ISSN 0915-6348

NATIONAL INSTITUTE FOR FUSION SCIENCE

Symposium on Development of Intensed Pulsed Particle Beams and Its Applications
February 20, 1990

(Received – Sep. 10, 1990)

NIFS-PROC-5 Oct., 1990

RESEARCH REPORT
NIFS-PROC Series

NAGOYA, JAPAN

Symposium on Development of Intense Pulsed Particle Beams and Its Applications

February 20, 1990

Edited by Kiyoshi Yatsui

(Received-Sept. 10, 1990)

NIFS-PROC-5 Oct., 1990

Symposium on Development of Intense Pulsed Particle Beams and Its Applications

February 20, 1990

Edited by Kiyoshi Yatsui

National Institute for Fusion Science, Nagoya, Japan

Keywords: Pulse-Power Technology, Inertial Confinement Fusion, Intense Charged Particle Beams, Ion-Beam Diodes, Beam-Target Interaction

PREFACE

On February 20 (Tuesday), 1990, "Symposium on Development of Intense Pulsed Particle Beams and Its Applications" was held at National Institute for Fusion Science, Nagoya, as a collaborative research program in the fiscal year of 1989. In spite that such the timing was not so good since everybody was so busy due to the end of the fiscal year, which actually ends in March, twelve papers were presented at this symposium, which were discussed in more detail among twenty five scientists attended from thirteen universities or institutes.

It was recognized and warmly welcome by everybody that, particularly nowadays, young scientists or students significantly begin to increase in Japan who are interested in pulse-power technology. At the same time, its applications grow up so wide that many industries are interested in practical use in commerce.

In summary, great achievements were obtained by this symposium in the fruitful discussions and in the settlement of its prospects in this particular field of interests.

Kiyoshi Yatsui
Symposium Chairman
Nagaoka University of Technology

PROGRAM OF SYMPOSIUM ON DEVELOPMENT OF INTENSE PULSED PARTICLE BEAMS AND ITS APPLICATIONS

February 20 (Tuesday), 1990

9:20 ~ 9:30	Preface/Address K. Yatsui (Nagaoka Univ. of Tech.)
9:30 ~ 10:00	Rayleigh-Taylor Instability in LIB ICF K. Kawata et al. (Nagaoka Univ. of Tech.)
10:00 ~ 10:30	Supertron H. Matsuzawa et al. (Yamanashi Univ.)
10:30 ~ 11:00	Two-Stage Ion Diode Experiments on Induction Adder S. Miyamoto et al. (Osaka Univ.)
11:00 ~ 11:30	Experiments toward the Development of New Pulsed Ion Diodes K. Horioka et al. (Tokyo Inst. of Tech.)
11:30 ~ 12:00	Study of Ablation of Target Material induced by Pulsed Ion Beam Bombardment S. Kamihata et al. (Kobe Univ. of Mercantile Marine)
12:00 ~ 13:15	Lunch
13:15 ~ 13:45	Theoretical Study of "Plasma Focus Diode" W. Jiang et al. (Nagaoka Univ. of Tech.)
13:45 ~ 14:15	Pulse-Power Characterisitcs of "VIVA-I", Versatile Inductive Voltage Adder K. Shimiya et al. (Nagaoka Univ. of Tech.)
14:15 ~ 14:45	Reduction of Low Energy Components in Pulse Ion Beam M. Sato et al. (Himeji Inst. of Tech.)

14:45 ~ 15:15 Observation and Focusing of Carbon Ion Beam by the "Inverse Pinch Ion Diode"

Y. Hashimoto et al. (Himeji Inst. of Tech.)

15:15 ~ 15:30 Coffee break

15:30 ~ 16:00 Generation of Pulsed Ion Beams by an Inductive Storage Pulsed Power Generator

S. Katsuki et al. (Kumamoto Univ.)

16:00 ~ 16:30 Power Plant by LIB Fusion

K. Niu et al. (Tokyo Inst. of Tech.)

16:30 ~ 17:00 Control of Gap Closure in Applied-B Diode

T. Aoki (Tokyo Inst. of Tech.)

17:00 ~ 17:05 Remarks/Acknowledgements

K. Yatsui (Nagaoka Univ. of Tech.)

CONTENTS

Page

RAYLEIGH-TAYLOR INSTABILITY IN LIB ICF

Shigeo KAWATA, Toshiaki SATO and Takayuki TERAMOTO
Department of Electrical Engineering,
Nagaoka University of Technology,
Nagaoka 940-21

Abstract

The Rayleigh-Taylor(R-T) Instability is studied in the Light-Ion-Beam(LIB) Inertial-Confinement-Fusion(ICF)-pellet. The R-T instability is one of the problems in ICF. The nonuniform acceleration field and the radiation effects on the LIB-ICF-pellet implosion are investigated by the linear analyses in this paper. By means of these analyses we obtained the following two results: 1) The nonuniform acceleration field in space does not change the growth rate(γ) of the R-T instability. However this nonuniformity may suppress the R-T instability in some particular cases. 2) The radiation may reduce the growth rate(γ).

§ 1. Introduction

This paper presents how the growth rate(γ) of the Rayleigh-Taylor(R-T) instability is affected by the nonuniform acceleration field in space and the radiation effects in the Light-Ion-Beam(LIB) Inertial-Confinement-Fusion(ICF)-pellet implosion.

The acceleration and the density gradient in the fuel pellet cause the R-T instability[1-11] during the implosion process in ICF. The R-T instability may prevent the fuel compression to the high density which is essential to burn the fuel and extract the fusion energy efficiently. Therefore it is important to investigate the growth of the R-T instability in the implosion process.

In this paper the nonuniform acceleration field and the radiation effects on the R-T instability in the LIB-ICF-pellet implosion are investigated by the linear analyses. Generally the nonuniform heating of the fuel surface is observed because of the limited number of the incoming beams. This nonuniformity causes the nonuniform implosion. In addition the radiation becomes a primary energy carrier especially in a reactor-size pellet and may have the influence on the R-T instability. By means of our analyses we obtained the following two results: 1) The nonuniform acceleration field does not change

the growth rate(γ)of the R-T instability. However this nonuniformity may suppress the R-T instability in some particular cases. 2) The radiation may reduce the growth rate(γ) of the R-T instability at the ablating surface. In this case the spatial profiles of the physical quantities in the zeroth order are obtained by the computations using the one-dimensional implosion code[12,13]. The perturbation equations are solved self-consistently based on these profiles.

§ 2. Influence of Nonuniform Acceleration Field in Space

In order to investigate the influence of the nonuniform acceleration field in space on the R-T instability, we perform the linear analyses with the assumptions that the fluid plasma is incompressible and inviscid. We also assume that the density and the pressure of the zeroth-order are the function of the space coordinate z only. As the basic equations we employ the following three equations:

$$\frac{\partial \rho}{\partial t} + \vec{\nabla} \cdot (\rho \vec{v}) = 0 \tag{1}$$

$$\rho \left(\frac{\partial \vec{v}}{\partial t} + (\vec{v} \cdot \vec{\nabla}) v \right) = -\vec{\nabla} p + \rho g \hat{z} \tag{2}$$

$$\vec{\nabla} \cdot \vec{v} = 0 \tag{3}$$

Here $\hat{z}$ shows the unit vector directing along the z axis. Let us introduce the nonuniform acceleration field:

$$\begin{aligned} g(x,y,z,t) &= g_0 + \delta g(x,y,z,t) \\ &= g_0 + g_1 f(x,y) \exp(-\beta |z|) T(t) \end{aligned} \tag{4}$$

In eq.(4) β is a positive constant, g_0 is the constant acceleration of the zeroth order and the nonuniformity of the acceleration (δg) is the first-order one, having the spatial $(x-y)$-dependency of $f(x,y)$ and the time dependency of $T(t)$. The equilibrium condition is

$$\frac{\partial p_0}{\partial z} = -\rho_0 g_0. \tag{5}$$

The physical quantities of the zeroth order are denoted with the suffix 0. The first-order quantities are distinguished by attaching the symbol (δ) to the expressions for the physical quantities. In our analyses the perturbation velocity is denoted by (u, v, w), and the density and the pressure have the forms of $\rho = \rho_0 + \delta\rho$ and $p = p_0 + \delta p$, respectively.

Assuming $g_0 \gg g_1$, eliminating the equilibrium term and taking the Fourier transformation in space and the Laplace transformation in time, we obtain the following differential equation:

$$\begin{aligned} D(\rho_0 D\tilde{w}) &= (-k^2)\Big\{-\rho_0\tilde{w} + \frac{g_0(D\rho_0)\tilde{w}}{\gamma^2} \\ &\quad - \frac{\rho_0 g_1 \tilde{f}(k_x,k_y)\exp(-\beta|z|)\tilde{T}(\gamma)}{\gamma}\Big\}, \end{aligned} \tag{6}$$

where $D = d/dz$, $k = \sqrt{k_x^2 + k_y^2}$ and the physical quantities with a tilde denote those after the transformations.

In this section we consider the two superposed fluids with the constant density ρ_2 for $z > 0$ and ρ_1 for $z < 0$. Then eq.(6) is simplified as follows:

$$(D^2 - k^2)\tilde{w} = k^2 g_1 \tilde{f}\tilde{T}\exp(-\beta|z|)/\gamma \tag{7}$$

The solution for $\tilde{w}$ derived from eq.(7) is

$$\tilde{w} = A(k_x,k_y,\gamma)\exp(+kz) + \frac{k^2 g_1}{\gamma}\tilde{f}\tilde{T}\frac{\exp(+\beta z)}{\beta^2 - k^2} \qquad (z < 0), \tag{8}$$

$$\tilde{w} = A(k_x,k_y,\gamma)\exp(-kz) + \frac{k^2 g_1}{\gamma}\tilde{f}\tilde{T}\frac{\exp(-\beta z)}{\beta^2 - k^2} \qquad (z > 0). \tag{9}$$

In eqs.(8) and (9) the arbitrary function A should have the form of

$$A(k_x,k_y,\gamma) = 2\pi\Phi\delta(k_x - k_{x0})\delta(k_y - k_{y0})/(\gamma - \gamma_0), \tag{10}$$

in order to satisfy the condition that the perturbed velocity is in agreement with one for the standard R-T instability with the wave number (k_{x0}, k_{y0}) and the growth rate γ_0, when $\delta g = 0$. The amplitude of the perturbed velocity at $t = 0$ is described by Φ.

The boundary condition is obtained by integrating eq.(6) over the infinitesimal element of z including $z = 0$.

$$\Delta_0(\rho_0 D\tilde{w}) = -\frac{k^2 g_0}{\gamma^2}\Delta_0(\rho_0)\tilde{w}(z=0) \tag{11}$$

Here $\Delta_0(F) = F(+0) - F(-0)$ for the physical quantity F. Inserting eqs.(8)and (9) into eq.(11), we find the equation for the growth rate γ:

$$A\gamma^3 + \frac{kg_1\tilde{f}\tilde{T}\beta\gamma^2}{\beta^2 - k^2} - A\alpha g_0 k\gamma - \frac{\alpha g_0 k^3 g_1 \tilde{f}\tilde{T}}{\beta^2 - k^2} = 0 \tag{12}$$

Here α is the Atwood number.

Then we obtain the growth rate under the nonuniform acceleration field by solving eq.(12). Here we choose the nonuniform acceleration field as

$$\delta g = g_1 \exp(ik_{xg}x + ik_{yg}y)\exp(-\beta|z|) \tag{13}$$

for $t > 0$ and $\delta g = 0$ for $t < 0$. This means that the nonuniform acceleration field distributes with the wave number k_{xg} in the x direction and k_{yg} in the y direction. The perturbation of the boundary surface of the two superposed fluids and the nonuniform acceleration field are shown schematically in Fig.1. In this case the growth rate obtained from eq.(11) is equal to $\gamma = \sqrt{\alpha g_0 k}$, which agrees with that of the standard R-T instability[5]. Especially when the wave number (k) of the perturbation is equal to that ($k_g = \sqrt{k_{xg}^2 + k_{yg}^2}$) of the nonuniform acceleration field, we obtain the velocity of the perturbation in the real space (x, y, z, t).

$$\begin{aligned} w &= \Phi \exp(ik_{xg}x + ik_{yg}y)\exp(-k|z|)\exp(\gamma t) \\ &\quad -g_1 \exp(ik_{xg}x + ik_{yg}y)\exp(-\beta|z|)t \\ &\equiv w_0 + w_1 \end{aligned} \tag{14}$$

The first term (w_0) of eq.(14) corresponds to the R-T instability and the second (w_1) describes the free falling induced by the imposed nonuniform acceleration field. From eq.(14) it is found that the mechanism of the suppression for the R-T instability exists under the following particular cases: If the phase of the R-T instability coincides with that of the free falling, the R-T instability may be suppressed by δg, though the R-T instability may enhanced, if the phases do not coincide with each other.

Here we estimate the suppression effect of the nonuniform acceleration field on the R-T instability. We define R at $z = 0$.

$$R = \frac{w_1}{w_0} \times 100 = \frac{g_1 t}{\Phi \exp(\gamma t)} \times 100 \tag{15}$$

Table 1 shows the ratio R for the following case: The growth rate $\gamma = \sqrt{\alpha g_0 k}(\alpha = 1)$, $g_0 = 1.0 \times 10^{13}(\mathrm{m/sec^2})$, $g_1 = 0.1 \times g_0, \Phi = a \times 6.185 \times 10^5$ (m/sec) and $t = 1.0$(nsec). It is found that the ratio R is several or several tens per cent in this case. These values of R depend on those of the parameters employed. One may choose the appropriate values for these parameters in order to overcome the growth of the R-T instability by the imposed nonuniformity (δg).

In an actual system the short wavelength (large k) region is stabilized by the effects of the density gradient, the convection and the heat conduction. Thus the suppression effect shown in this section may be effective for the long wavelength region. This fact suggests that we may control the R-T instability as follows: For example we may introduce

the artificial nonuniform acceleration field by the input beams in the initial stage of the implosion. After the perturbation by the R-T instability grows because of this nonuniformity, we may change the phase of the nonuniformity of the input beams by π. Then we may suppress the growth of the R-T instability by the effect discussed above.

§ 3. Influence of Radiation

In a fuel pellet of a reactor size the radiation transportation and the radiation pressure have the important roles. In this section we discuss about the influence of the radiation on the growth of the R-T instability at the ablation front of the pellet impinged by the LIB. The space profile of the physical quantities during the implosion phase are obtained by the computation using the one dimensional implosion code[12,13]. In the analyses the linear equations are solved as an eigenvalue problem and the self-consistent growth rate is obtained.

The basic equations including the radiation terms are:

$$\frac{\partial \rho}{\partial t} + \vec{\nabla} \cdot (\rho \vec{v}) = 0 \tag{16}$$

$$\rho \left(\frac{\partial \vec{v}}{\partial t} + (\vec{v} \cdot \vec{\nabla}) \vec{v} \right) = -\vec{\nabla}(p + p_R) + \rho \vec{g} \tag{17}$$

$$\rho C_V \left(\frac{\partial T}{\partial t} + (\vec{v} \cdot \vec{\nabla}) T \right) = -(p + p_R) \vec{\nabla} \cdot \vec{v} + \vec{\nabla}(\kappa_e \vec{\nabla} T + \kappa_R \vec{\nabla} T), \tag{18}$$

where C_V is the specific heat, p_R is the radiation pressure and $\kappa_R = 16\sigma l_R T^3/3$ is the coefficient of the radiation heat conduction. Here σ is the Stefan-Boltzmann constant and l_R is the Rosseland mean free path[14].

Let us consider eqs.(16)-(18) on the coordinate moving with the ablation surface. In order for the simplicity we assume that the plasma is an ideal gas with the constant charge z. The equation of state is $p = \rho kT/\mu$ where k is the Boltzmann constant, $\mu = m_i/(1+z)$, m_i the ion mass and the specific heat $C_V = 3/(2\mu)$. We normalize the basic equations with the physical quantities at the radius r_S (the density ρ_S, the temperature T_S, the acoustic sound velocity v_S, the pressure p_S and the radiation pressure p_{RS}). Then we obtain the following equations:

$$\frac{\partial \tilde{\rho}}{\partial \tilde{t}} + \frac{1}{\tilde{r}^2} \frac{\partial}{\partial \tilde{r}} (\tilde{r}^2 \tilde{\rho} \tilde{v}_r) + \tilde{\vec{\nabla}}_\perp \cdot (\tilde{\rho} \tilde{\vec{v}}_\perp) = 0 \tag{19}$$

$$\rho \left\{ \frac{\partial \tilde{\vec{v}}}{\partial \tilde{t}} + ((\tilde{\vec{v}} \cdot \tilde{\vec{\nabla}}) \vec{v})_r \right\} = -\frac{\partial}{\partial \tilde{r}} (\tilde{p} + \frac{p_{RS}}{p_S} \tilde{p}_R) + \tilde{\rho} \tilde{\vec{g}} \tag{20}$$

$$\rho\left\{\frac{\partial\tilde{\vec{v}}}{\partial\tilde{t}}+\left((\tilde{\vec{v}}\cdot\tilde{\vec{\nabla}})\vec{v}\right)_{\perp}\right\}=-\tilde{\vec{\nabla}}_{\perp}(\tilde{p}+\frac{p_{RS}}{p_S}\tilde{p}_R) \tag{21}$$

$$\begin{aligned}\frac{3}{2}\tilde{\rho}(\frac{\partial\tilde{T}}{\partial\tilde{t}}+(\tilde{\vec{v}}\cdot\tilde{\vec{\nabla}})\tilde{T}) &= -(\tilde{p}+\frac{p_{RS}}{p_S}\tilde{p}_R)\left\{\frac{1}{\tilde{r}^2}\frac{\partial}{\partial\tilde{r}}(\tilde{r}^2\tilde{v}_r)+\tilde{\vec{\nabla}}_{\perp}\cdot\tilde{\vec{v}}_{\perp}\right\}\\ &+\frac{K_0}{\tilde{r}^2}\frac{\partial}{\partial\tilde{r}}(\tilde{r}^2\tilde{T}^{5/2}\frac{\partial\tilde{T}}{\partial\tilde{r}})+\frac{K_{R0}}{\tilde{r}^2}\frac{\partial}{\partial\tilde{r}}(\tilde{r}^2\frac{\tilde{T}^{13/2}}{\tilde{\rho}^2}\frac{\partial\tilde{T}}{\partial\tilde{r}})\\ &+K_0\tilde{\vec{\nabla}}_{\perp}\cdot(\tilde{T}^{5/2}\tilde{\vec{\nabla}}_{\perp}\tilde{T})+K_{R0}\tilde{\nabla}_{\perp}\cdot(\frac{\tilde{T}^{13/2}}{\tilde{\rho}^2}\tilde{\vec{\nabla}}_{\perp}\tilde{T})\end{aligned} \tag{22}$$

Here we denotes the radial components with the suffix r and the azimuthal components with the suffix $\perp$. In these equations $\tilde{t}=(v_S/r_S)t$, $\tilde{\vec{\nabla}}=r_S\vec{\nabla}$, $\tilde{\vec{\nabla}}_{\perp}$ is the azimuthal component of $\tilde{\vec{\nabla}}$, $\tilde{\vec{g}}=r_S\vec{g}/v_S^2$, $K_0=K_{SP}T_S^{5/2}\mu/(\rho_S v_S r_S)$ where K_{SP} is the coefficient for the electron thermal conduction given by Spitzer and $K_{R0}=K_R T_S^{13/2}\mu/(\rho_S^3 v_S r_S)$ where $K_R=16\sigma l_R/(3c)$.

Now we consider the perturbation equation. We assume that the first-order physical quantities have the following form:

$$\delta f=\sum_{lm} f_1(\tilde{r})\exp(\tilde{\gamma}\tilde{t})Y_{lm}(\theta,\phi) \tag{23}$$

Here Y_{lm} is the spherical harmonics. Assuming the spherically symmetry of the zeroth-order quantities, we obtain the perturbation equations, which are written formally as follows:

$$a_{ij}(\partial/\partial\tilde{r},l,\tilde{\gamma})\Psi^T(\tilde{r})=0. \tag{24}$$

Here a_{ij} is the (5×5) matrix and $\Psi=(\rho_1,v_1,D_1,T_1,Q_1)$, where $D_1=\tilde{\vec{\nabla}}_{\perp}\cdot\tilde{\vec{v}}_{\perp}$ and Q_1 is the perturbation of the heat flow. Solving eq.(24) as an eigenvalue problem, we obtain the self-consistent growth rate of the R-T instability.

In order to accomplish this purpose we have to calculate the actual implosion process to obtain the profile of the zeroth-order physical quantities. We use the one dimensional implosion code for this purpose and employ the one-temperature model. The target structure employed is shown in Fig.2, which is a simple direct-driven pellet consisting of three layers of Pb, Al and DT. The pellet radius is 5(mm) and the thickness of each layer is 26.7(μm) for Pb, 161.3(μm) for Al, and 55.8(μm) for DT. The total mass of the DT fuel is 3(mg). During the implosion process, we assume that the charge z is a constant and, 13.3, 7.8 and 1 for Pb, Al and DT, respectively. The proton beam whose particle energy is 5(MeV) is employed, and the total LIB energy is 5(MJ). The pulse shape is as follows: The pulse rising time is 15(nsec) and the beam power increases with the function of (time)^2 and is a constant(167(TW)) from 15(nsec) to 40(nsec). After 40(nsec) the beam power is equal to zero .

Figure 3 shows the density profile at the time $t = 40$(nsec). The magnification of the density profile at the ablation surface is shown in Fig.4. The solid line shows the result for the case with the radiation and the dashed line shows for the case with no radiation. It is found that the density gradient with the radiation is gentle compared with that without the radiation. In addition the acceleration of the implosion with the radiation is 5.0×10^{14}(cm/sec^2), which is small compared with that with no radiation 1.2×10^{15} (cm/sec^2). This comes from that a part of the input energy escapes from the outer surface of the pellet by the radiation energy transport. From these two facts we can expect that the growth rate of the R-T instability may be reduced by the radiation transport.

We obtained the growth rate of the R-T instability of these density profiles. Figure 5 shows the results of the calculation discussed above by a solid line for the case with the radiation and a dashed line for the case without radiation, and also the estimation by a dot-dot-dashed line for the case with the radiation and a dot-dashed line without radiation of the growth rate. It is found that the radiation effects reduce the growth rate as is expected above. This fact mainly comes from the fact that the radiation energy transport causes the decrease of the acceleration. On the other hand the decrease of the growth rate in the short wavelength region (large k) results from the effects of the density gradient, the convection and the heat conduction. In Fig.5 the estimation curves include these effects by the following expressions[7,10,11]:

$$\gamma = \sqrt{\frac{gk}{1+kL} + \frac{1}{4}k^2v^2} - \frac{1}{2}kv \tag{25}$$

In eq.(25) k is estimated as l/r_a, where l is the spherical mode in eq.(23) and r_a is the radius of the ablation front. The parameter L is the typical length of the density gradient (30.45(μm) for the case with the radiation and 29.8(μm) for the case without radiation) and v is the speed of the convection (4.205×10^5(cm/sec) for the case with the radiation and 4.118×10^5(cm/sec) without radiation). The eigen-value analysis agrees with the estimation in the general tendency. We may say that the radiation effects reduce the growth rate (γ).

§ 4. Conclusion

In this paper we investigated the influence of the nonuniform acceleration field in space and the radiation on the R-T instability. We found that the growth rate of the R-T instability was unchanged by the nonuniformity in space of the acceleration field.

However the growth might be suppressed by the nonuniform acceleration field in some particular cases. We also found that the zeroth-order density gradient became less steep in the case which had the radiation and the growth rate of the R-T instability was reduced by the escape of the radiation energy from the outer surface of a pellet and confirmed the effects of the density gradient, the convection and the heat conduction on γ. This reduction of the growth rate for the R-T instability comes mainly from the reduction of the acceleration because of the escape of the input LIB energy from the pellet outer surface.

Acknowledgments

Our computations were performed partly on the computer in the National Institute of Fusion Science, Japan.

References

1) S.Chandrasekhar : *Hydrodynamic and Hydromagnetic Stability* Chapt.X, Dover(1981)
2) L.Baker : Phys.Fluids **26**, 391(1983)
3) H.J.Kull : Phys.Rev.A **31**, 540(1985)
4) H.J.Kull and S.I.Anisimov : Phys.Fluids **29**, 2067(1986)
5) T.Abe and K.Niu : Jpn.J.Appl.Phys. **20**, 91(1981)
6) F.Troyon and R.Gruber : Phys.Fluids **14**, 2069(1971)
7) H.Takabe and K.Mima : J.Phys.Soc.Jpn **48**, 1793(1980)
8) H.Takabe, L.Montierth and R.L.Morse : Phys.Fluids **26**, 2299(1983)
9) H.Takabe, K.Mima, L.Montierth and R.L.Morse : Phys.Fluids **28**, 3676(1985)
10) S.E.Bodner : Phys.Rev.Lett. **33**, 761(1974)
11) D.H.Munro : Phys.Rev. A **38**, 1433(1988)
12) J.P.Christiansen, D.E.T.F.Ashby and K.V.Roberts : Comp.Phys.Comm. **7**, 271(1974)
13) M.Tamba, N.Nagata, S.Kawata and K.Niu : Laser and Particle Beams **1**, 121(1983)
14) Y.B.Zel'dovich and Y.P.Raizer : *Physics of Shock Waves and High-Temperature Hydrodynamic Phenomena* Chapt.V, Academic Press(1966)

Table.1

k	a=0.005	a=0.01
5	25.9	12.9
10	23.6	11.8
50	16.0	8.0
100	11.9	6.0
500	3.5	1.7
1000	1.4	0.7

The effect of the nonuniform acceleration field on the perturbation velocity in the case of the growth rate $\gamma = \sqrt{\alpha g_0 k}$, $\beta = 0$, $g_0 = 1.0 \times 10^{13}(\mathrm{m/sec^2})$, $g_1 = 0.1 g_0, \Phi = a \times 6.185 \times 10^5$ (m/sec) and $t = 1.0$(nsec). The free falling may suppress the R-T instability.

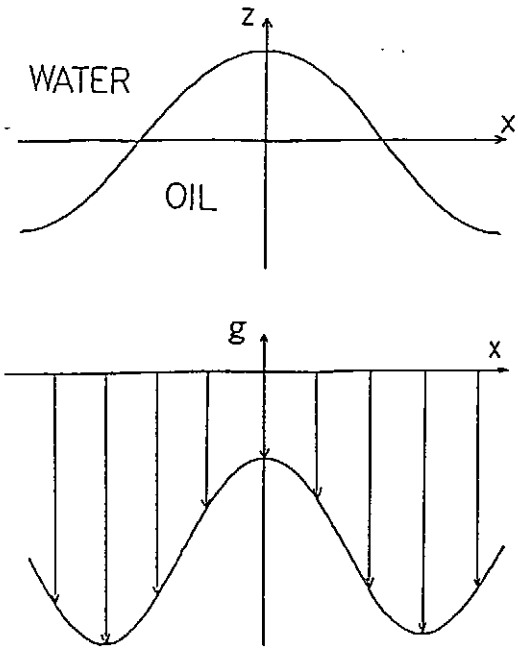

Fig.1 Schematic diagram for the perturbation of two superposed fluids and the nonuniform acceleration field $g = g_0 + g_1 \exp(ik_{xg}x + ik_{yg}y)$.

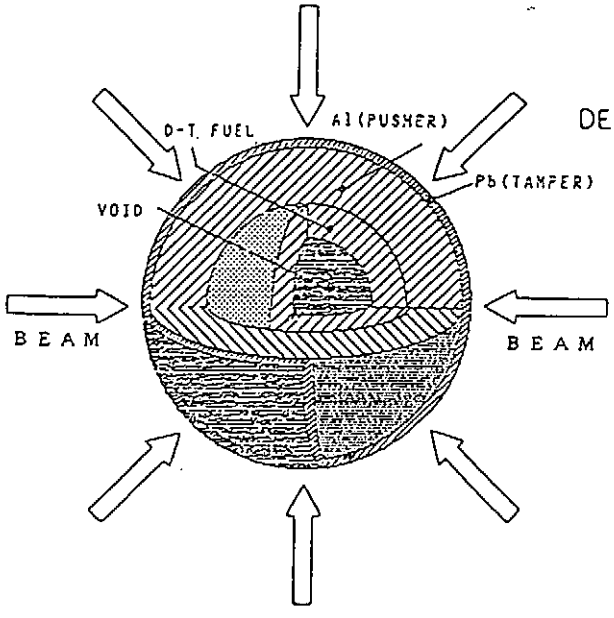

Fig.2 The fuel pellet structure employed in the simulation in this paper. The LIB impinges the fuel pellet and deposits its energy mainly in Al and partly in Pb. The Pb behaves as a tamper and the Al as a beam energy absorber. The inner part of Al behaves as a pusher.

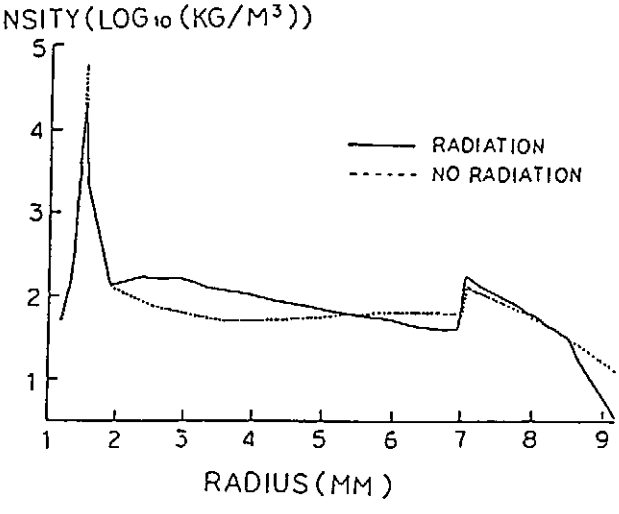

Fig.3 The density profiles at the time $t = 40$(nsec).

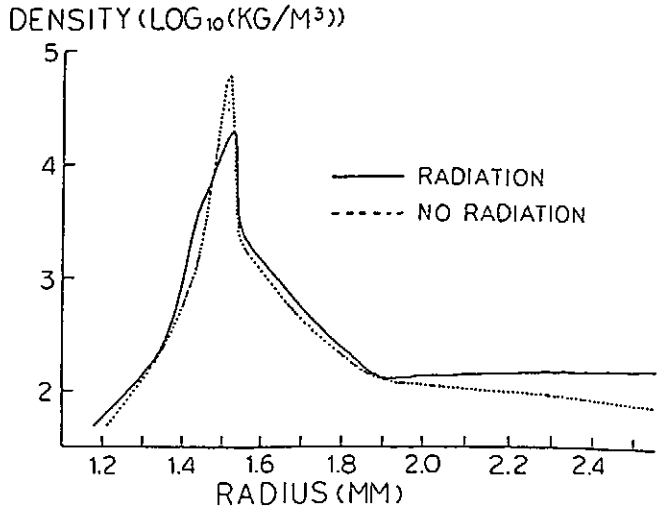

Fig.4 The magnification of the density profile at the ablation front in Fig.3. The solid line shows the result with the radiation and the dashed line with no radiation. The density gradient in the case with the radiation is gentle compared with that with no radiation.

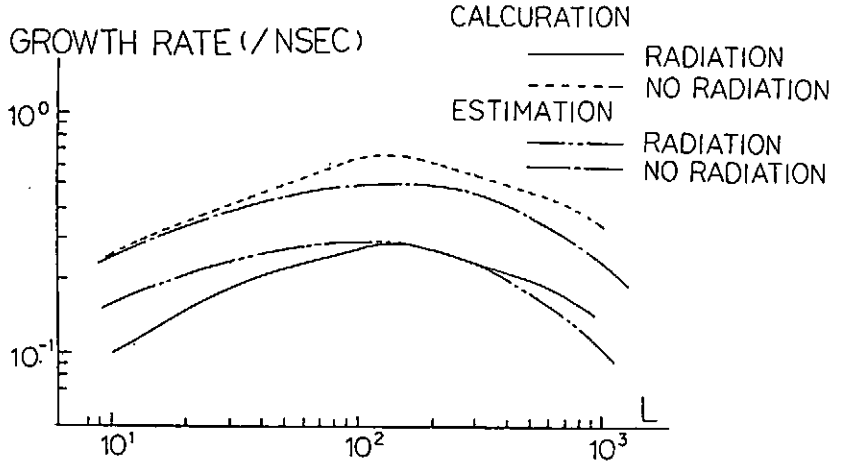

Fig.5 The estimation and the numerical calculation of the growth rate of the R-T instability at the ablation front in Fig.4. The numerical results are shown by a solid line and a dashed line, and the estimation by the dot-dashed line and the dot-dot-dashed line. The estimations include the effects of the density gradient, the convection and the heat conduction. The growth rate with the radiation is small compared with that with no radiation because of the radiation energy transport.

TWO-STAGE ION DIODE EXPERIMENTS ON INDUCTION ADDER

S.Miyamoto, Y.Yasuda, M.Yamamoto, T.Honma, A.Zakou, S.Umehara
T.Akiba, K.Imasaki*, C.Yamanaka* and S.Nakai

Institute of Laser Engineering,Osaka University
2-6, Yamada-oka, Suita,Osaka 565, Japan
* Institute for Laser Technology, Osaka 565, Japan

Abstract

Two-stage ion diode experiment has been performed on an induction adder accelerator "Reiden-SHVS". The second stage diode is operated in an ion beam injection mode. Enhanced space-charge-limited current in second stage diode indicates a formation of virtual anode due to the energetic ion beam injection. The beam deflection by virtual anode formation occurred only at inner part of the beam. Two-stage charge-stripping ion diode is demonstrated. Carbon beam of C^+ and C^{2+} are stripped and partially recombined in thin stripping foil and accelerated at second diode.

I. Introduction

In recent years, ion diode have been the key subject of considerable experimental and theoretical research for use as an inertial confinement fusion driver. Ion diodes covert the pulsed power energy into a uniform ion beam suitable for pellet implosion. In order to accomplish this efficiently, the flow of electrons across the diode gap must be inhibited. This is accomplished with the application of a strong magnetic field parallel to the diode electrode.[1] In most experiments, ion diode have used surface flashover anodes to produce the anode plasma from which the beam ions are extracted. This type of diode typically demonstrate a rapidly changing impedance. The impedance generally starts out very high during the electrode plasma formation phase. After that, the ion current rapidly increases and diode impedance decreases rapidly. This impedance behavior is unsuitable to generate a ramped-voltage beam for ballistic bunching/axial compression system and also is less efficient in coupling between the pulsed power generator and the ion diode. Furthermore, a empirical scaling of ion diode impedance[2] implies the existence of a limiting voltage V* at which the ion current diverges. A recent theory[3] of ion diodes that includes the self-consistent virtual cathode motion has explained the observed ion diode impedance characteristics.

To avoid this impedance collapse and limiting voltage of diode, ion source limiting operation of diode is considered. One method is to use an externally injected ion source plasma.[4] Ion current density is limited by the ion flux nivi where ni and vi are density and drift velocity of the ion source plasma, respectively. Plasma injection ion source improves turn-on delay of ion beam generation and lower the early time impedance.[5] Another method to control the diode impedance is to use an ion beam injected diode. Ion beams generated in a separate ion diode (first stage) injected into the

main acceleration diode (second stage). The potential distribution of ion beam injected diode must be different from the case with a stationary anode plasma ion source. With increasing the injection ion current over a simple Chiled-Langmuir value of second diode, the virtual anode is formed near the anode. The space charge limiting current increases due to the energetic ion beam injection. For strong insulation field, a maximum steady state current of ion beam injection diode[6]

$$J_i^* = J_{CL}^i \left(\frac{W}{V}\right)^{\frac{9}{2}} \left(\sqrt{1+\frac{V}{W}} - 1\right)^3 \left(\left(4+\frac{V}{W}\right)\sqrt{1+\frac{V}{W}} + 3\frac{V}{W} + 4\right)^2 \quad (1)$$

where $J_{CL}^i = (4/9)\varepsilon_0(2eZ/M)^{(1/2)}V^{(3/2)}/d_S$ is simple Child-Langmuir current, W and V are the voltage of first and second stage diode, M and eZ are the ion mass and charge, and ds is AK gap of second diode.

This operation regime is important to generate a high current density beam by the two-stage charge stripping diode. In this paper, we show 1) an experimental performance of plasma injection diode, 2) a virtual anode formation and its effect on ion beam trajectory in ion beam injection diode, and 3) a demonstration of two-stage charge stripping ion diode.

II. Experimental Apparatus

Experiments were performed on Reiden-SHVS induction adder accelerator. Reiden-SHVS consists of a 500 kV, 100 ns, 1.25 ohm pulsed power generator, a power divider, 32-high voltage cables and eight-stage induction adder cavities. It has a capability to generate 4 MV, 40 kA, 100 ns pulse into single diode. Figure 1 shows schematic configuration of the induction adder. Center electrode extended from right

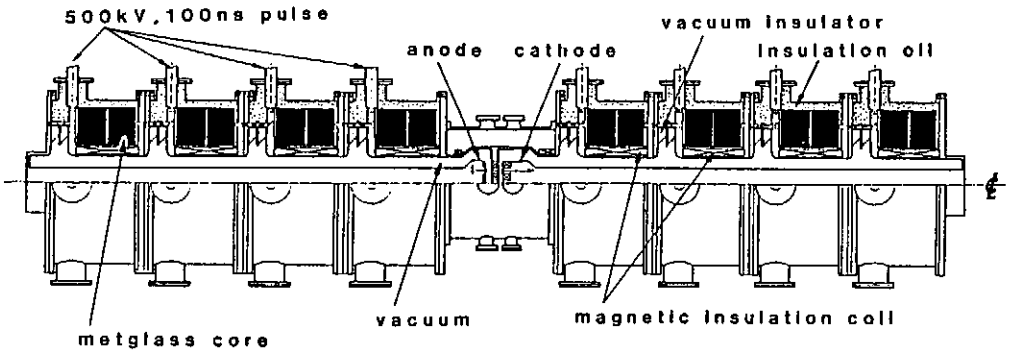

Fig.1 Schematic configuration of eight stages induction adder "Reiden-SHVS".

(left) hand side of induction cavities is positive (negative). Figure 2 shows two-stage magnetically insulated ion diodes which are set between two center electrodes of induction adder. The ground electrode is combined a cathode of first diode and an anode of second diode. Each diode are powered by four induction cavities. All experiments were performed with a voltage of 100 to 200 kV/stage, then 400 to 800 kV/diode.

The anode electrode of first stage diode is made from aluminum to exclude the insulation magnetic field generated by cathode coil. Charge stripping foils which are made by Formver film of less than 0.1 micro-meter thickness are optionally used. In order to maintain the ion canonical momentum to be zero, these foils are set on the anode surface of second diode where is approximately on a separatrix line between two coils (first and second stage diode coils).

Ion sources used in the experiments are a pallafin grooves anode and an injection plasma from carbon flashboard located behind the anode which have three circular slot of 6 mm width. The flashboard is driven by a 25 kV, 1.2 micro-farad capacitor bank. The active anode area are 99 cm^2. The first stage diode gap of d_f = 9.2 mm and the second stage diode gap d_s was varied from 8.3 mm to 33.3 mm.

The ion current density is measured by biased charge collectors which are located inside the center electrode of negative adder 12 cm behind the cathode. The energy spectrum and species of the ion beam are measured by a Thomson parabola analyzer. The ion beam trajectories are measured by the combinations of shadow-box and scatter-ion pinhole camera located four different Z-axial positions and three different radial positions.

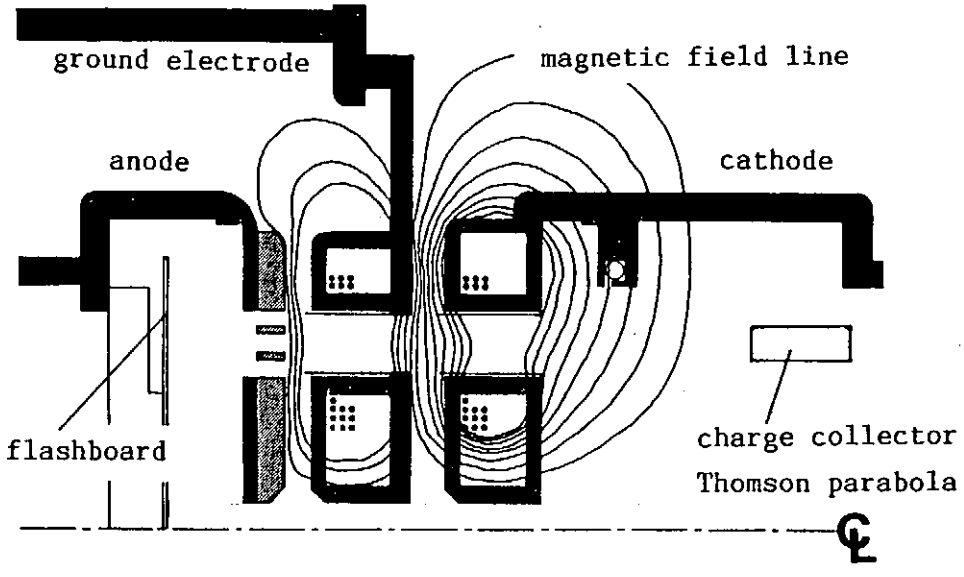

Fig.2 Two-stage magnetically insulated ion diode.

III. Experimental Results

Electrical characteristics of injection plasma and diode

Figure 3 shows a driving voltage waveforms and a plasma signals from the carbon flashboard without (a) and with (b) a transverse insulation field (9 kG). The plasma signals shows two peaks. The plasma drift velocities of the first and the second peak are 1.8 x 10^7 cm/s and 1.0 x 107 cm/s, respectively. The peak ion flux at the anode is estimated to be 400 A/cm^2 and is correspond to the ion density of 2.5 x 10^{14} /cm^3. Considerable amount of plasma is measured through the strong transverse magnetic field as shown in Fig.3(b). By changing the timing between the plasma injection and the diode pulse, the diode operation can be chosen from no ion source diode to the plasma prefill diode.

Electrical characteristics of first-stage diode are shown in Fig.4. Early time impedance is high in the both case of pallafin groove ion source and no ion source. The paraffin groove anode turns on about 30 nano-second after the voltage application and then the impedance starts to decrease. An adequately injected plasma can reduce the early time impedance to near the generator matched value (50 ohm).

Typical voltage waveforms and impedance characteristics of two-stage diode are shown in Fig.5. The impedance of second diode which is operated as an ion beam injected diode rapidly turn on and graduate increase during the later part of pulse. High time impedance of second diode at early time is due to a finite ion time of flight between the first diode and the second diode.

Ion current limitation

If the second diode gap increases with fixed ion beam injection, the ion current density in the second diode change from source limited value to the enhanced space charge limited value J_i^*. Figure 6 shows the ion current density measured at the back of second diode. The data of single diode operation (second stage is shorted) are represented in Fig.6 as the data point of second diode gap is zero ($d_S = 0$). The solid line in Fig.6 is calculated steady state limiting current J_i^* (Eq.(1))for C^+ ions assuming the first and second diode voltage were 0.45 MV.

Approximately four tomes higher ion current over the steady state limiting current J_i^* are observed for the diode with AK gap larger than 2.33 cm. In this condition, monoplar theory predict that the ion flow should be unstable. Because of the maximum transmittable current in the second diode is not at the maximum virtual anode potential.

In the case of high current injection ($d_S > 1$ cm in Fig.6(b)), the humped potential distribution in the second diode (due to the virtual anode formation) are modified by the large ion current injection. The virtual anode width increases with increasing the injection current andthen the effective diode gap decreases. Furthermore, the electrons are drawn

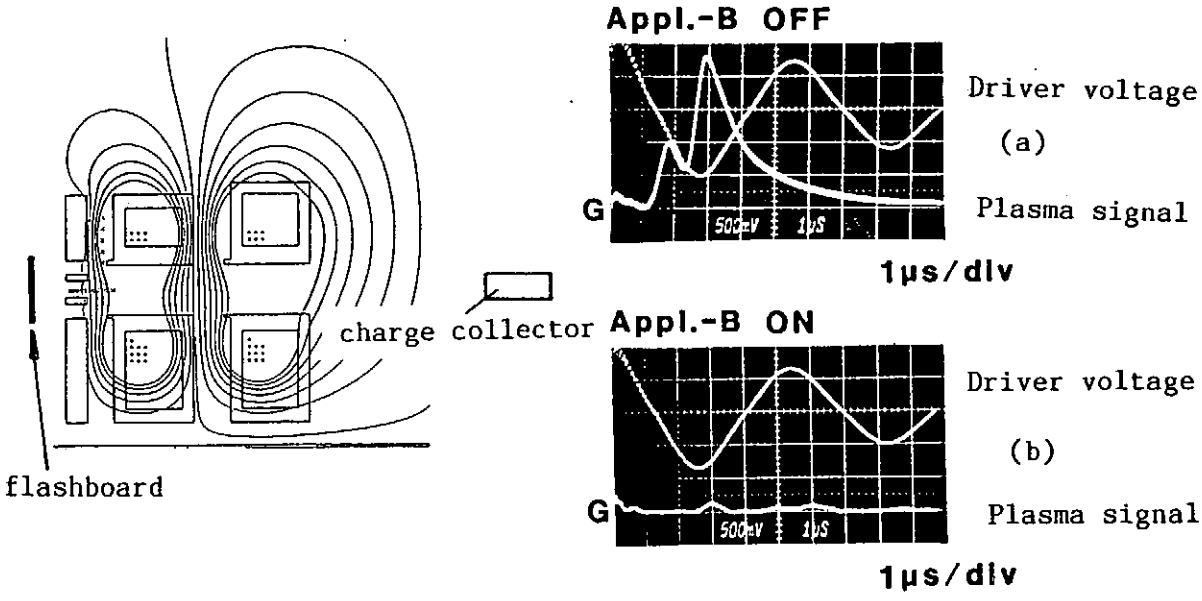

Fig.3 Voltage waveform and plasma signals from the carbon flashboard without (a) and with (b) a transverse magnetic field.

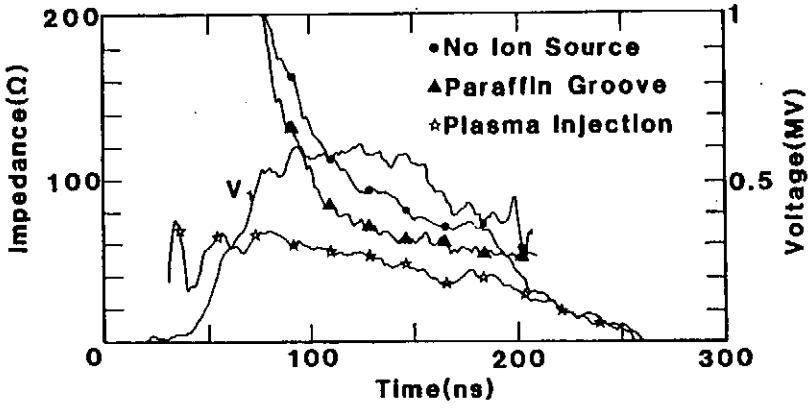

Fig.4 Electrical characteristics of first stage diode.

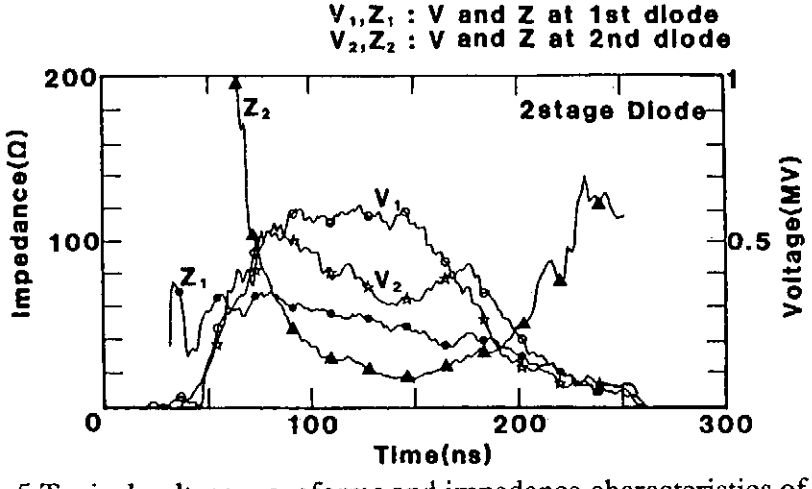

Fig.5 Typical voltage waveforms and impedance characteristics of two-stage diode.

in the diode from both the anode and cathode side due to the enhanced ion space charge. This electrons reduces the ion space charge and more ions can enter the diode. Schematic configurations of potential distribution in the diode at different injection beam current are shown in Fig.7. In LIB-ICF application, the second diode should be operated with small virtual anode potential.

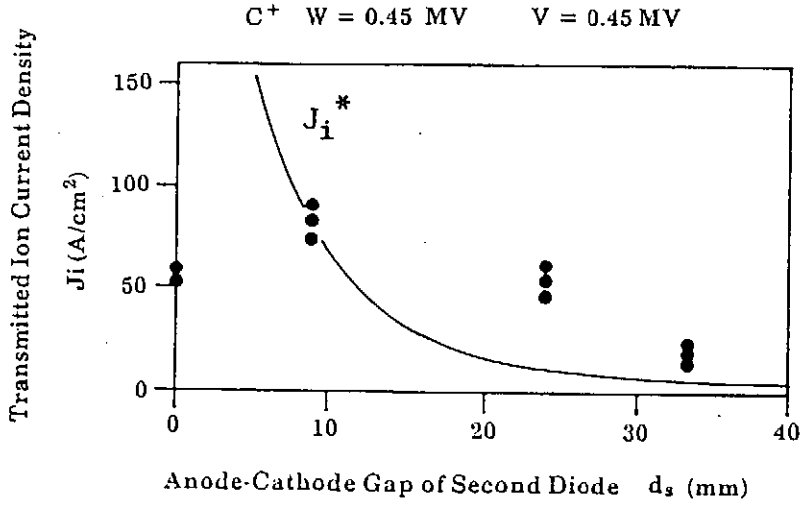

Fig.6 The ion current density measured at 12 cm from the cathode as a function of AK gap of second diode. (a) low injection current, and (b) high injection current case.

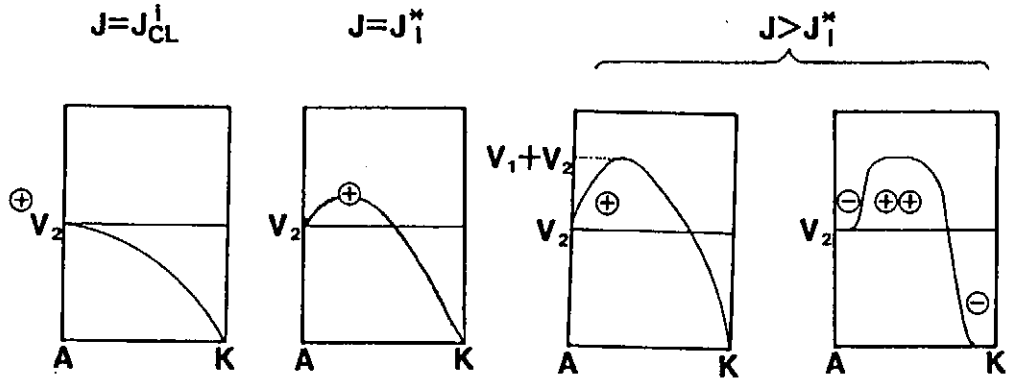

Fig.7 Schematic configurations of potential distribution in the ion beam injected diode with different injection beam current.

Beam trajectory

Beam trajectories are measured at four different axial (z-direction) position, z = 16.2 mm, 26.2 mm, 115.5 mm and 125.5 mm. Origin of z-axis is the anode surface of first diode and the anode surface of second diode is z = 47.2 mm. Figure 8 shows the measured beam trajectory in the two stage diode. Comparison of beam trajectories were made between deferent diode operations; an ion source limiting operation of second diode (ds = 8.3 mm) and a space charge limiting operation with virtual anode formation (ds = 33.3 mm)(Fig.8). No trajectory differences are observed for outer (r = 75.5 mm) and center (r = 68.5 mm) part of beam. But inner part of beam (r = 61.5 mm) changes the radial direction by 60 mrad. This angle includes an edge effect of virtual anode and also the bending by the deformation of electron virtual cathode because of changing the magnetic field line shape which is crossed by cathode chip. To avoid the large beam deflection of inner part of beam, the diode should be operated in ion source limited regime in which the virtual anode dose not so much grow.

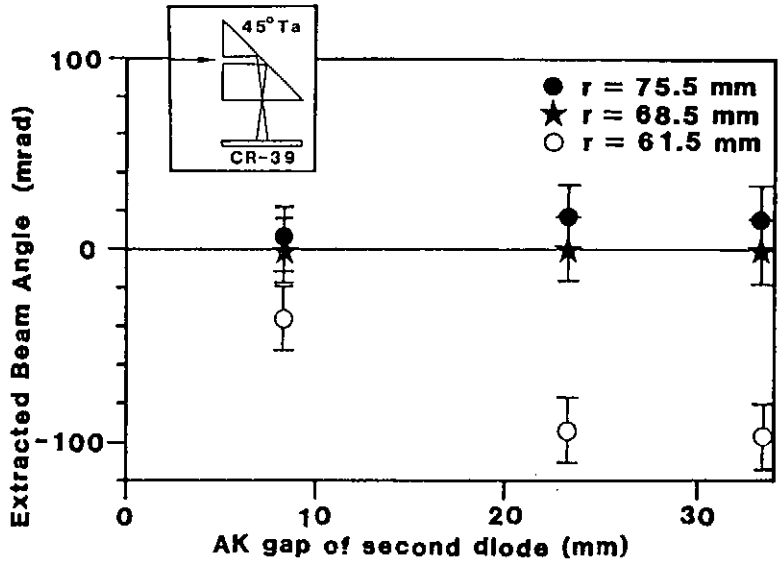

Fig.8 Measured beam trajectory in the two stage diode. The data at z = 26.2 mm shows radially split beam (carbon and proton) trajectories by the magnetic insulation field coil.

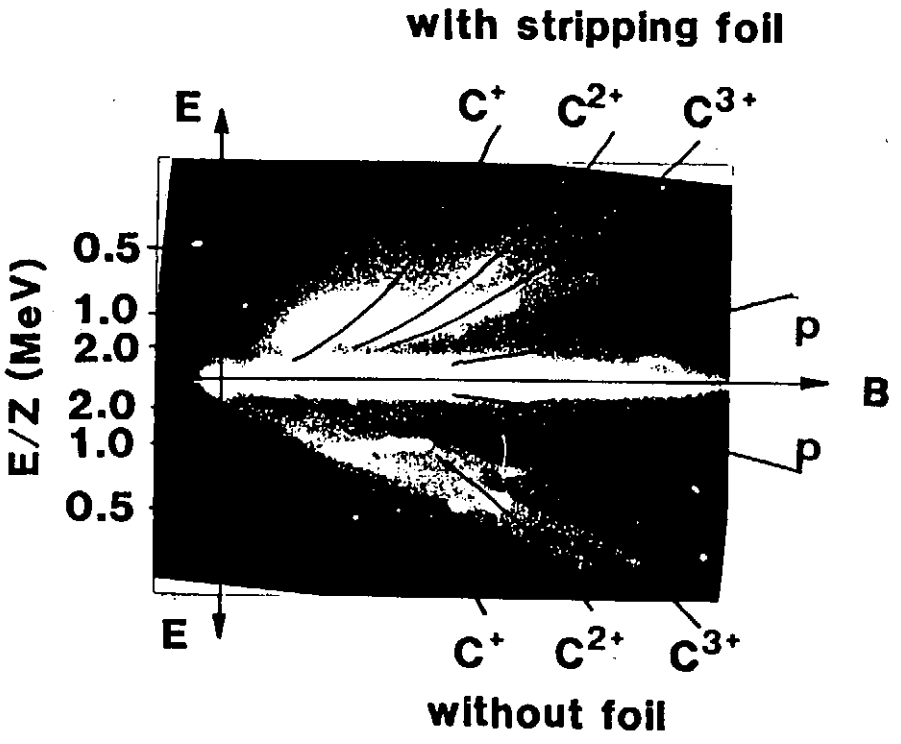

Fig.9 Thomson parabola traces with (a) and without (b) a stripping foil between two diode.

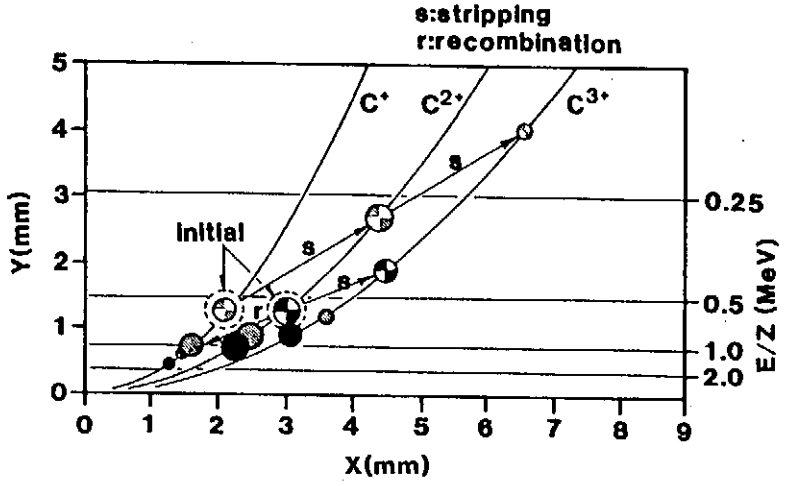

Fig.10 The calculated results of ion spectrum with a stripping foil and second diode acceleration. First stage of 0.6 MV and second stage of 0.5 MV are assumed.

Two-stage charge stripping diode

Thomson parabola traces are shown in Fig.9, with (a) and without (b) a stripping foil between two diode. Without stripping foil (lower half of Fig.9), the maximum energy of C^+ and C^{2+} ions are same value of about 1.1 MeV. Two-stage charge stripping diode (upper half of Fig.9) shows obviously different ion spectrum comparing with the non stripping case. The charge state equilibration of ions passing through a stripping foil is calculated from the charge stripping and the charge recombination cross sections. The calculated results of ion spectrum with the stripping foil is shown in Fig.10. The carbon ions C^+ and C^{2+} are stripped (or partially recombined) after acceleration at the first stage diode (W = 0.6 MV) and subsequently assume the acceleration energy of the charge state times the voltage of second diode (V= 0.5 MV). The maximum energy edges of each ion parabola traces are in agreement with the calculation.

This experimental result implies the possibility of two-stage charge stripping diode to obtain high energy ions suitable for the light-ion-beam inertial confinement fusion. If we use Li^+ ions of 6 MeV energy, almost all ions are stripped to Li^{3+} ions (>95 %) by an 0.01 micro-meter thickness foil and accelerated by 8 MV second diode assuming the final energy of 30 MeV. The multiple scattering angle of 6 MeV Li ions by the stripping foil is estimated to be less than 1 mrad and is sufficiently small for beam focusing.

IV. Summary

Two-stage ion diode experiments are performed on Reiden-SHVS induction adder accelerator. The diode impedance of first stage was adequately controlled by plasma injection ion source. Second stage diode, which is operated as ion beam injection diode, has the impedance characteristics of rapidly decreasing at pulse rise and gradually increasing during the later part of pulse. The ion current density of two stage diode is enhanced by the virtual anode formation. The ion beams are strongly deflected by the solenoidal lens geometry of diode insulation field coil and the virtual anode effect was relatively small. The two stage charge stripping diode is demonstrated, and the ion spectrum and ion charge state are in agreement with the calculation.

V. References

[1] R.N.Sudan and R.V.Lovelace, Phys. Rev. Lett. **31**, 1174 (1973).
[2] P.A.Miller, J. Appl. Phys. **57**, 1473 (1985).
[3] M.P.Desjarlais, Phys. Rev. Lett. **59**, 2295 (1987).
[4] J.B.Greenly et al., J. Appl. Phys. **63**, 1872 (1988).
[5] S.Miyamoto et al., Proc. 7th Int'l Conf on High Power Particle Beams, Karlsruhe, (1988), p.47 (Kernforshungszentrum Karlsruhe, Federal Republic of Germany), **AI2**.
[6] S.A.Slutz and M.P.Desjarlais, J. Appl. Phys., **67**, 6705 (1990).

EXPERIMENTS TOWARD THE DEVELOPMENT OF NEW PULSED ION DIODES

Kazuhiko HORIOKA, Naoki TAZIMA, Yasuhiro SAITO and Koichi KASUYA
Department of Energy Sciences, The Graduate School at Nagatsuta,
Tokyo Institute of Technology, Nagatsuta 4259,
Midori-ku Yokohama, Japan 227

Abstract

Laser-based diagnostic methods are developed to improve our understanding of the behavior of a flashover-type magnetically-insulated, pulsed-ion diode. Effects of neutral particles on the diode characteristics are examined with laser resonant interferometry. For the quantitative estimation of the particle density, a laser resonance scattering method is also applied. These techniques could allow direct determination of the particle distribution in the diode gap.

A new diode which uses actively produced source plasma is developed for the investigation of the anode plasma effect on the diode characteristics. Two types of diode configurations are tested, over a wide range of pulse delays and peak flux of the source plasma injection.

I. INTRODUCTION

Although magnetically insulated flashover-type pulsed ion sources can be operated at TW power level, they have also some drawbacks; impurity of the extracted beam and impedance characteristics of the gap. Generally the impedance of this type of diode falls rapidly with time, which is undesirable from the point view of the coupling efficiency with the pulse power generator and the energy spectrum of extracted beam.

A large amount of emission of neutral particles in the initial phase seems to be significant and inevitable process for the anode plasma formation.[1] Any energetic neutrals emitted by the flashover process can freely travel across the magnetic field in the diode gap, which can degrade the diode characteristics.[2,3] For space charge limitted condition, the total charge (ions and electrons) in the A-K (Anode-Cathode) gap must remain zero. It brings 'bootstrap' behavior in the diode gap ie; increase of the ion current density induces electron emission into the A-K gap which further induces ion emission[8].

To increase the spacial and temporal focusability of the beam, our understanding of the diode gap behavior must be improved. The development of a new diode which has non-flashover ion source may be the highest priority. In this report, an advanced diagnostic method for the investigation of the gap behavior is proposed[4] and preliminary results are shown. Two types of diode configurations are tested for the investigation of anode plasma effects on the conventional passive flashover ion diode.

II. LASER DIAGNOSTICS OF A-K GAP

II-1 EXPERIMENTAL SET-UP

A schematic diagram of the experimental set-up is shown in Fig.1. An applied-B_r magnetically insulated extraction diode was driven with a 5Ω-60ns Blumlein line. The beam ions are extracted from a surface flashover plasma of a dielectric material (Paraffin Wax; $(CH_2)_n$) on the anode surface. The diode typically delivered ion current densities of 50-100A/cm^2 at nominal diode voltage of 200-300kV, d=4mm and B/B^*=1-2, where d is the width of anode cathode gap, B denotes the insulation magnetic field in the gap and B^* is critical value.

The behavior of hydrogen atoms in the diode gap was investigated with an interferometric technique and measurements of hydrogen Balmer alpha (H_α) fluorescence induced by a resonant laser injection. The homogeneous line width of the H_α line emitted from the source plasma was Stark broadened ($\Delta\lambda = \sim 0.2$nm) and was correspondingly larger than the laser bandwidth. The laser light was introduced into a Mach-Zehnder interferometer. The H_α fluorescence induced in the plasma was measured at a 20° scattering angle.

II-2. EXPERIMENTAL RESULTS

RESONANCE INTERFEROMETRY

To measure the quantitative behavior of neutral particles in the gap, we are developing a resonant interferometric technique, because the sensitivity of the conventional interferometric method is too low for the measurements.

The enhanced refraction n_r is given approximately as,

$$n_r - 1 = \frac{r_0 f}{4\pi} \frac{\lambda^3}{\lambda - \lambda r} N_l \left(1 - \frac{g_l N_u}{g_u N_l}\right) \qquad (1)$$

where λ is the wavelength, f is the absorption oscillator strength, r_e is the classical electron radius, N is the atomic number density, g is the statistical weight and subscript r, u, l denote the resonance state, upper and lower resonance level, respectively.

The refraction induced by the plasma electron can be expressed as,

$$n - 1 = -4.49 \times 10^{-28} \lambda^2 n_e \qquad (2)$$

here, n_e is the number density of plasma electron in cm^{-3} and λ is the wavelength in nm. For example, when $\Delta\lambda$=0.1nm, and at the H_α line (656.3nm), their contribution to the refractivity can be written as follows,

$$n - 1 = a(1.42 \times (10^{-2} N + 10^3 N_r) - n_e) \qquad (3)$$

and also when $\Delta\lambda$=-0.1nm, it is written as,

$$n - 1 = a(1.42 \times (10^{-2} N - 10^3 N_r) - n_e). \qquad (4)$$

For off-resonance line, it is expressed as,

$$n - 1 = a(1.42 \times 10^{-2} N - n_e) \qquad (5)$$

where a is constant (1.93×10^{-22}), $N_r=N_l(1-(g_lN_u/g_uN_l))$ and N is the hydrogen atomic number density (cm^{-3}). We can estimate those three values (N_r, N, n_e) by the measurement of the fringe shift at three wavelengths ($\lambda = \lambda r+\Delta\lambda$, $\lambda= \lambda r-\Delta\lambda'$, and $\lambda= \lambda$ off), here subscript "off" means off-resonance state.

An example of the interferometry is shown with a typical oscillogram of the pulse line output voltage(V_{BL}) in Fig.2. Here, the probe laser light of 0.07nm bandwidth was tuned to the wavelength of 0.08nm longer than the center wavelength of the Hα. As can be seen with this figure, it was observed that the fringe shift by the electrons (shown in the photographs numbered 4 and 5 in Fig.2) follows that by the neutral hydrogen (typically shown by the photograph of No.3). This result qualitatively supports the plasma expansion model, which explains that fast plasma expansion of the pulsed ion diode is induced by charge exchanged high energy neutral particles.[2)]

However, as shown in Eq.(1), the resonance interferometry merely gives information about the population difference N_r of the transition.[4)]

RESONANCE SCATTERING METHOD

For the quantitative estimation of the particle density, the resonance scattering of laser light was measured. The spectral width of the dye laser was 0.07nm centered at Hα line. The Hα fluorescent scattered light was focused on the optical fiber, which has rectangular shape and 7m in length, guided to a 50cm monochromator (JASCO CT-50C) and observed using a HAMAMATSU R2257

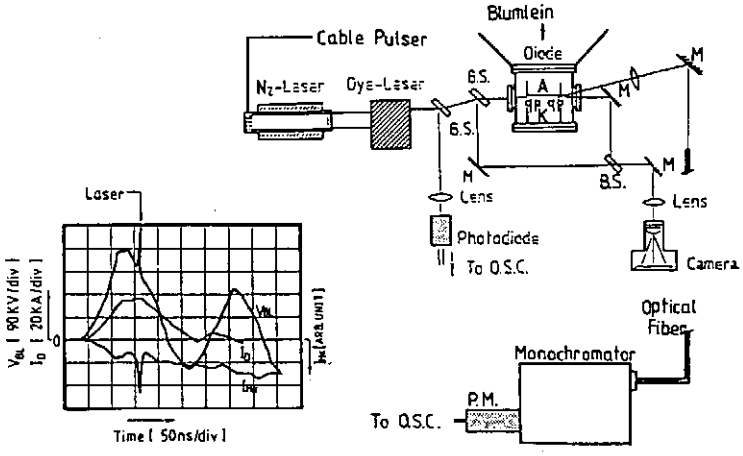

Fig.1 A schematic diagram of experimental setup

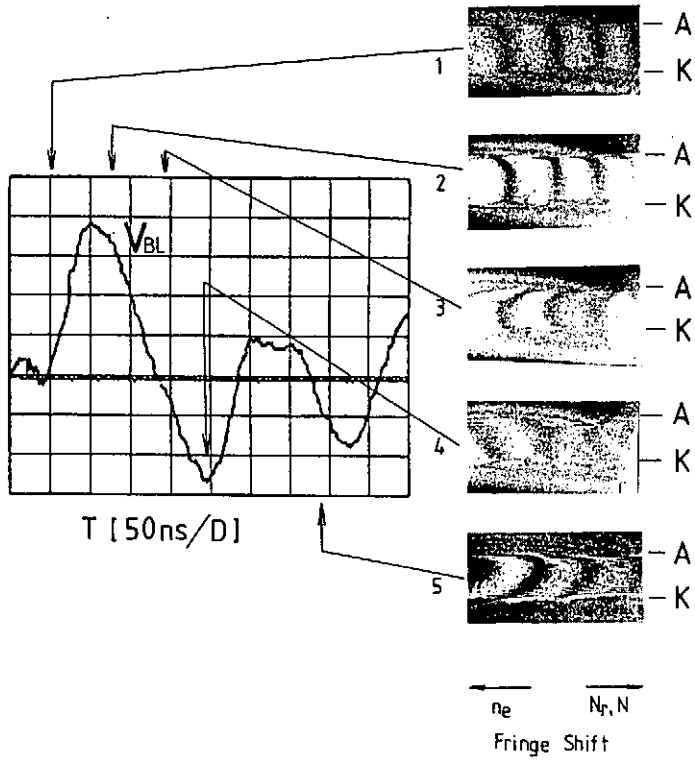

Fig.2 Resonance interferometry of the gap as a function of diode time T (A; Anode, K;Cathode)

photomultiplier. The image of the gap was formed on the rectangular fiber, which determined the spatial resolution. The scattered light from the anode plasma of 1mm thickness was detected together with the background Hα intensity. A typical oscillo-trace of the photomultipier output is shown in Fig.3, where T shows the time from the rise of diode voltage. In response to the incident laser light, the Hα light emission increased two to three times compared with the background level.

At the saturation condition, the ratio of the population between the upper and the lower level can be written by,

$$\frac{N_2^s}{N_3^s} = \frac{g_2}{g_3} \qquad (6)$$

and the sample becomes completely transparent. Here g is the statistical weight (in our case $g_2/g_3=4/9$), and the superscript s denotes the saturating condition.

By the intense laser injection, the Hα intensity rises rapidly from the initial background level corresponding N_3 to a peak value. On the other hand the fluorescence light is proportional to the upper level population. Hence the ratio of the transient peak ($I'_{H\alpha}$) and the background ($I_{H\alpha}$) Hα fluorescence provides a measure of the ratio of initial level population N_2/N_3 as follows,

$$\frac{N_2}{N_3} = \frac{g_2 + g_3}{g_3} \frac{I'_{H\alpha}}{I_{H\alpha}} - 1 \qquad (7)$$

On the condition that the laser intensity is at an

intermediate level, quantitative results relate largely to collisional or radiative rate for the resonance levels, which decides the effective decay rate ie; effective saturation intensity.[6] The saturation intensity must be determined by measurements of the fluorescence intensity as a function of the injection level of the probe laser light. In principle, therefore, provided that the saturation level of the incident laser light is precisely monitored, we can estimate the population ratio without an absolute calibration of the system.

III. EXPERIMENTS AT PLASMA INJECTION MODE

III-1 EXPERIMENTAL SET-UP

A Br-magnetically insulated diode driven by a 5Ω-60nsec pulse forming line was used for the expriments. An equivalent circuit of the flashboard section is shown in Fig.4. The anode plasma was actively supplied with four segmented flashboard which is inductively isolated from driving capacitor C_D. The source flux was controlled with the charging voltage and timing of the activation.

Figure-5 shows the schematic of the diode section. Two types of configuration were tested. The first version (version-1) used flashboard directly attached on the anode surface of the Br-extraction diode. Then the dielectric surface was directly exposed to the A-K gap. The second version (version-2) used a flashboard-type plasma gun placed 1cm behind from the anode surface made from a perforated Al disk. The perforated Al plate excludes the insulation field and stagnates the injected plasma. Then the Al plate defines the ion emitting surface.

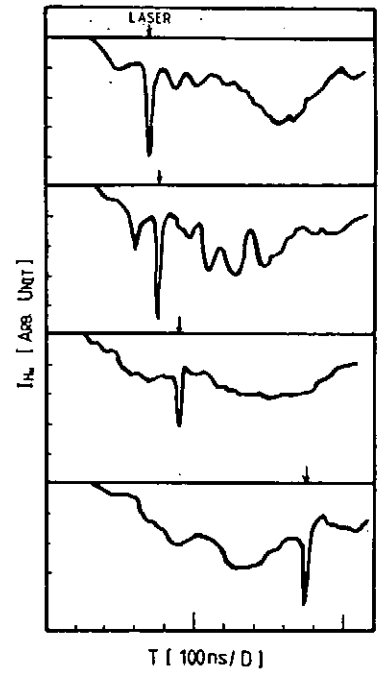

Fig.3 Typical signals of Hα light emission from source plasma

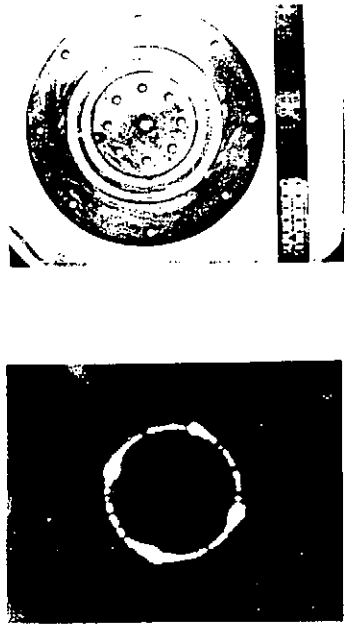

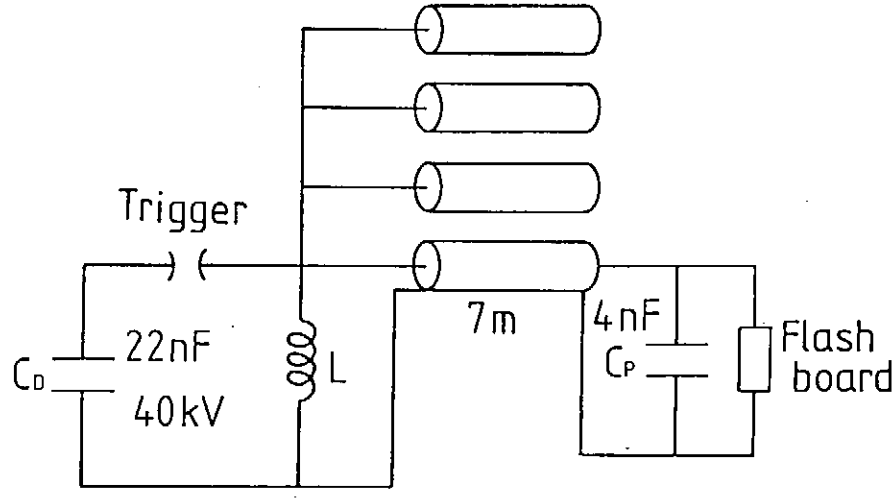

Fig.4 Equivalent circuit of the flashboard and front view of the flashboard

III-2 EXPERIMENTAL RESULTS

Typical traces of the diode voltage V_D and diode current I_D of the diode (version-1) is shown in Fig.6, with 'delay time' from the activation of the flashboard to the main voltage pulse as a parameter. The turn-on delay of ion current was improved by the plasma activation compared with conventional diode. However, as shown in the figure, when the delay was increased more than 100nsec, the diode impedance dramatically collapsed.

On the contrary, the version-2 diode was succesfully operated, over a wide range of the delay time and plasma flux. Typical waveforms of the V_D, I_D and the ion current density Ji for version-2 diode are shown in Fig.7. For the short delay mode, the ion current rised rapidly coincident with voltage rise, after that it gradually decreased probably because of ion depletion in the source plasma as the beam is extracted. Generally diode impedance was maintained at high value.

When the quantity of plasma injection was further increased the ion current density increased more than Child-Langmuir level and the rising impedance mode was appeared. The cause of initial low impedance phase is considered to be the effect of low density plasma pre-fill in the A-K gap.

Evidently impedance collapse of version-1 diode is caused by anode plasma effect including large neutral particles produced with flashover process.

IV. SUMMARY

The physics of the pulsed ion source has not yet been understood exactly, because of the difficulty of the diagnostics

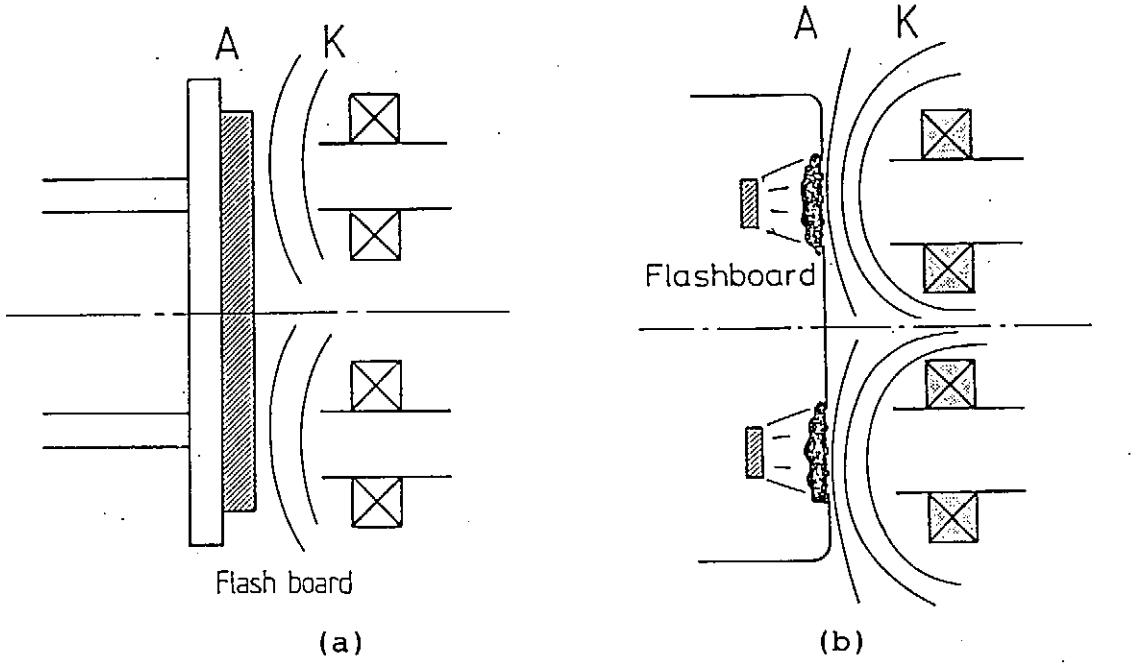

Fig.5 Schematic of diode sections (Version-1 (a), Version-2 (b))

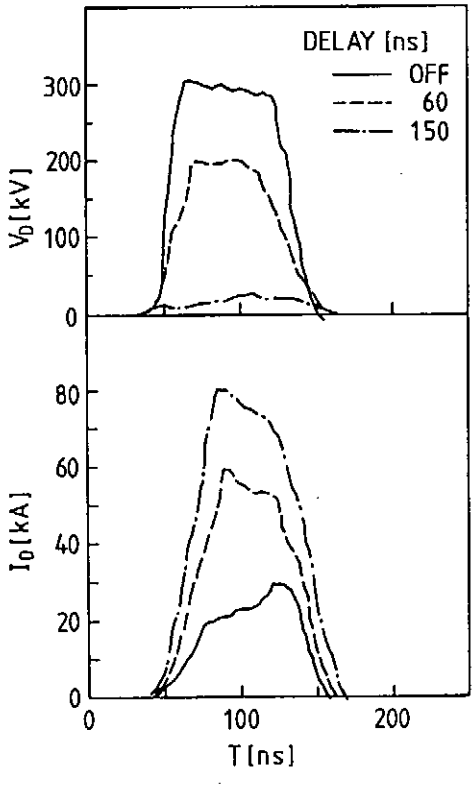

Fig.6 Typical oscillo-traces of V_D and I_D for version-1 diode with delay time as a parameter

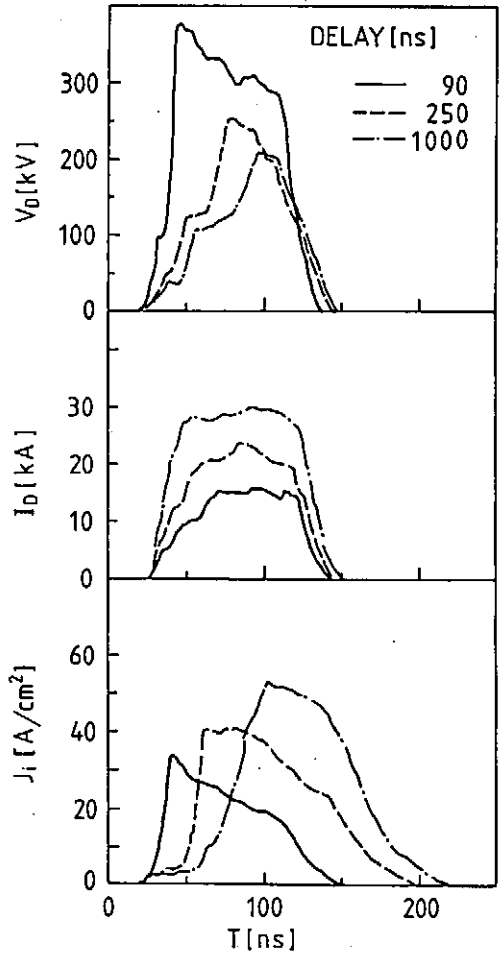

Fig.7 Typical oscillo-traces of V_D, I_D and J_i for version-2 diode

of the localized and highly nonequilibrium[7] electrode plasma.

New methods of laser diagnostics were developed for the investigation of the pulsed ion diode. The resonant interferometry detects the population difference of the transition and the resonance scattered light reflects the ratio of the population. With detection of the dispersion and the scattering of resonant light, the population density of N_2 and N_3 can be directly determined. The behavior of diode acceleration gap was observed with the resonant interferometry and laser induced fluoresence.

It was concluded that the most critical factor of the active diode of version-1 was the time delay of the main voltage pulse from the pre-ionization. In our experimental condition, it must be controlled 40-100nsec. Out of this range, the impedance characteristics was degraded severely, probably because of the invasion of plasma and neutral particles in the gap.

Generally, the second version was successfully operated ; high impedance was maintained through whole voltage pulse, at current level lower than the Child-Langmuir value. When the current level ie; plasma injection was increased, the rising impedance mode was appeared.

Obviously, much more work must be done but preliminary results exist ; the results qualitatively support the anode plasma expansion mechanism induced by the energetic neutral particles in the gap. To increase the operation range, a high flux capable of providing high current, neutral free, and high purity (including charge state purity), plasma source must be developed.

REFERENCES

1) K.Horioka, H.Yoneda and K.Kasuya;IEEE Trans. Plasma Sci., PS-17, 793 (1989)

2) D.S.Prono, H.Ishizuka, E.P.Lee, B.W.Stallard and W.C.Turner ; J. Appl. Phys., 52, 3004 (1981)

3) C.Litwin and Y.Maron; Phys. Fluids, B1, 670 (1989)

4) K.Horioka, N.Tazima and K.Kasuya; Rev. Sci. Instr. 61, 610 (1990)

5) J.R.Woodworth; private communication

6) D.D.Burgess, G.Kolbe and J.M.Ward; J. Phys. B, 11, 2765 (1978)

7) Y.Maron; Proc. 7th Int. Conf. High Power Particle Beams; BEAMS'88., Ed.by W.Bauer and W.Schmit, July 4-8, Germany Karlsruhe, A13, 57 (1988)

8) T.Aoki and K.Niu; in this proceedings

STUDY ON ABLATION OF TARGET MATERIAL INDUCED BY PULSED ION BEAM BOMBARDMENT

S. Kamihata, A. Kitamura, Y. Furuyama and T. Nakajima

Department of Nuclear Engineering,
Kobe University of Mercantile Marine,
Fukaeminami-machi 5-1-1, Higashinada-ku, Kobe 658, Japan

Abstract

Process of ablation due to irradiation of medium power pulsed ion beams (PIB) with a power level of 10^7-10^8 W/cm^2, which have been proved useful for material processing, is investigated with use of a charge collector method and a "collector-RBS method". In the letter, the ablation particles are collected onto a silicon probe surface, which is later subjected to Rutherford Backscattering Spectroscopy (RBS). Preliminary results of measurements on the ablation mass as a function of the ion current density and the target material and on the ion energy include some interesting features, which must be followed by further investigation.

§1. Introduction

Application of medium-power (>10^7 W/cm^2) pulsed ion beams (PIB) to material processing is of growing interest owing to their unique feature of energy deposition; instantaneous deposition of energy into a localized region of a target restricted to the particle range, and subsequent rapid cooling [1].

Following the first application of PIB to annealing of materials [2], interest has been concentrated on reformation of the target structure irradiated with PIB [1,3,4,5,6,7,8,9]. Mixing of atoms and formation of various novel compounds which are difficult to produce through conventional methods have been found. Efforts have been also concentrated on improvement of the mechanical properties of the irradiated target surfaces, such as wear resistance and microhardness [10,11,12,13].

Recently, successful formation of thin films from the ablation plasma induced by PIB bombardment has been reported [14,15]: ion beams with power density greater than 10^9 W/cm^2 were used to form electroluminescent ZnS:Mn films of submicrometer thickness. They also have succeeded to form thin films of $YBa_2Cu_3O_{7-x}$, $TiBaO_3$, apatite and carbon [16]. Such a method of thin-film deposition has distinctive features that the deposition occurs in much shorter period of time from the ablation plasmas having much higher density than in conventional plasma methods. In addition, feedom in chosing the material and high controllability of the plasma temperature are the great advantages of this PIB evaporation technique, making this method very atractive.

However, it is not always clear how the film properties are influenced by the characteristics of the ablation plume, such as electron temperature, ion energy, ionization degree, etc. In the present study, we examine the basic characteristics of the ablation plumes produced by pulsed ion beams of 10^7-10^8 W/cm^2. In addition to the chrage collector method to measure the ion energy and flux of the plume, a collector-RBS method is applied for the measurement of total fluence. The latter is similar to the surface probe method used as a powerful diagnostic method for

boundary plasmas in magnetically-confined fusion experiments [17,18].

§2. Experimental procedure

A schematic of the PIB irradiation system is shown in Fig.1. Pulsed ion beams of 50 ns duration with current density of 1 kA/cm^2 were produced with a pinched electron beam diode with a polyethylene anode, which was operated at an anode voltage of 400 kV fed by a 5-kJ pulse power source Eridatron-Ⅱ [19]. The beam composed of 80% protons and 20% carbon ions induced ablation on the target; Pb, Cu, Mo, Ti, Fe or W.

The ablation particles were collected with a Si collector probe at three different angular locations, which is later subjected to the Rutherford Backscattering Spectrometry (RBS) analysis using an MeV-accelerator. For measuring the ion component of the ablation particles, the Si collector was replaced with a charge collector probe. It contains 2 collector electrodes separated from each other by 16 mm for the purpose of time-of-flight measurements with an oscilloscope. A bias voltage of up to -100 V was applied to the electrodes. The beam current density on the target was controlled by moving the target-collector assembly axially. The irradiation system was maintained at a pressure below 1.5×10^{-2} Pa.

A schematic of the RBS system is shown in Fig.2. The Si collector plate having ablation particles on it is analyzed with a probe beam of 1-MeV C^+ ions from a tandem Pelletron accelerator [20]. The beam diameter on the Si collector sample was 0.5 mm, which was small enough to restrict the analyzing area to the area corresponding to the interested irradiation point on the ablation target. Carbon was chosen as the probe ion, taking advantage of its high resclution for the present combination of the substrate Si and the material to be analyzed (Pb, etc.). An example of the energy spectra measured with the silicon surface barrier detector is shown in Fig.3. Good isolation of the Pb peak from the substrate Si signal is realized. The number of ablation Pb particles is calculated from the integrated counts of the Pb peak.

§3. Results and discussion

The angular dependence of the particle fluence in the ablation plume measured with the Si probe is shown in Fig.4, where the fluence data for several target materials under irradiation with 240 A/cm^2 PIB are normalized to the value of cosθ at θ=39°. A fair agreement of the angular distribution with the cosine law is observed in the measured range of angle.

Integrating the fluence distribution over the half space under the assumption of the cosine distribution, we get the ablation mass expressed as target thickness T_a removed due to the ablation. A correlation is observed between the removed thickness T_a and the normalized deposition energy E_n which is defined as the deposited energy within the particle range divided by the energy neccessary for heating the target up to the boiling point. The dependence of T_a on E_n is shown in Fig.5 for the case of 240 A/cm^2 irradiation. An abrupt increase of T_a at E_n=1 means that the sublimation energy is the threshold value for ablation. The data for Pb suggests a nonlinear increase of T_a with further increasing E_n. This is closely related to the dependence on ion current density j_i shown below.

In Fig.6 the removed thickness T_a for the Pb target is plotted as a function of j_i. The abrupt increase of T_a at j_i=30 A/cm^2 shows the ablation threshold again. Above the threshold, T_a does not increase linearly with j_i. This behavior can be understood from the fact that the heated region does not increase with increasing j_i. The tendency that T_a rather decreases toward higher j_i might suggest that the fluence distribution becomes forward peaked at high j_i. It is also interesting to note that the saturation value of T_a is much smaller than the particle range in the target. The further discussion requires more detailed measurements on the angular distribution of the particle fluence.

Typical traces recorded with the charge collector probe are shown in the inset of Fig.7, which shows evolution of the ion component of the ablation plume from the Pb target irradiated with 240 A/cm^2. The lower trace is from the collector near the target, while the upper from the farther one. From the time-of-

flight plots of 2 peaks shown in Fig.7, the velocities of the first and the second component are deduced to be 6×10^4 m/s and 8×10^3 m/s, respectively. It is reasonable to assume that these are due to adsorbed hydrogen ions with mean energy of 18 eV and Pb ions with 67 eV, respectively. It is interesting to note that the ion energies are rather low compared with those reported for the ablation plasma generated by KrF laser irradiation [21]. Further investigation is required also in this respect.

§4. Concluding remarks

The characteristics of the ablation plumes induced by PIB with a power level of 10^7-10^8 W/cm^2 are investigated with use of a collector-RBS method in addition to the charge collector probe. The preliminary results include some interesting features, which must be followed by further investigation.

Thanks are due to Mr. S. Niina for his help in the measurements.

References

[1] K. Yatsui: Proc. 7th Int. Conf. on High Power Particle Beams, Karlsruhe, West Germany, (1988)283; Laser & Particle Beams 7(1989)733.

[2] R.T. Hodgson, J.E.E. Baglin, R. Pal, J.M. Neri and D.A. Hammer: Appl. Phys. Lett. **37**(1980)187.

[3] J.E.E. Baglin, R.E. Hodgson, W.K. Chu, J.M. Neri, D.A. Hammer, and L.J. Chen: Nucl. Instr. & Meth. **191**(1981)169.

[4] T. Brat, M. Eizenberg, R. Fastow, C.J. Palmstrom and J.W. Mayer: J. Appl. Phys. **57**(1985)264.

[5] R. Fastow, J.W. Mayer, T. Brat, M. Eizenberg and J.O. Olowolafe: Appl. Phys. Lett. **46**(1985)1052.

[6] K. Kamata et al.: Laser & Particle Beams **5**(1987)495.

[7] Y. Nakagawa, T. Ariyoshi, M. Itami and Y. Fujii: Jpn. J. Appl. Phys. **27**(1988)L719.

[8] Y. Nakagawa et al.: Proc. 7th Int. Conf. on High Power Particle Beams, Karlsruhe, West Germany, (1988)1475.

[9] A. Kitamura, N. Sasaki, T. Nakajima and S. Yano: Proc. 7th Int. Conf. on High Power Particle Beams, Karlsruhe, West Germany, (1988)791.
[10] A.N. Didenko et al.: Nucl. Instr. & Meth. **B27**(1987)421.
[11] I.F. Isakov, A.E. Ligachev, A.D. Pogrebnjak and G.E. Remnev: Nucl. Instr. & Meth. **B28**(1987)37.
[12] S.A. Chistjakov, A.D. Pogrebnjak and G.E. Remnev: Nucl. Instr. & Meth. **B42**(1989)342.
[13] A.D. Pogrebnjak, G.E. Remnev and I.G.Romanov: Nucl. Instr. & Meth. **B43**(1989)41.
[14] Y. Shimotori, M. Yokoyama, H. Isobe, S. Harada, K. Masugata and K. Yatsui: J. Appl. Phys. **63**(1988)968.
[15] Y. Shimotori, M. Yokoyama, S. Harada, K. Masugata and K. Yatsui: Jpn. J. Appl. Phys. **28**(1989)468.
[16] K. Yatsui: lecture notes on Production and Control Technology of Plasma and Its Application (Japan Society of Plasma Science and Nuclear Fusion Research, 1989) p.93.
[17] D.M. Manos and G.M. McCracken: in Physics of Plasma-Wall Interactions in Controlled Fusion, ed. D.E. Post and R. Behrisch (Plenum Press, New York, 1986) p.135.
[18] T. Nakajima, I. Takaya, T. Akiyama, A. Kitamura, S. Yano, S. Sengoku, H. Ohtsuka and H. Maeda: Proc. 4th Int. Conf. on Fusion Reactor Materials, Dec. 4-8, 1989, Kyoto. (in press)
[19] A. Kitamura and S. Yano: Jpn. J. Appl. Phys. **21**(1982)L354.
[20] A. Kitamura, T. Nakajima and S. Yano: Proc. 8th Symp. on ISIAT'84, June 4-6, 1984, Tokyo, p.149.
[21] P.E. Dyer: Appl. Phys. Lett. **55**(1989)1630.

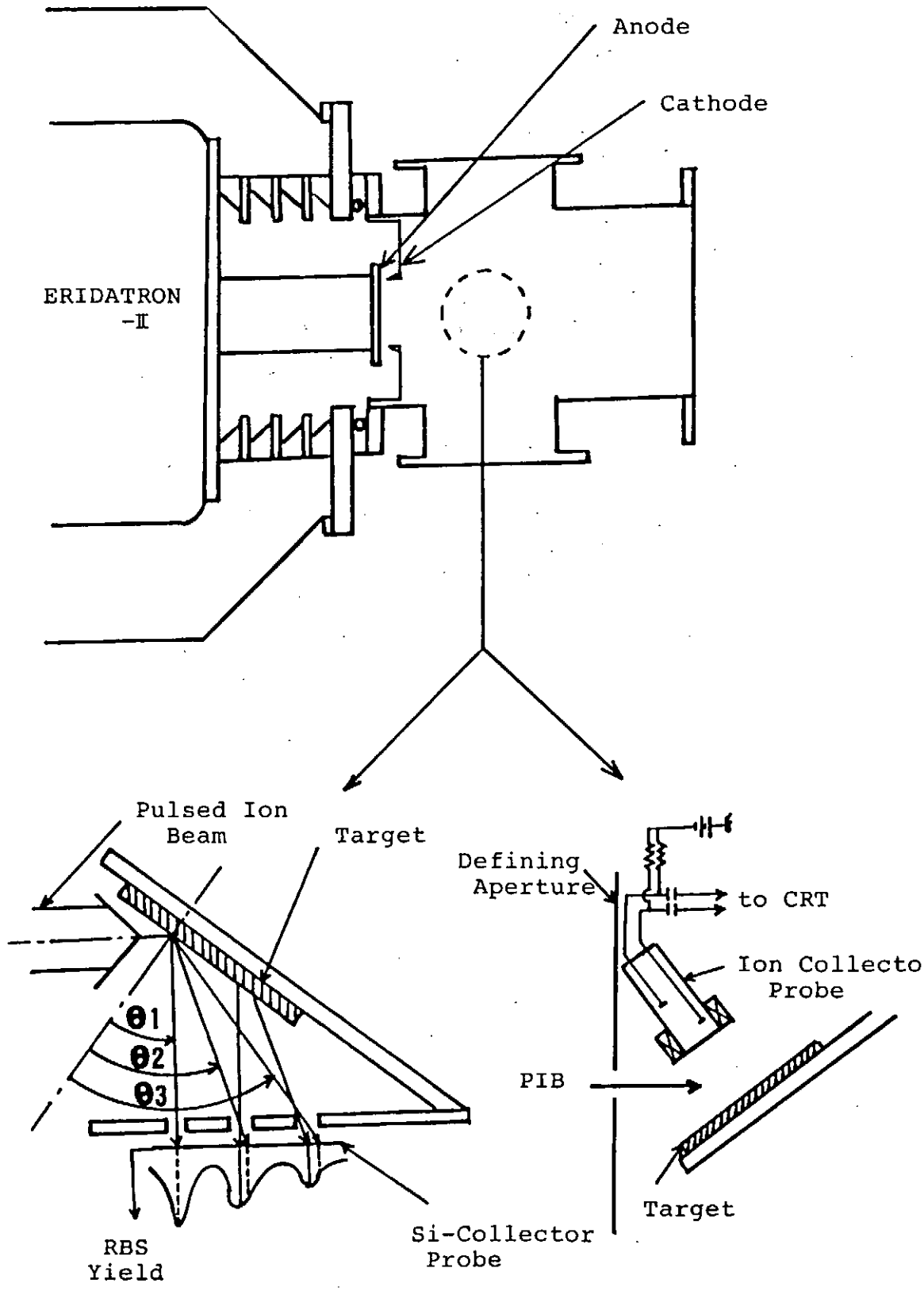

Fig.1. Schematic of PIB irradiation system with Ion collector Probe and Si-Collector Probe.

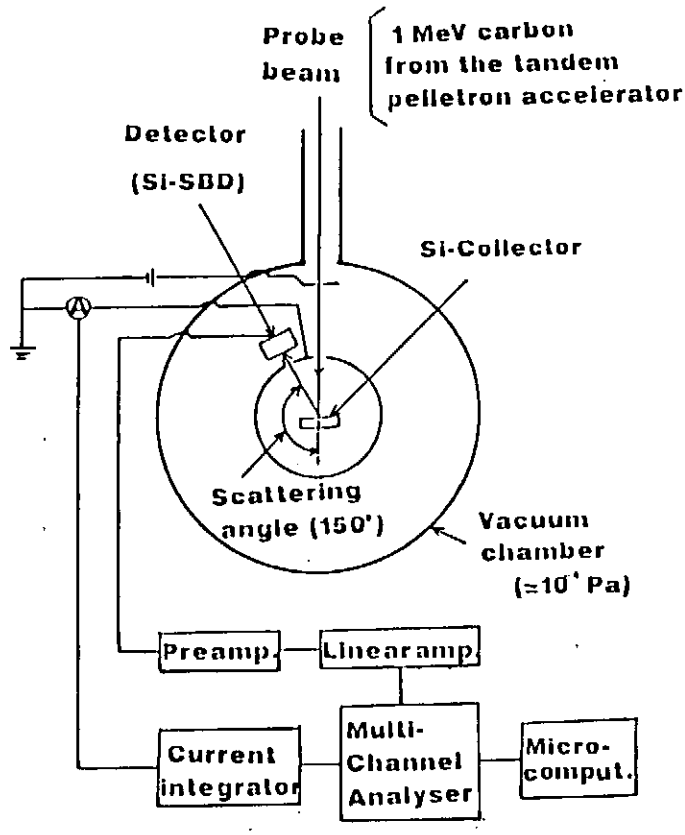

Fig.2. Schematic of RBS system.

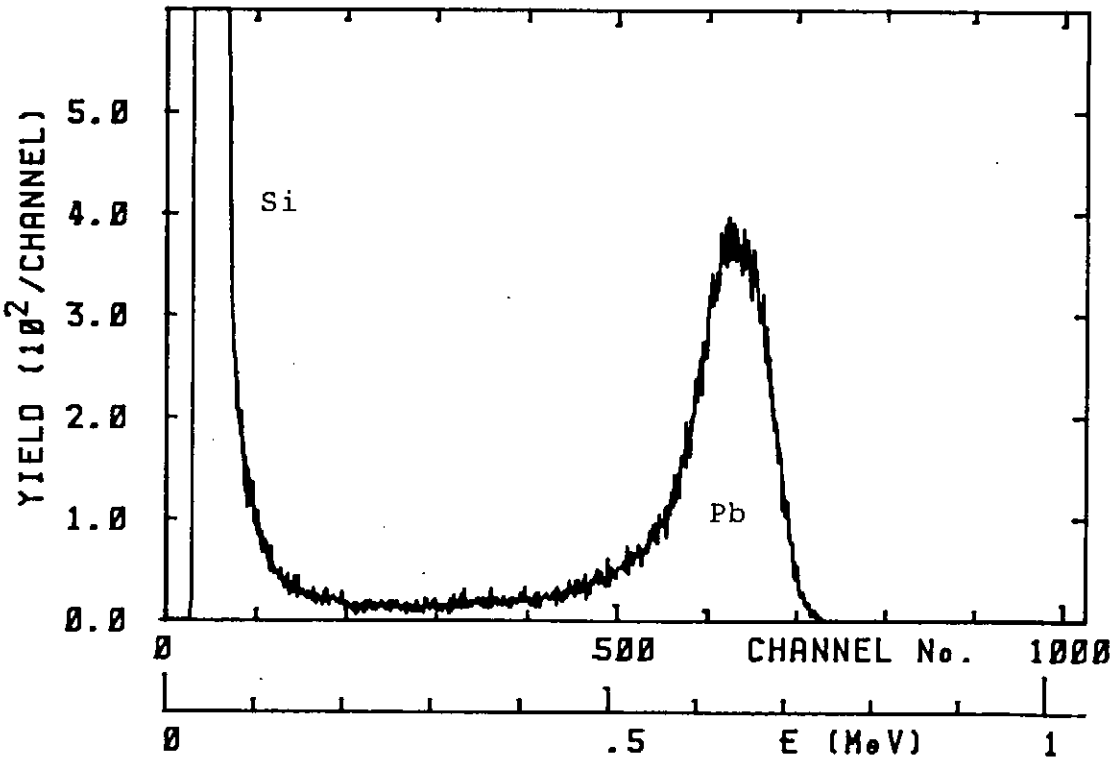

Fig.3. Typical RBS spectrum.

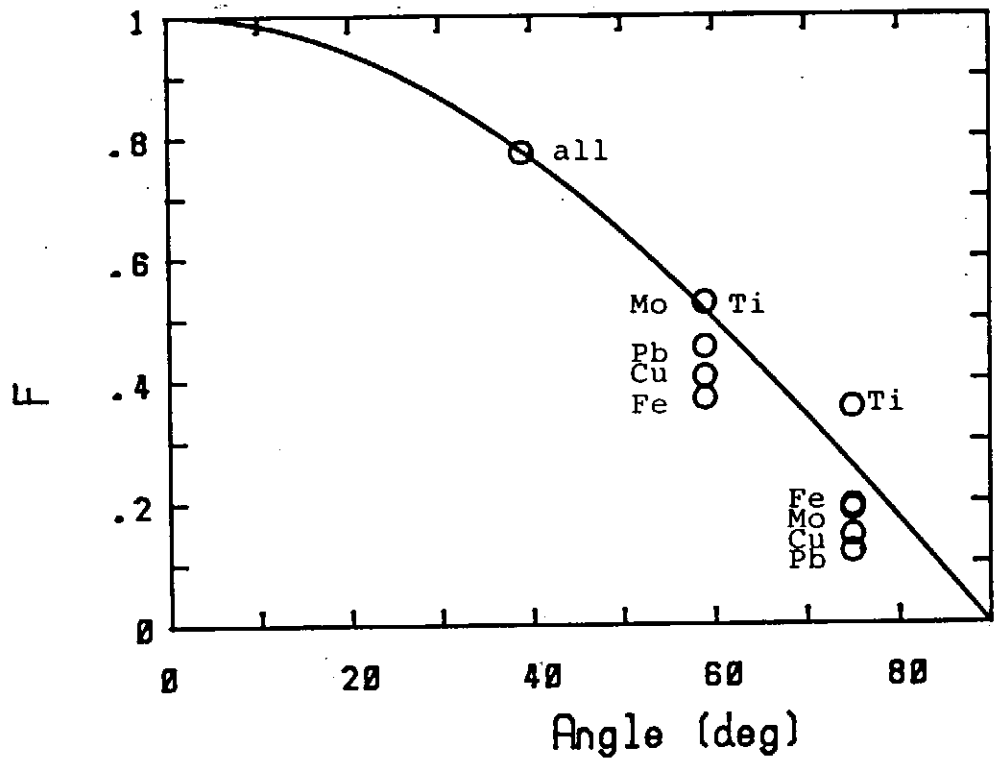

Fig.4. Angular dependence of ablation particle fluence F normalized to fit on the cosine distribution.

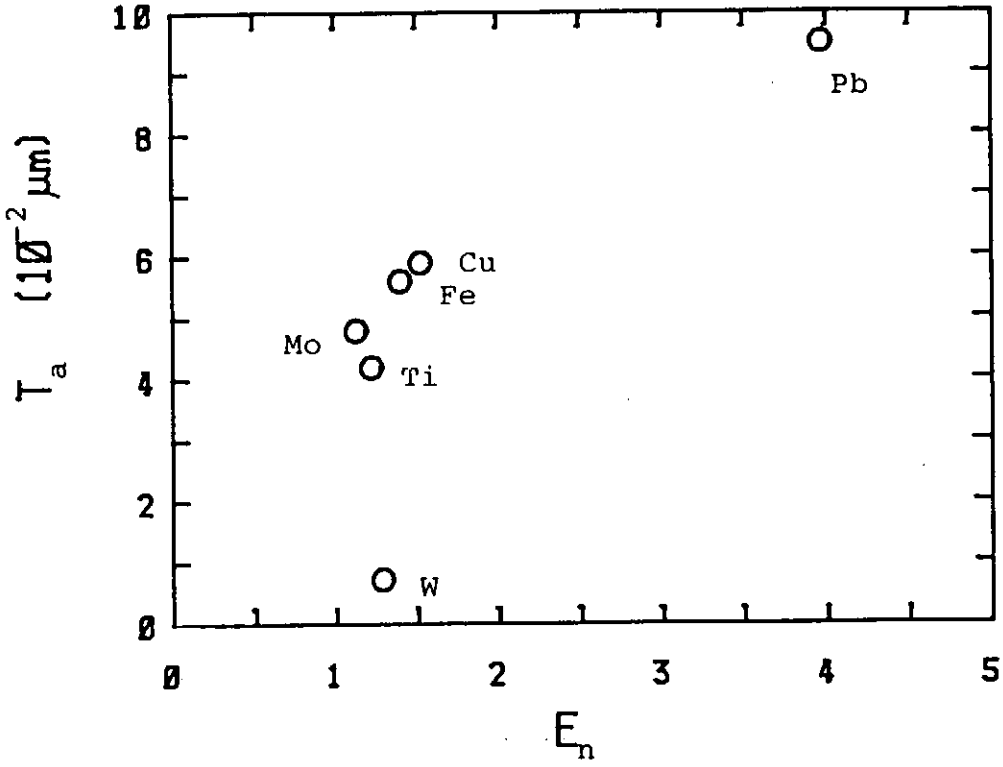

Fig.5. Dependence of ablation thickness T_a on deposition energy normalized to the sublimation energy.

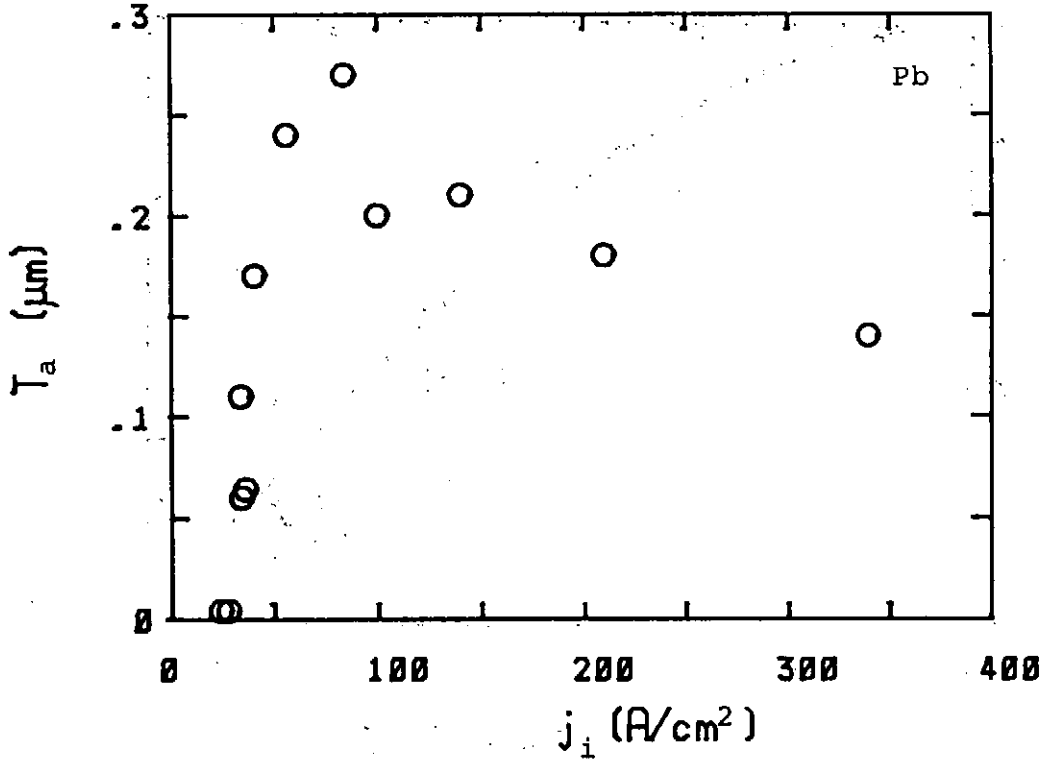

Fig.6. Dependence of ablation thickness T_a on irradiation current j_i.

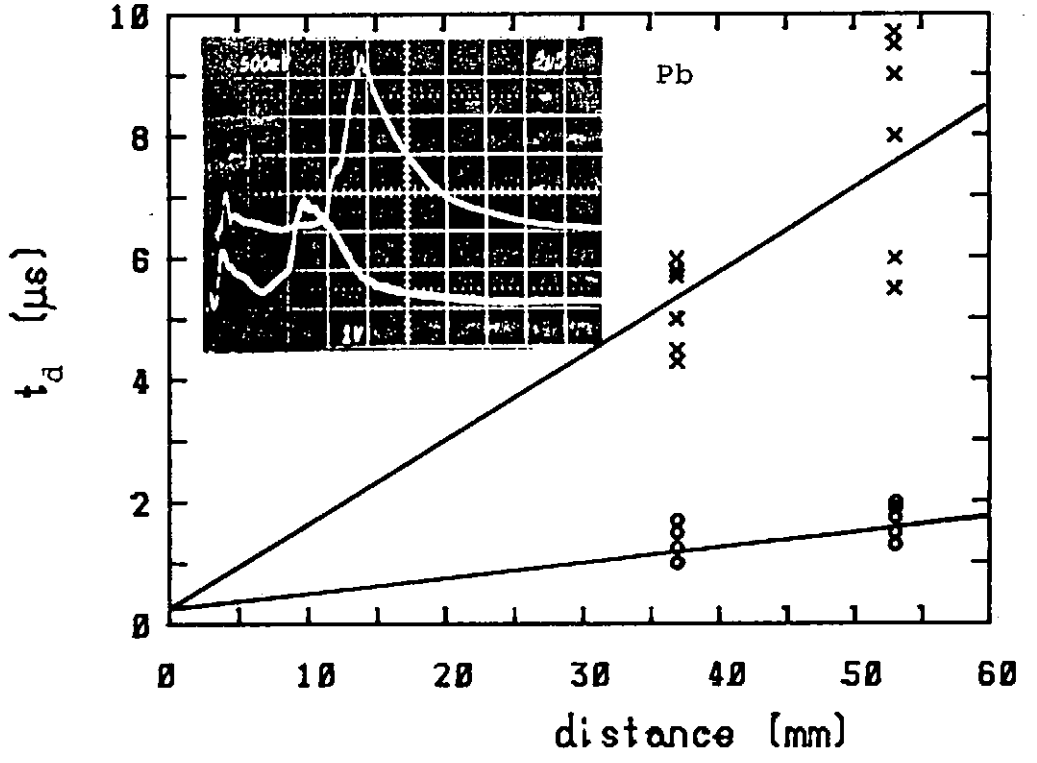

Fig.7. Time-of-flight plot of two peaks observed with ion collectors. The inset shows typical spectrum.

Theoretical Study of "Plasma Focus Diode"

Weihua Jiang, Katsumi Masugata and Kiyoshi Yatsui
Laboratory of Beam Technology, Nagaoka University of Technology,
Nagaoka, Niigata 940-21, Japan

Abstract

A theoretical model of self-magnetically insulated, coaxial type ion beam diode, "Plasma Focus Diode" (PFD), is developed and analyzed in detail. In this theory, self-consistant electron current and space-charge limited ion current are incorporated. The steady-state charge and current distribution inside the diode is calculated for given diode voltage. We compare the calculated diode impedance with the experimental results obtained at the peak power, and good agreement was obtained. Some diode behaviours observed in the experiments are explained by the theory. From the theoretical understanding about PFD, we obtain the scaling relations of diode impedance and the ion-current efficiency, and use them to discuss the possible ways to improve the diode operation.

I. Introduction

Intense pulsed light-ion beam (LIB) has been studied for many years for applications in inertial confinement fusion (ICF) and material prosessing.[1,2] In these studies, both the generation and focusing of LIB are very important subjects.

We have previously introduced coaxial type, self-magnetically insulated ion-beam diode, "Plasma Focus Diode" (PFD).[3-5] The principle of PFD is shown schematically in Fig. 1. Two coaxial cylinders basically form the diode to which the pulse power is fed

from one side. The anode plasma is generated by earlier leakage of electrons and/or flashover on the anode surface made of epoxy. Most electrons are moving mainly in the axial (z) direction due to E × B drift. The ion emission from the anode plasma is enhanced by the space-charge of the drifting electrons. Through a perforated cathode, the ions tend to focus to the center line.

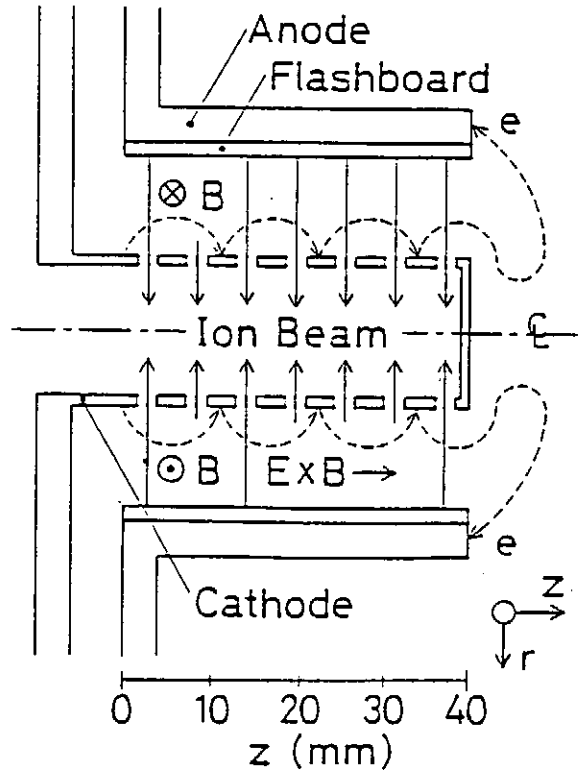

Fig. 1 Basic principle of PFD.

Compared with other kinds of ion diode, PFD is found to be very attractive mainly in its good focusing. In coaxial type applied-B diode, the magnetic field is usually in the axial direction. Experimentally, it is difficult to compensate the influence of the axial magnetic field on azimuthal momentum of ions, which limits the focusability at the center line. In PFD, however, the magnetic field generated by every current component is in the azimuthal (θ) direction so that only the axial (z) momentum of the ions is affected by the magnetic field while the θ-momentum keeps zero theoretically. In addition, we are able to make PFD with small radial size because no external field coil is required. As a result, the focusability of PFD in radial (r) direction is better than any other diodes. The tight focusing gives very high beam power density on the center line. Line focusing can also be interesting in some applications other than ICF.

Typical experimental data of PFD, as reported previouly,[6-10] can be summarized as follows: focusing radius = 0.18 ~ 0.25 mm, ion-

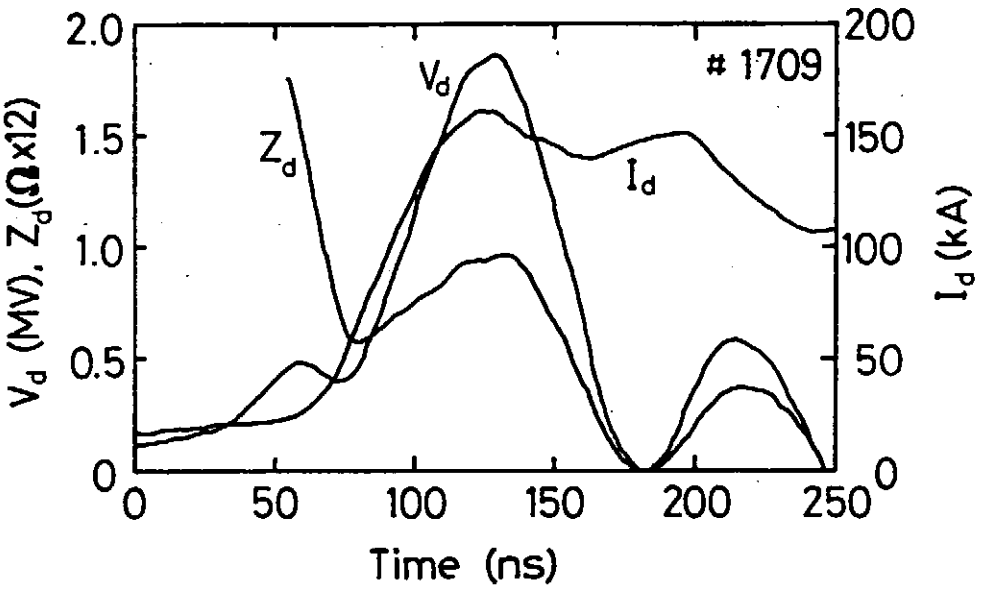

Fig. 2 Typical waveforms of inductively-corrected diode voltage (V_d), total diode current (I_d), and diode impedance (Z_d). Shot No. 1709. Here, r_c (cathode radius) = 11 mm, r_a (anode radius) = 18 mm, and L (axial length) = 40 mm.

current density at the anode surface = 1.4 ~ 1.9 kA/cm^2, ion-beam power density at focusing region ~ 0.1 TW/cm^2 (for ion energy of 1.5 MeV).

Figure 2 shows the typical waveforms of inductively-corrected diode voltage, total diode current and impedance of the diode. From Fig. 2, we see that the diode impedance is ~ 12 Ω at the peak power and then falls very rapidly to nearly zero before the end of the power pulse. The internal impedance of our pulse forming line is 6.5 Ω.

The impedance behaviour of PFD is always a problem in diode operation. It has been experimentally observed that breakdown usually happens at sometime in the main pulse. For obtaining a longer impedance lifetime, we have to increase the A-K gap and then the impedance is increased as a result. Another problem is the ion-current efficiency. For PFD, we are able to lengthen the diode to increase the ion efficiency by lengthening the transition time of electrons in the diode. However, "overlengthening" usually causes the similar breakdown problem. In addition, the breakdown is easily affected by many uncertain factors in the diode and become very unstable. As a result, the reproducibility of PFD operation

is poor. For solving these problems, it is necessary to understand behaviour of PFD theoretically.

The behaviour of applied-B diodes has received intensive studies by many authors. With the extension of the studies above, we analyze the behavior of PFD theoretically. Our early model[11] is based on one-dimensional laminar electron flow, the Antonsen and Ott model.[12] Both the ion-beam current density and the diode impedance predicted by the calculation, however, have been found to deviate from the experimental results. In this paper a new model is developed and presented in detail. The calculated results are compared with the expermental results. From this model, the physical mechanism behind the diode impedance behaviour and the instability of diode operation will be clearly understood. In Section Ⅱ, the diode model and assumptions are presented. Section Ⅲ contains the numerical calculation results along with comparisons between the model and the experimental data obtained at the peak power. Some discussions about the diode behaviour are given in Sec. Ⅳ. We give our concluding remarks in Sec. Ⅴ.

Ⅱ. Model and Assumptions

An appropriate desciption of free electrons in the A-K gap is very crucial in the theories of ion diodes. Early models[12,13] are considered to be not suitable because of the presence of electrons coming from the power feed and the fluctuations in the gap.[14,15] In our new model of PFD presented in this paper, we allow the existence of electrons with velocity in non-z-direction and adopt the flat density profile of electrons from the model of Desjarlais.[15] The constant density distribution not only simplifies the calculation, but also seems to be a good approach to the real situation.[15] In addition, even with the early equilibrium theory,[12] the violation of electron profile from the flat profile in coaxial diode, particularly for smaller radius/gap ratio, is smaller than that in planar diode.

With the flat profile assumption, we write the equations in r direction:

$$d(rE) = e(n_e - n_i)rdr/\varepsilon_0, \qquad (r < r_s) \qquad (1)$$

$$d(rE) = -en_i rdr/\varepsilon_0, \qquad (r > r_s) \qquad (2)$$

$$n_i = \frac{J_a r_a}{e\,r}\left[\frac{m_i}{2e(V_d-\phi)}\right]^{1/2} \qquad (3)$$

where r_s denotes the radius of electron sheath surface, E the electric field, n_e the electron density, n_i the ion density, J_a the ion-current density on anode surface, r_a the radius of anode, m_i the ion mass, V_d the diode voltage between the gap, and ϕ the electric potential. For these equations, we give the following boundary conditions: $\phi(r_c) = 0$, $\phi(r_a) = V_d$, $E(r_c) = 0$, $E(r_a) = 0$ and the continuity of E and ϕ at r_s. Equations (1)-(3) were integrated numerically to give the potential profile in the gap. Among the three parameters of J_a, n_e and r_s, any prescribed one can be used to calculate the other two.

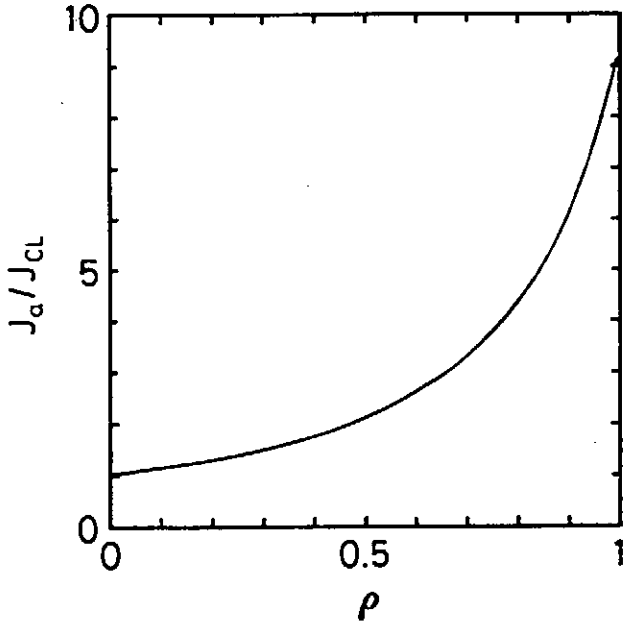

Fig. 3 Calculated result of normalized enhancement ratio, J_a/J_{CL}, as a function of ρ, the ratio of electron-sheath thickness to the A-K gap, $\rho = (r_s-r_c)/(r_a-r_c)$.

Figure 3 shows the calculated result of ion-current density as a function of electron sheath thickness. The ion-current density at the anode surface is normalized by the current density of zero sheath thickness (J_{CL}) so that it represents the enhancement ratio. Here, ρ is the ratio of sheath thickness to the A-K gap. From Fig. 3, we see that, for the fulfilled gap ($\rho = 1$), the enhancement ratio is ~ 9.1.

The magnetic field is determined by assuming that the current I_c exists in the cathode. The equations are:

$$d(rB) = \mu_0 e n_e v_z r dr, \quad (4)$$

$$d(v_z m) = eB dr, \quad (5)$$

where B is the magnetic field, v_z the axial velocity of electron, and m the mass of electron. The boundary conditions are $B(r_c) = \mu_0 I_c/(2\pi r_c)$, and $v_z(r_c) = 0$.

To determine the charge and current distribution in PFD, we assume that the diode is in a steady state. That is, for a given voltage, every parameter can be determined, and does not change with time. Because the electrons are not trapped in the gap, PFD can be more suitably treated by the time-independent model than the other diodes in which the electrons drifts in θ direction.

Another assumption is that the surface of the electron sheath reaches the anode at the downstream end of the diode, i.e., the free electrons always fulfill the A-K gap there. Almost all electrons drifting out of the diode region freely reaches the anode. From the consideration of continuity, the electron-sheath surface should be very close to the anode at the downstream terminal.

In this model, we do not take the electron loss inside the diode into account. We also assume that ions do not pull electrons along with them to the cathode as they pass through the electron sheath. We do not incorporate the A-K gap closure by electrode plasma in our model.

Ⅲ. Numerical Calculation Results

With the above assumptions, the parameter distributions in z

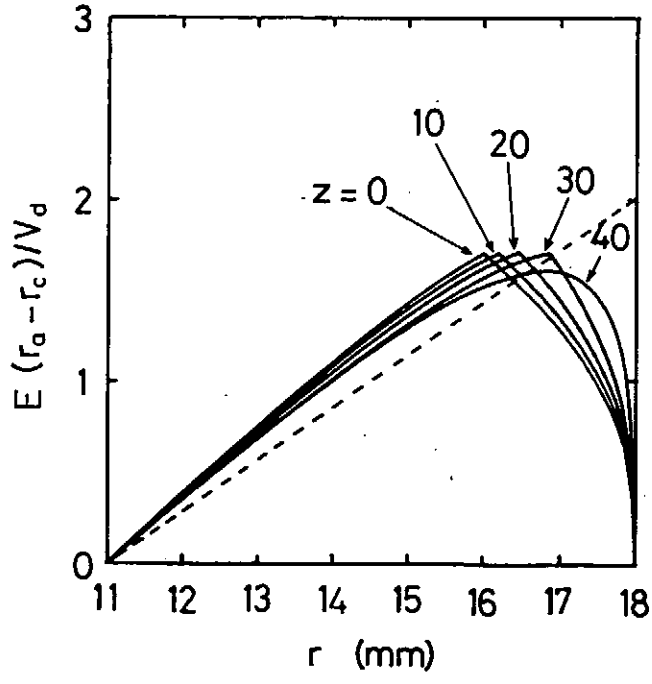

Fig. 4 Calculated result of electric-field distribution for z = 0, 10, 20, 30 and 40 mm, where V_d = 1.5 MV. The dashed line will be used for deriving the scaling law in Sec. Ⅳ.

direction are calculated numerically.

Figure 4 shows the calculated results of electric-field distri- bution with z positions as a parameter. We see from Fig. 4 that the peak electric field is about $1.8V_d/(r_a-r_c)$ and there is no significant variation along z-direction.

Figure 5 shows the calculated results of (a) electron-sheath thickness (r_s) and (b) ion-current density at anode surface (J_a). We see from Fig. 5 (a) that the sheath thickness does not change significantly in the diode. From the following considerations, this is found to be consistant with the assumption that the diode is in a steady state. The axial momentum of electrons at radius r is determined by the total magnetic flux between r and r_c, according to eq. (5). The current that is flowing inside r (including that in the cathode) is limited by the requirement that the axial velocity of electrons does not exceed the absolute velocity determined by electric potential ϕ. In addition, compared to the current in the cathode, the electron current outside the cathode contributes more to ϕ but less to magnetic flux. Therefore, the largest total current (critical current) corresponds to the situation that all the electrons are moving only in z direction and the electron current outside the cathode takes the largest fraction of total current as possible. We incorporate this situation into our model at the upstream end. Otherwise the total current will be smaller than the critical current, and hence the diode is not in a steady state. In other words, the steady state demands that electrons are only emitted at the upstream region. Therefore, in our model, the current carried

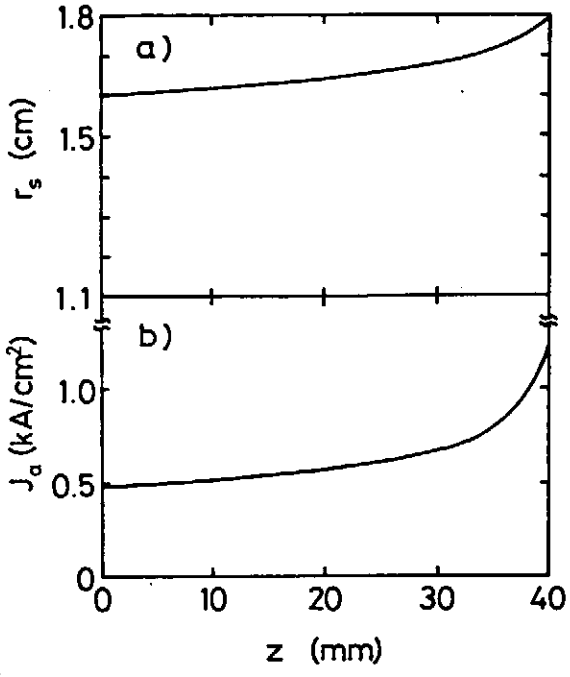

Fig. 5 Calculated result of axial variation of (a) electron-sheath thickness (r_s), and (b) ion-current density at anode surface (J_a).

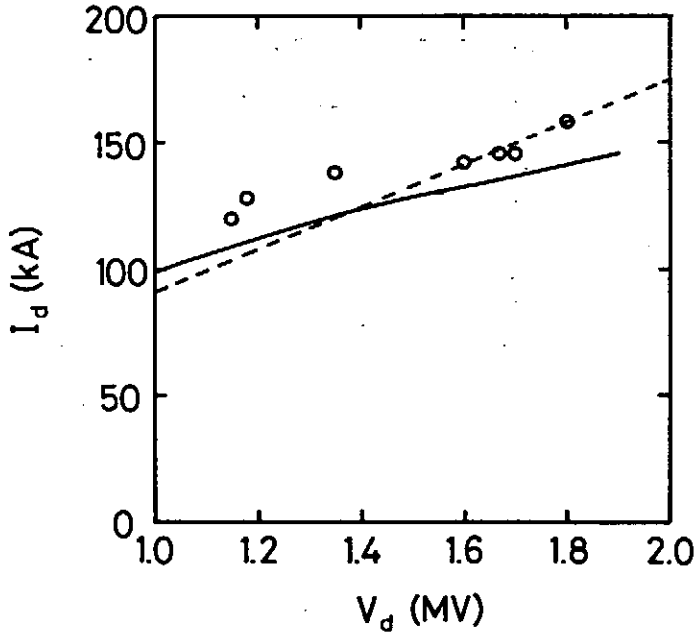

Fig. 6 Calculated result of total diode current (I_d) as a function of diode voltage (V_d), together with the experimental data obtained at peak power of seven shots. Shot No. 1707, 1701, 1704, 1706, 1703, 1606 and 1709 (from left). The dashed line shows the simp lified scaling law which is obtained in Sec. Ⅳ.

by the electron sheath is a constant along z direction. The cathode current is very small at the downstream end and is approximately the total ion current at the upstream end.

The ion-current density in Fig. 5 (b) is compared with previous experimental results. We have experimentally observed the peak ion-current density of 1.4 ~ 1.9 kA/cm^2, which is much larger than that obtained in Fig. 5 (b). However, we note that this peak ion-current density usually appears later than the peak power. The large enhancement at the later stage of the pulse (relative to the peak power) may be caused by the gap closure because of plasma expansion. This is not considered in our model.

The total diode current is calculated for voltages from 1.0 to 1.9 MV, and the results are shown in Fig. 6 together with experimental data obtained at peak power of seven shots. The calculated results are found to be in considerable agreement with the experimental results.

Ⅳ. Analysis of Diode Behaviour

From the above studies, we have figured out the physical picture inside PFD. In this section, we simplify our calculation model into some scaling relations and use them to discuss the

improvement of PFD.

a) Diode impedance

As described in Sec. Ⅲ, the total diode current is determined by the upstream end where the electrons are supposed to move only in z direction. We assume that the relation E = vB approximately hold there, and $v = c(1-\gamma^{-2})^{1/2}$. We assume that the electric field varies linearly in the gap from 0 to $2V_d/(r_a-r_c)$, that is shown as the dashed line in Fig. 4. From Fig. 5 (a), we suppose that the gap is entirely fulfilled by the electrons. Thus, we have:

$$\mu_0 I_t/(2\pi r_a)c(1-\gamma^{-2})^{1/2} = 2V_d/(r_a-r_c), \tag{6}$$

and then

$$I_t \fallingdotseq \frac{4\pi}{\mu_0 c}\,\frac{r_a}{r_a-r_c}\,\frac{V_d}{(1-\gamma^{-2})^{1/2}}, \tag{7}$$

where I_t is the total diode current. Equation (7) is also plotted in Fig. 6 together with the calculated results of our model and the experimental data. Because eq. (7) is derived by our model, it has been found to fit well with the calculated results.

b) Ion-current efficiency

To estimate the relation of total ion current (I_i) and the electron current (I_e), we assume that the electric field varies linearly as the dashed line in Fig. 4 and the electrons fulfill the gap. Considering the relativistic effect, we assume that the electron velocity is propotional to $(r-r_c)^{1/2}$. We also assume the uniformity of ion-current density along z direction. Thus, we have:

$$I_i = 2eN_i/\pi\,(2e/m_i)^{1/2}V_d^{1/2}L/(r_a-r_c), \tag{8}$$

and

$$I_e = 4eN_e/15\;c(1-\gamma^{-2})^{1/2}(3r_a+2r_c)/(r_a+r_c), \tag{9}$$

where N_i and N_e are the total numbers of ion and electron in the gap, respectively. From the assumption that $N_i = N_e$, we get:

$$\frac{I_i}{I_e} = \frac{15}{2\pi c}\left(\frac{2e}{m_i}\right)^{1/2} \frac{V_d^{1/2}}{(1-\gamma^{-2})^{1/2}} \frac{r_a+r_c}{3r_a+2r_c} \frac{L}{r_a-r_c}, \qquad (10)$$

where L is the diode length. Figure 7 shows the ion-current efficiency of eq. (10) (dashed line) and the calculated efficiency of our model (solid line). From Fig. 7, eq. (10) is seen to give a good approximation to our model.

c) Diode operation

The application of eqs. (7) and (10) for changing the diode impedance and efficiency is limited by the instability of PFD. In our model, an idealized assumption is that all electrons are emitted from the cathode at upstream area and arrives at the anode, outside the downstream end as seen from Fig. 1. We suppose that the electron loss in the gap can be neglected. It is necessary for stable diode operation because large electron loss to the anode will bring considerable charge nonuniformity in the A-K gap which causes unusual diode behavior. However, from our theory we understand that, except at the upstream end, the electron total momentum is larger than its z-momentum, that is, the electrons move nonlaminarly. As a result, if the gap length is too small or the axial length of PFD is too long,

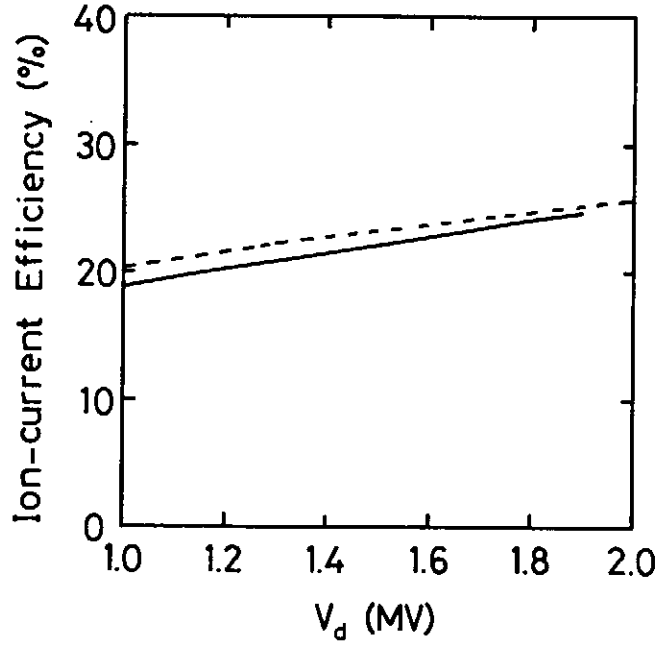

Fig. 7 Ion-current efficiency calculated by the model (solid line) and that of eq. (10) (dashed line).

a large number of electrons are possible to leak to the anode inside the gap, especially at the downstream area.

To avoid such a problem, it is necessary to reduce the non-z-momentum of electrons, that requires the current at every z-position equal to the critical current (cf. eq. (7)). Because the current varies with z, it is necessary to change the geometry of PFD in z-direction. For example, we suggest to use the diode shapes shown in Fig. 8. Figure 8(a) comes from the design of the electron emitter of virtual cathode of applied-B diode.[15] At present stage, we believe that a complete virtual cathode is not practical for PFD because of the large length/radius ratio. In Fig. 8(a), therefore, the cathode is basically a real cathode where only a gap difference is made. Figure 8(b) shows a tapered anode which gives a smooth variation of the gap.

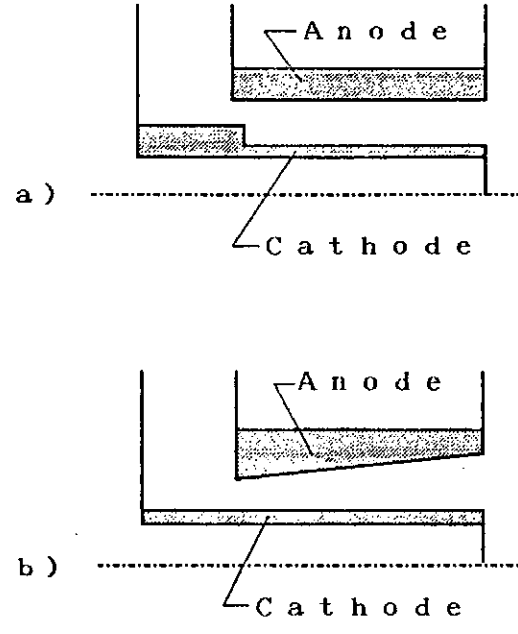

Fig. 8 Improved shapes of PFD by our model.

With eqs. (7) and (10), we can estimate the required gap difference between the upstream end and the downstream end. For example, we take V_d = 1.5 MV, r_a = 17.5 mm and r_c = 12.5 mm (at upstream). We have used the average gap to estimate the total ion current. Then, the calculated results are as follows. For the PFD shape of Fig. 8(a), we evaluate $I_t \sim 180$ kA, $I_i \sim 48$ kA, and $r_c \sim 10.7$ mm (at downstream); for Fig. 8(b), in addition, $I_t \sim 180$ kA, $I_i \sim 45$ kA, $r_a \sim 20.2$ mm (at downstream).

We understand from our model that the experimental problems of operational reproducibility and breakdown are closely correlated to the electron movement in the PFD gap. From the above discussions, we find it is possible to control the electron flow by the geometry of PFD. From eqs. (7) and (10), or the more accurate numerical way of previous sections, it is possible for us to calculate the suita-

ble geometry. After moving the operating point of PFD away from the unstable region, we are possible to adjust the sizes of PFD to change the diode impedance and to increase the ion-current efficiency as indicated by eqs. (7) and (10).

V. Summary and Concluding Remarks

We have presented a new theoretical model for PFD. The model assumes (a) that the electron density profile is constant in r-direction, (b) that the electrons fulfill the A-K gap at the downstream end, and (c) that the anode is a space-charge limited ion source.

The model is supported by the experimental data of diode impedance obtained at the peak power. The major conclusions of our theory are as follows:

1) For stable diode operation, the steady-state charge and current distributions demands constant electron current in z-direction, so that there is no large parameter variation in the axial direction of PFD.

2) From the smooth parameter distribution in PFD described by our model, we have derived the simplified scaling relations of the diode impedance and ion-current efficiency.

3) Our theory shows that, by adjusting the geometry of PFD, it is possible to optimize the diode parameter without bring instability in the diode operation.

Acknowledgments

This work was partly supported by a Grant-in-Aid from the Ministry of Education, Science and Culture of Japan. Calculational cooperations given by H. Sugimura of Laboratory of Beam Technology are acknowledged with thanks.

References

1. S. Humphries, Jr.: Nuclear Fusion 20, 1549 (1980).
2. K. Yatsui: Laser and Particle Beams 7, 733 (1989).
3. K. Masugata, T. Yoshikawa, A. Takahashi, K. Aga, Y. Araki, M. Ito and K. Yatsui: Proc. 6th Int'l. Conf. on High-Power Particle Beams (ed. by C. Yamanaka), p. 152 (1986).
4. K. Masugata, K. Aga, A. Takahashi and K. Yatsui: Proc. 2nd Int'l. Top. Symp. on ICF Res. by High-Power Particle Beams, Nagaoka, (ed. by K. Yatsui), p. 81 (1986).
5. K. Yatsui, Y. Shimotori, Y. Araki, K. Masugata, S. Kawata and M. Murayama: Proc. 11th Int'l. Conf. on Plasma Phys. & Controlled Nucl. Fusion Res., Kyoto, IAEA-CN-47/B-Ⅲ-9 (1986).
6. K. Yatsui, K. Masugata and S. Kawata: Laser Interaction and Related Plasma Phenomena (Plenum Press, New York & London), 8, p. 653 (1988).
7. K. Yatsui, Y. Shimotori, H. Isobe, W. Jiang and K. Masugata: Proc. 12th Int'l. Conf. on Plasma Phys. & Controlled Nucl. Fusion Res., Nice, IAEA-CN-50/B-4-2 (1988).
8. K. Yatsui, K. Masugata, Y. Shimotori, K. Imanari, M. Murayama, M. Yokoyama and T. Takaai: Proc. 7th Int'l. Conf. on High-Power Particle Beams (ed. by W. Bauer and W. Schmidt), Vol. I, p. 522 (1988).
9. K. Masugata, H. Isobe, K. Aga, M. Matsumoto, S. Kawata, W. Jiang and K. Yatsui: Laser and Particle Beams 7, 287 (1989).
10. W. Jiang, C. Zhang, K. Masugata and K. Yatsui: Jpn. J. Appl. Phys. 29, 434 (1990).
11. W. Jiang, K. Masugata and K. Yatsui: Research Report of Lab. of Beam Tech., LBT-8901, (Nagaoka Univ. Tech.) (1989).
12. T. M. Antonsen, Jr. and E. Ott: Phys. Fluids, 19, 52 (1976).
13. K. D. Bergeron: Phys. Fluids, 20, 688 (1977).
14. P. A. Miller and C. Mendel, Jr.: J. Appl. Phys., 61, 529 (1987).
15. M. P. Desjarlais: Phys. Fluids, B1, 1709 (1989).

Pulse-Power Characteristic of "VIVA-I", Versatile Inductive Voltage Adder

K. Shimiya, Y. Hozumi, T. Aoyama, M. Shigeta+, K.Shibata+,
Y. Sekimoto, K. Masugata, and K. Yatsui
Laboratory of Beam Technology, Nagaoka University of Technology,
Nagaoka, Niigata 940-21
+Permanent address: Ferrite Division, TDK Electronics Co. Ltd.,
Narita, Chiba 286

Abstract

Versatile Inductive Voltage Adder, "VIVA-I", with high potential gradient has been successfully developed to be in operation. It has been designed to produce output pulse of 4 MV, 60 ns by adding 2 MV pulses in 2-stages of induction cells, where amorphous cores are installed. Within ~ 40 % of full charge voltage, pulse-power characteristics of Marx generator, pulse forming line (PFL), transmission line (TL), and induction cells were tested for three types of loads; open-circuit, dummy-load of $CuSO_4$ resistor, and electron diode. In open-circuit test, ~ 2.0 MV of output voltage was obtained with good reproducibility. Dependence of output voltage on diode impedance was evaluated by using a dummy-load, and good agreement was obtained with that expected. An E-beam diode was operated successfully, and ~ 18 kA of beam current was obtained at diode voltage of ~ 1 MV.

§ 1. Introduction

Inductive voltage adder is a promising technology to obtain a high-power pulse of voltage more than 10 MV. Using an amorphous metallic material as magnetic cores, we expect a high potential

gradient of more than 2 MV/m,[1-3] due to its high saturation level of flux density as well as its high frequency response.[4]

To demonstrate such a technology to be realistic, we have constructed "VIVA-I", a compact, highly potential-gradient pulse-power machine, the details of which will be described in this paper.

§ 2. Description of "VIVA-I"

"VIVA-I" consisits of a Marx generator, a Blumlein PFL, a pulse distributer, four TLs, two induction cells, and a diode. The primary energy storage of "VIVA-I" is Marx generator of 17-stages. Stored energy of Marx generator is 43 kJ at charging vortage of ± 75 kV, which yields 2.55 MV of output voltage.

Both PFL and pulse distributer are located in deionized water. The cross-sectional view of this section is shown in Fig. 1. The PFL used is cylindrical Blumlein line (BL) with switching reversed. Intermediate conductor (IMC) of BL is directly charged by Marx generator in ~ 500 ns. BL switch is self-breakdown SF_6-gas switch located between IMC and outer conductor. Design parameters of BL output are written as follows: Z_{BL} (output impedance) ~ 12.5 Ω, τ_{BL} (pulse width) ~ 60 ns, $V_{BL(max)}$ (output voltage) ~ - 2 MV.

The output pulse of BL is fed to pulse distributer through a four-channel pre-pulse switch (water, self-breakdown), and divided to four 50-Ω pulses. They are transported to inductive voltage adder section through oil filled, four coaxial TLs.

Figure 2 shows the cross-sectional view of the adding section, which consists of two induction cells and a diode. The outer diameter and length of one cell are ~ 1 m and ~ 0.8 m, respectively. Two 50-Ω TLs are connected to one cell in parallel. Average potential gradient of ~ 2.5 MV/m is achieved by the application of 2 MV. Amorphous cores are immersed in oil and the oil-vacuum interface is made of acrylic insulator. Properties of amorphous metallic cores installed inside the cells are presented in Table I.

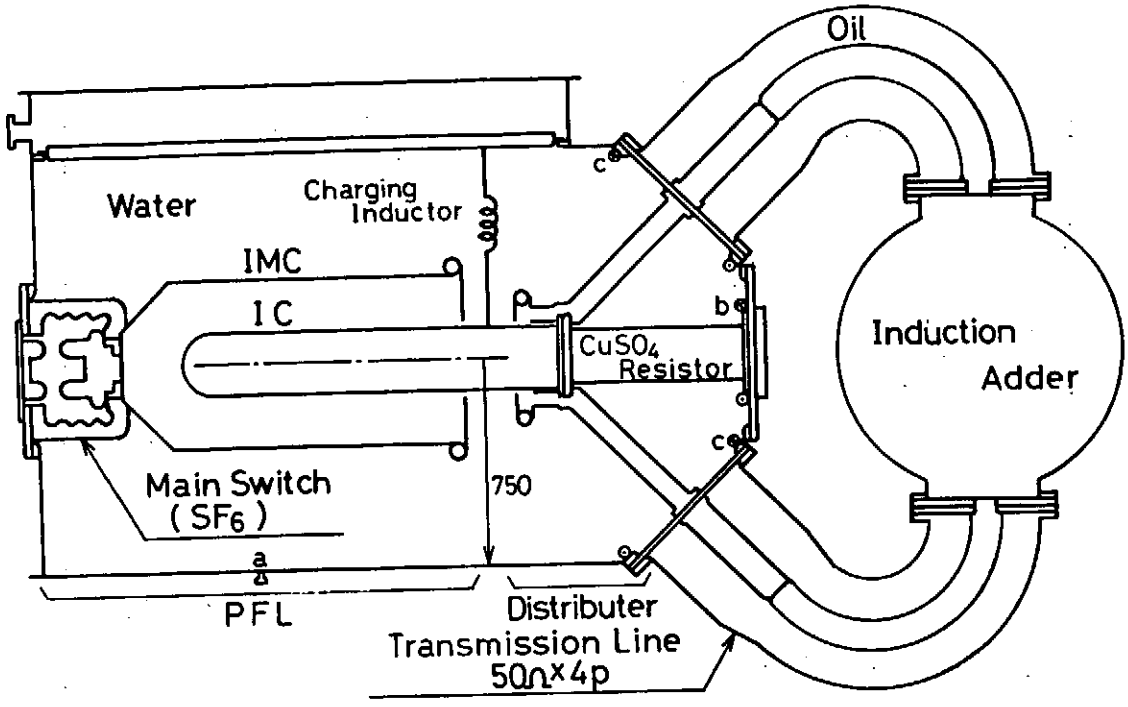

Fig. 1 Cross-sectional view of PFL, distributer, and TLs.

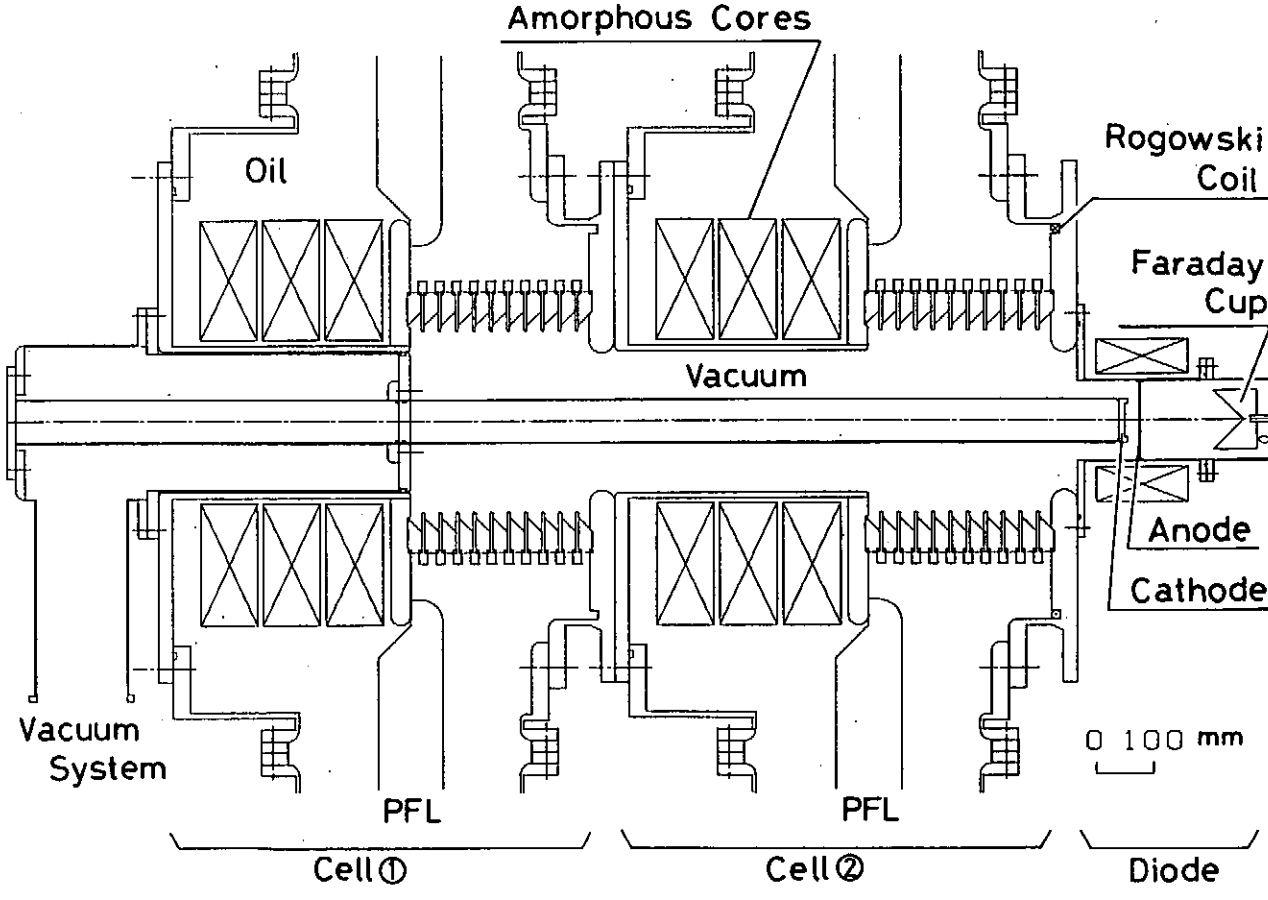

Fig. 2 Cross-sectional view of induction cells and diode.

Table I. Size and properties of amorphous core (1 core)

Size			
Outer diameter	700	mm	
Inner diameter	300	mm	
Width	96	mm	
Insulater	6	μm	(PET)
Filling factor	~ 70	%	
Magnetic properties of core (DC Value)			
B_s (Saturation flux density)	≧ 1.0	T	
B_r (Residual flux density)	≧ 0.75	T	
ΔB (Flux swing)	~ 1.75	T	
H_c (Coersive force)	≦ 4.0	A/m	
$V \cdot \tau$	~ 0.034	Vs	
Amorphous metallic tape			
Thickness	~ 21	μm	
Resistivity	~ 130	$\mu\Omega \cdot$cm	

The output voltage from two induction cells are added in series by a center conductor/MITL. Such the pulse added is finally deliverd to the diode. In the initial test of the system, we have installed a resistor of $CuSO_4$ solution or E-beam diode (shown in Fig. 2).

Figure 3 presents the eqivalent circuit of the whole system of "VIVA-I". Some diagnostics in the initial test are also indicated.

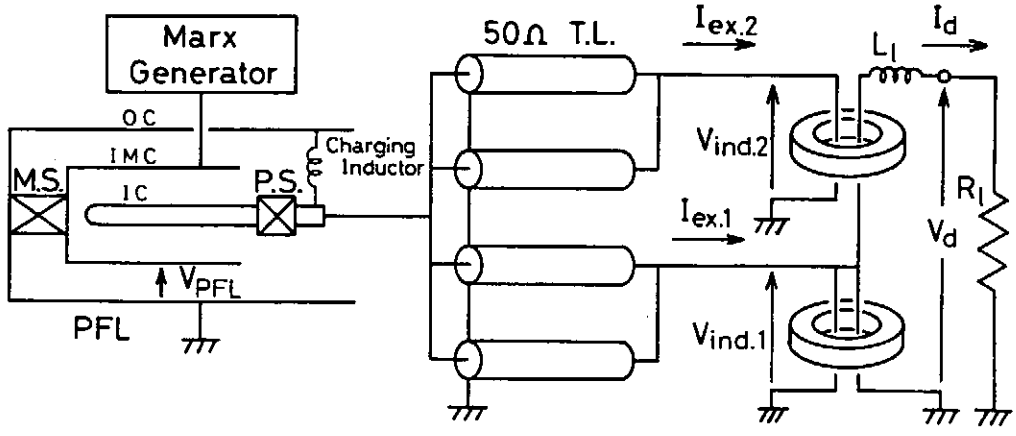

Fig. 3 Equivalent circuit of whole system of "VIVA-I".

§ 3. Results of Initial Tests

Initial tests of the whole system were carried out at V_{ch} (charging voltage of Marx generator) ≦ 30 kV, which is less than 40 % of full charge voltage. To obtain characteristics of magnetic cores in saturated level within the limited V_{ch}, we have first installed two cores to each cell. As a result, the value of $V\tau$ of one cell is reduced to ~ 0.067 Vs from the initially designed value of ~ 0.1 Vs.

3.1. Open-circuit Test

Open-circuit test was carried out by taking out the center feeder/MITL of the adder. Figure 4 shows typical waveforms at V_{ch} = 30 kV. As seen From Fig. 4 (a), charging voltage of PFL reaches 1.1 MV at t ~ 600 ns and then BL switch is closed. From Fig. 4 (b) of applied voltage of cell ① (V_{ind}), pre-pulse voltage of ~ 100 kV is seen to be present for ~ 600 ns, and after that negative main pulse of V_{ind} ~ 1.0 MV is obtained with pulse width of ~ 75 ns. Due to the presence of pre-pulse, cores are automatically biased, and good reproducibility was obtained even in the absence of reset pulse. Figure 4 (c) shows the excitation current of cell ① (I_{ex}). We see I_{ex} builds up at t ~ 610 ns, and gradually increases, and reaches ~ 8 kA at the peak of V_{ind} (t ~ 700 ns). After t ~ 780 ns, I_{ex} significacantly increases, and reaches the peak value of 25 kA at t ~ 850 ns, indicating the saturation of magnetic cores at t ~ 780 ns.

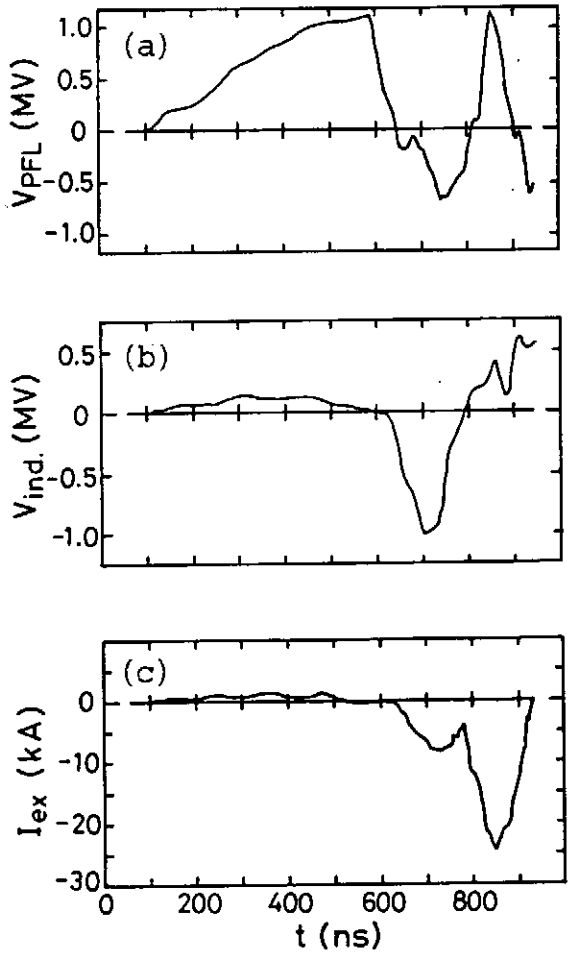

Fig. 4 Typical waveforms of open-circuit test. (a) V_{PFL}, (b) V_{ind} and (c) I_{ex}.

Integral of V_{ind} from t ~ 610 ns to ~ 780 ns is calculated to be ~ 0.065 Vs, which reasonably agrees to the value of $V\tau$ of the cells (~ 0.067 Vs) stated previously.

Figure 5 shows the dependence of V_{PFL}, V_{ind}, and I_{ex} on V_{ch}. We see that both V_{PFL} and V_{ind} increase almost propotionally to V_{ch}. Such the linear increase in V_{ind} on V_{ch} suggests that magnetic core is not saturated before the peak of V_{ind}.

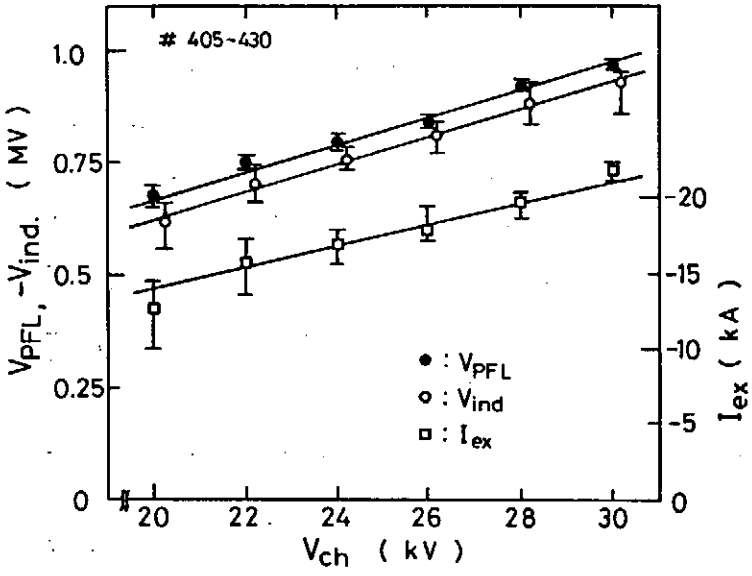

Fig. 5 Dependence of V_{PFL}, V_{ind} and I_{ex} on V_{ch}.

3.2 Dummy-load Test

Pulse-power characteristics were measured by using a resistance of $CuSO_4$ solution as a dummy load. Three kinds of resistances (R_l = 50, 120, and 580 Ω) were used in this test.

Figure 6 shows V_d (peak diode voltage applied to the load) and V_{ind} vs. V_{ch}. We see V_d and V_{ind} are propotional to V_{ch}. The difference between V_d and V_{ind}, which is due to the inductive voltage drop in the center conductor ($L_l (dI_d/dt)$), increases with decresing R_l. We have calculated L_l from the dimension of the center conductor to be ~ 450 nH, which almost agrees with that estimated from these experimental results by using the relation,

$$V_d \ (= R_l I_d) = (V_{ind.1} + V_{ind.2}) - L_l (dI_d/dt) \ . \qquad (1)$$

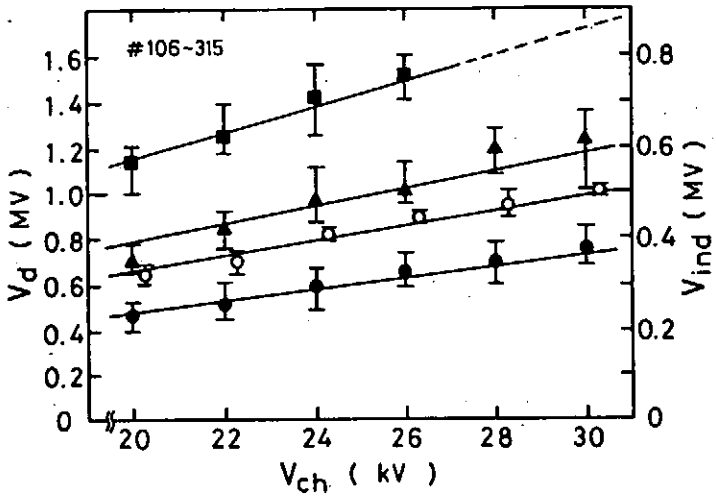

Fig. 6 Dependence of V_d and V_{ind} on V_{ch}.
● : V_d at R_l = 50 Ω,
▲ : V_d at R_l = 120 Ω,
■ : V_d at R_l = 580 Ω,
○ : V_{ind} at R_l = 50 Ω.

3.3 Electron-Beam Production

As shown in Fig. 7, E-beam generation experiment was carried out by using an annular diode (cathode; carbon, anode; Ti foil of thickness ~ 20 μm). The inner and outer diameters of the cathode are ID = 58 mm and OD = 76 mm, respectively, and the gap length d_{K-A} = 17 mm. Axial magnetic field of B_z ~ 0.84 T is applied to the diode and a drift region. The E-beam current is measured by a Faraday cup at ~ 160 mm downstream from the anode.

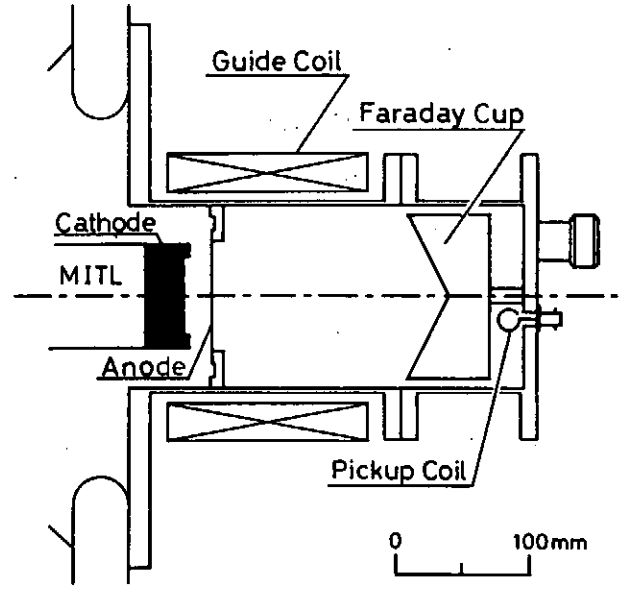

Fig. 7 Cross sectional view of E-beam diode.

Figure 8 shows these typical waveforms. Clearly, E-beam is generated with V_d ~ 1 MV (estimated from V_{ind} and I_d by using eq. (1)), I_d ~ 20 kA, and I_b (beam current) ~ 18 kA.

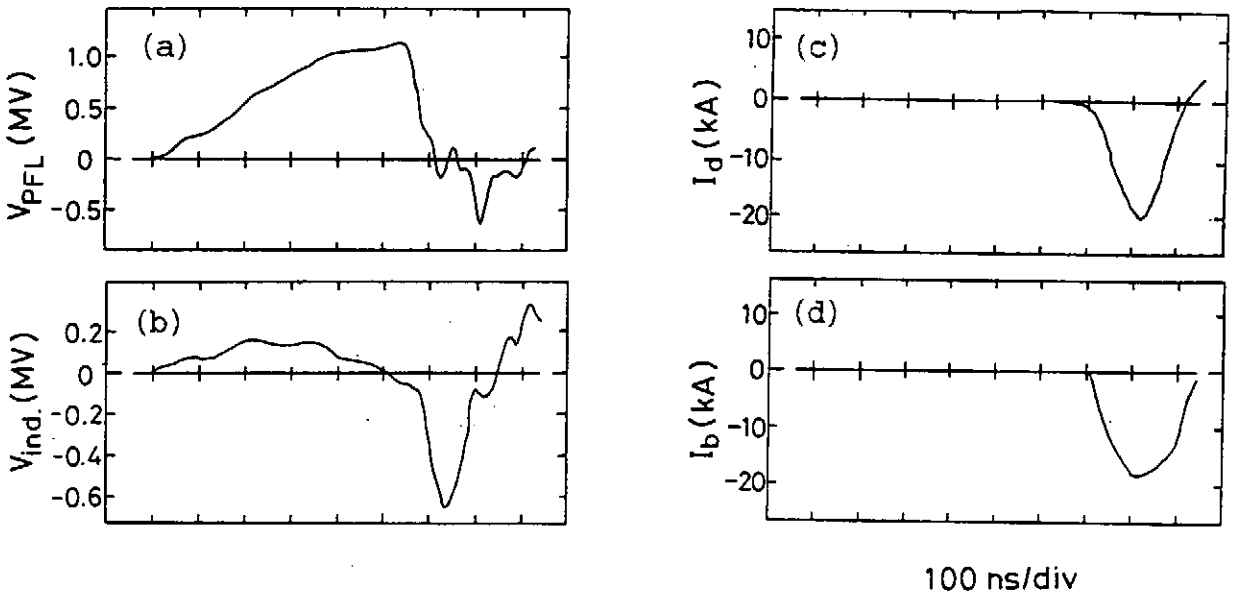

Fig. 8 Typical waveforms of E-beam production experiment.

§ 4. Concluding Remarks

"VIVA-I" was successfully constructed to be in operation, of which initial operating tests were carried out less than 40 % of full charge voltage. In the open-circuit test, ~ 2.0 MV of output voltage is obtained with good reproducibility. Dependence of output voltage on diode impedance was evaluated by using dummy load, and good agreement was obtained with that expected. An E-beam diode was successfully operated to produce ~ 18 kA of beam current.

The experiment is continued to increase the output voltage, optimize the parameters of each part, and improve the accuracy of diagnostics. Ion-beam diode experiment is also planned to be carried out soon.

Acknowledgement

This work was partly surported by a Grant-in Aid for Scientific Research from the Ministry of Education, Science and Culture of Japan.

References

1) J. P. Corley, C. E. Heath, D. L. Johnson, S. E. Rosenthal, J. W. Poukey, W. G. Adams and J. J. Ramirez: Proc. 6th IEEE Pulsed Power Conf., Arlington, VA, Ⅶ A, 571 (1987).
2) J. J. Ramirez, K. R. Prestwich, J. A. Alexander, J. P. Corley, G. J. Denison, C. W. Huddle, D. L. Jhnson, R. C. Pate, G. J. Weber, E. L. Burgess, R. A. Hamil, J. W. Poukey, T. W. L. Sanford, L. O. Seamons and G. A. Zawadzkas: Proc. 7th Int'l Conf. High-Power Particle Beams, Karlsruhe, West Germany, I, 148 (1988).
3) I. Smith, P. Corcoran, H. Nishimoto and D. Wake: ibid. I, 127 (1988).
4) T. Aoyama, Y. Hozumi, K. Shimiya, M. Shigeta, K. Shibata, K. Masugata and K. Yatsui: Proc. Symp. Production and Target Interaction of Particle Beam, IPPJ-900, Inst. Plasma Phys., Nagoya, 100 (1989).

REDUCTION OF LOW ENERGY COMPONENTS IN PULSE ION BEAM

M. Sato, Y. Hashimoto, M. Yatsuzuka and S. Nobuhara

Department of Electrical Engineering, Faculty of Engineering,
Himeji Institute of Technology, Shosha, Himeji, Hyogo 671-22, Japan

Abstract

We tried reduction of low energy components in pulse ion beams with self-crowbar switch of which operation was achieved by expansion of electrode plasmas in a small MITL. The experiments were carried out with the small MITL (self-crowbar switch) and the "Inverse Pinch Ion Diode". From the experimental results, the times required for dropping of pulse high voltage were shortened from 40 to 15 ns. As the result of this shortening, the ions accelerated at a relatively low voltage decreased, and the energy ranges of proton beams were reduced from 60 to 30 keV.

§1. Introduction

In an experiment with a pulse power generator, a diode voltage is generally dropped slowly by the effect of the inductance between the end of the generator and a diode. That is, a diode current is held after ending of a pulse high voltage by inductively stored energy. The differential coefficient of this diode current and the impedance generate a voltage. This voltage corresponds to the tail of the diode voltage, and is caused by slow dropping of it. In this tail, ions are also accelerated. However the energies of these ions are considerably lower than that of the ions which are accelerated at the top of the diode voltage. These low energy ions broaden the energy ranges of the ion beams. The broad energy ranges are not desirable in utilization to development of new materials, e.g. modification of surface layer.

From the previous experimental results[1], transport of pulse power is limited by expansion of electrode plasmas in a small magnetically insulated transmission line (MITL). That is, expansion of a cathode and an anode plasma shorts the gap between the inner conductor (cathode) and the outer conductor (anode) of the small MITL. On the other hand, it is expected

that this shorting of the gap is utilized as self-crowbar switch operation.

Figures 1 (a) and (b) show the schematic drawings of the small MITL and a small relativistic electron beam diode reported in ref. 1. Initially the small MITL operates as a diode, and an electron current I_{MITL} flows across the gap of the MITL. When a diode current I_D exceeds a critical current (e.g. the current calculated by the para-potential flow model[2]), I_{MITL} decreases by magnetic insulation. However initially produced plasmas on the conductors expand with the velocity of $2 \sim 7 \times 10^6$ cm/s [3] (Fig. 1 (a)), and the gap between the conductors is closed by several tens of nano-seconds (Fig. 1 (b)). In this time, it is expected that the diode voltage drops sharply if a crowbar current I_{CR} decreases sharply. In order to sharp decreasing of I_{CR}, it is required that the impedance of the diode is high and the inductance from the small MITL to the diode is low.

In this paper we present initial experimental results on reduction of low energy components in pulse ion beam by self-crowbar switch operation.

§2. Experimental Setup

The schematic drawings of the "Inverse Pinch Ion Diode" (IPD) [4] and the experimental setup are shown in Figs. 2 (a) and (b), respectively. The small MITL, which plays a role of a self-crowbar switch, consists of a metal rod (inner conductor) and the inner surface of an aperture drilled on the metal plate (outer conductor). In Fig. 2 (a), a brass rod which held the cathode of IPD was used as the inner conductor. The inner surface of the aperture located at the center of the ring anode of IPD was also used as the outer conductor. A gap length between these two conductors Δ was varied 1 to 4 mm in order to change a time required for turning on the switch.

The "Inverse Pinch Ion Diode" was used as the load of the self-crowbar switch. This diode consists of a ring cathode projected from a circular plate and a ring anode. When a pulse high voltage is applied to the diode, the electrons emitted from the ring cathode are accelerated to the anode, and bombard the anode surface. On this anode surface, the ring made of a 2 mm thick acrylic plate was attached. This ring is bombarded by the electrons, and its surface layer becomes a plasma which plays a role of an ion source. At the same time, the current flowing along the center conductor generates the azimuthal magnetic field. This magnetic field makes the electrons move radially, so that the lifetime of the electron is

lengthened. Consequently, effective ion beam generation is expected.

The pulse power generator "HARIMA-II" (400 kV, 3 Ω, 50 ns) was used in the experiments reported here. Figure 2 (a) shows the experimental setup arranged at the end of the "HARIMA-II". Voltages were measured at the end of the "HARIMA-II" (V_L) and at the diode (V_D). A copper sulfate and a resistive voltage divider were used for measurement of V_L and V_D, respectively. A diode current (I_D) was measured with a Rogowski coil. A biased ion collector (BIC) was used to measure the total current of the ion beam (I_i). An grounded plate, which has many small apertures, is set in front of BIC. The diameter of the aperture and the distance of separation between the apertures are 0.5 and 10 mm, respectively. From these values, the transparency of the grounded plate is 0.2 %. A charge collector in the BIC was biased at -450 V to remove the accompanying electrons. A Thomson-parabola ion spectrometer was employed for analyzing the species and those energies of ion beams, and consisted of a collimator, an electric and a magnetic deflection section, and a film holder. The collimator has the two pinholes of which diameters are 0.2 and 0.5 mm. The maximum values of the magnetic and the electric field are 0.54 T and 6 kV/cm, respectively. The film CR-39 was used for detection of analyzed ions.

§3. Experimental Results

3.1 Change in Wave-Form of Diode Voltage

The wave-forms of the diode voltage with operation and without operation of the self-crowbar switch are shown in Figs. 3 (a) and (b), respectively. The both shots were fired under the condition of 40 % of the maximum output voltage and the anode-cathode gap length δ of 3 mm. In the case of Fig. 3 (a), the gap length between conductors of the small MITL Δ was set by 1.5 mm. This short gap length permits the electrode plasmas to close the gap during the duration of the diode voltage; the small MITL operates as a self-crowbar switch. As a result of switch operation, the diode voltage drops sharply at the end of it (by about 15 ns). In the case of Fig. 3 (b), Δ was set by 3 mm, and the small MITL does not operate as the self-crowbar switch. In this case, the diode voltage drops by about 40 ns. The difference between these two values mean that the time required for dropping of the diode voltage is able to be shortened considerably by switch operation.

3.2 Energy Analysis of Ion Beams

The species and the energies of the ions were analyzed with the Thomson-parabola ion spectrometer. The traces on the film CR-39 are shown in Figs. 4 (a) and (b). Spot like traces are found at the intersections of the vertical and the horizontal lines. These correspond to the traces by neutral particles, and correspond to the origins of the coordinate in the Thomson-parabola ion spectrometer. The experiments to obtain these traces were carried out under the condition of 60 % of the maximum output voltage and the anode-cathode gap length of 3 mm. The gap lengths Δ of 1.5 and 3 mm were employed in the shots of Figs. 4 (a) and (b), respectively. In the case of Fig. 4 (a), only aclyric plate was used for the ion source, but Aquadac was painted on the aclyric plate in the case of Fig. 4 (b). Therefore the carbon ions are detected in Fig. 4 (b).

With switch operation (Fig. 4(a)), the maximum and the minimum energy of the proton beams are 130 and 100 keV, respectively. The difference between these two values is 30 keV. Without switch operation (Fig. 4 (b)), the low energy ions increased. The maximum and the minimum energy of the proton beams are 140 and 80 keV, respectively. The difference between these two values is 60 keV. From these values, the energy range of the proton beams is reduced to half with switch operation.

3.3 Voltage Amplification by Magnetic Insulation

Figures 5 (a), (b), (c) and (d) show the wave-forms of the voltages measured at the end of the "HARIMA-II" V_L, the diode voltages V_D, the diode currents I_D and the total currents of the ion beam I_i, respectively. In Figs. 5, data obtained by two shots are displayed. These two shots were fired under the condition of 60 % of the maximum output voltage and the anode-cathode gap length of 4 mm. With switch operation (four figures at left hand), the gap lengths Δ was set as 1.5 mm. Without switch operation (four figures at right hand), the gap lengths Δ was set as 3 mm.

In Fig. 5 (a), the maximum voltage in each shot is about 300 kV, and similar wave-forms are obtained with and without switch operation. In contrast to the case of V_L, the wave-forms of V_D are quite different. Without switch operation, the diode voltage reaches to a peak value of 170 kV by 15 ns, and drops sharply. After that, the voltage returns to 170 kV, and drops slowly. The ions are accelerated by the voltage under 120 kV, and its acceleration period is very long. With switch operation, the

voltage at the initial peak is a lower value of 120 kV, and returns to a higher value of 190 kV. After that, the voltage drops sharply. The ions are accelerated by the voltage under 190 kV, and its acceleration period is very short.

Here we compare the maximum values of the diode voltage which contribute to ion acceleration. In Fig. 5 (b), this value increases from 120 to 190 kV with switch operation. The value also increases from 100 to 140 kV in Fig. 3. From these values, the maximum value of the diode voltage which contributes to ion acceleration increases by about 50 % with switch operation. The reason why the diode voltage is increased is not made clear, but we consider that the phenomenon like as the plasma erosion opening switch[5] occurs. That is, the current flowing across the small MITL is switched over to the diode by magnetic insulation. In other words, voltage amplification by magnetic insulation occurs.

Without switch operation, the diode current linearly increases up to the maximum value of 80 kA in Fig. 5 (c). With switch operation, the diode current linearly increases up to about 40 kA. From this time, the rate of increase in I_D changes, and reaches to the maximum value of 110 kA. This change is caused by shorting of the gap in the self-crowbar switch.

In Fig. 5 (d), the pulse width of I_i is short with switch operation, and is long without switch operation. The difference in these two waveforms of I_i suggest that low energy ions are decreased by sharp dropping of the diode voltage. In other words, the energy range of ion beams becomes narrow.

§4. Summary

We tried reduction of low energy components in the pulse ion beams with the self-crowbar switch of which operation was achieved by expansion of the electrode plasmas in the small MITL. The experiments were carried out with the small MITL (self-crowbar switch) and the "Inverse Pinch Ion Diode". The major results are followings;

1. With switch operation, the times required for dropping of the pulse high voltages were shortened from 40 to 15 ns.
2. The ions accelerated at a relatively low voltage decreased, and the energy ranges of proton beams were reduced from 60 to 30 keV.
3. The maximum value of the diode voltage which contributes to ion acceleration increased by about 50 % with self-crowbar switch

operation.

References

1) M. Sato, J. Mizui, H. Yonezu and T. Tazima: Jpn. J. Appl. Phys. 25 (1986) 601.

2) J. M. Creedon: J. Appl. Phys. 48 (1977) 1070.

3) R. K. Parker, R. E. Anderson and C. V. Duncan: J. Appl. Phys. 45 (1988) 2463.

4) For example:
S. Miyamoto, A. Yoshinouchi, T. Ozaki, S. Higaki, H. Fujita, K. Imasaki, S. Nakai and C. Yamanaka: Jpn. J. Appl. Phys. 22 (1983) L703.

5) For example:
R. A. Meger, R. J. Commisso, G. Cooperstein and S. A. Goldstein: Appl. Phys. Lett. 42 (1983) 943.

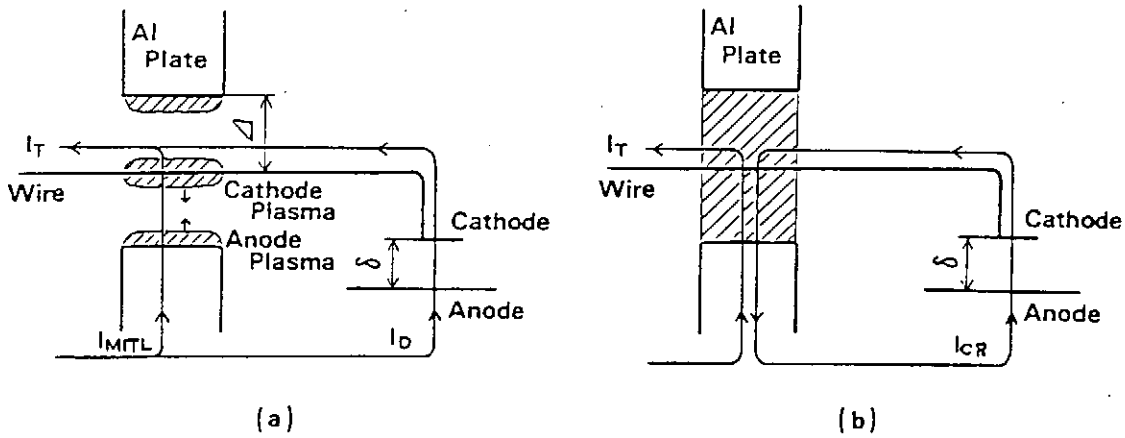

Fig. 1. Schematic drawings of the small MITL and a diode: (a) plasma expansion and (b) after self-crowbar.

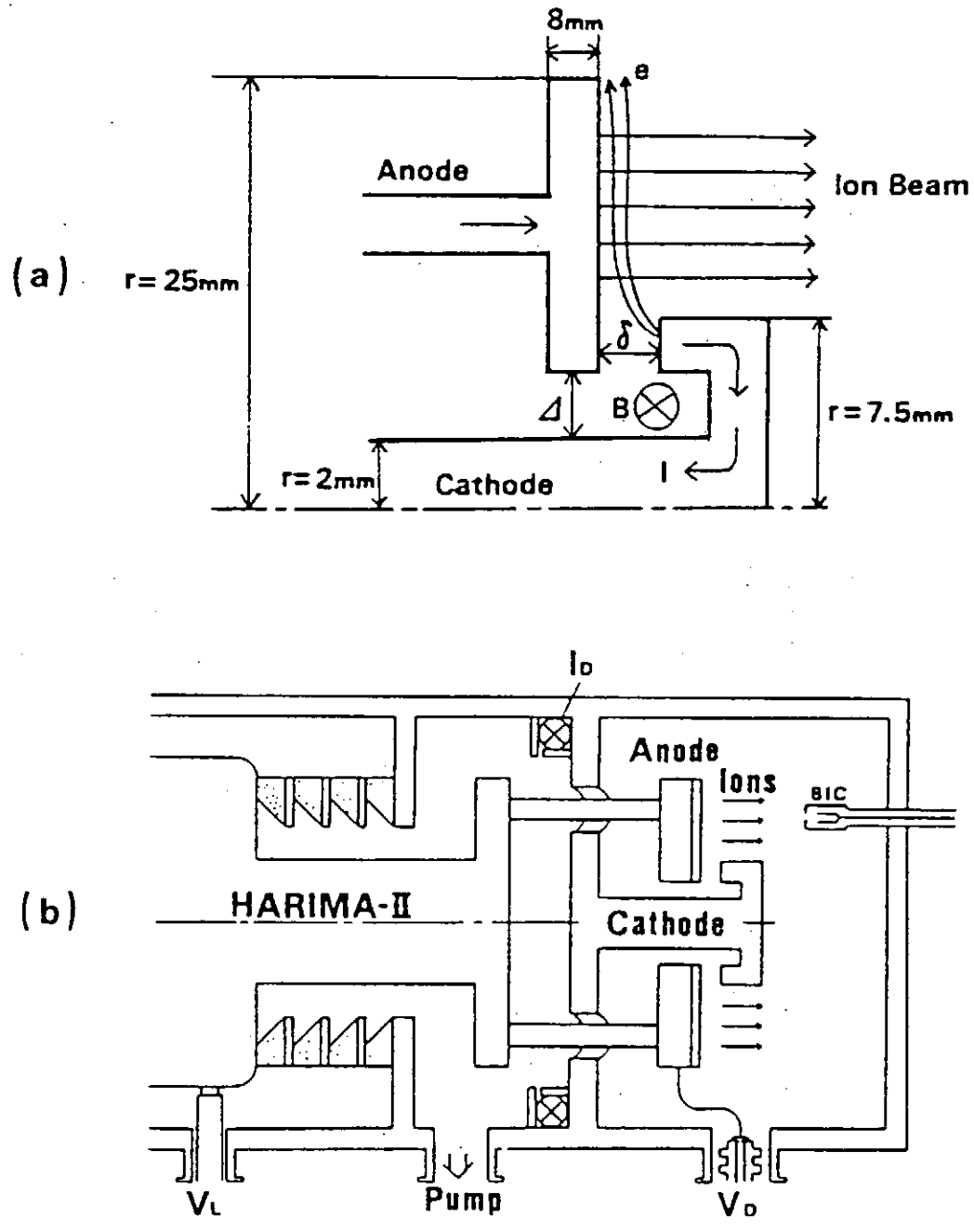

Fig. 2. Schematic drawings of (a) the "Inverse Pinch Ion Diode" and (b) the experimental setup.

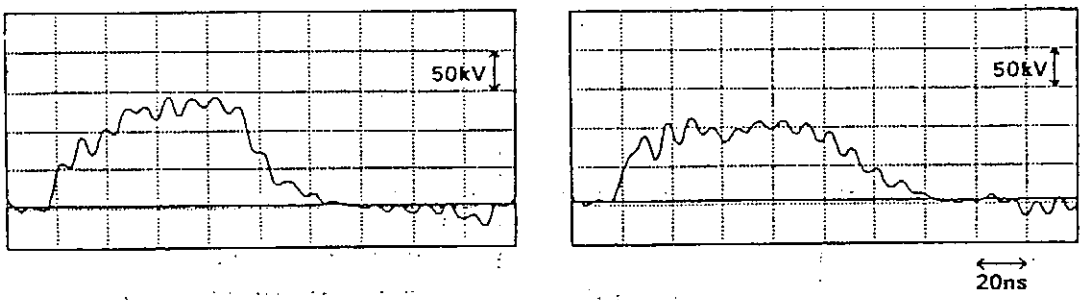

Fig. 3. The wave-forms of the diode voltage.

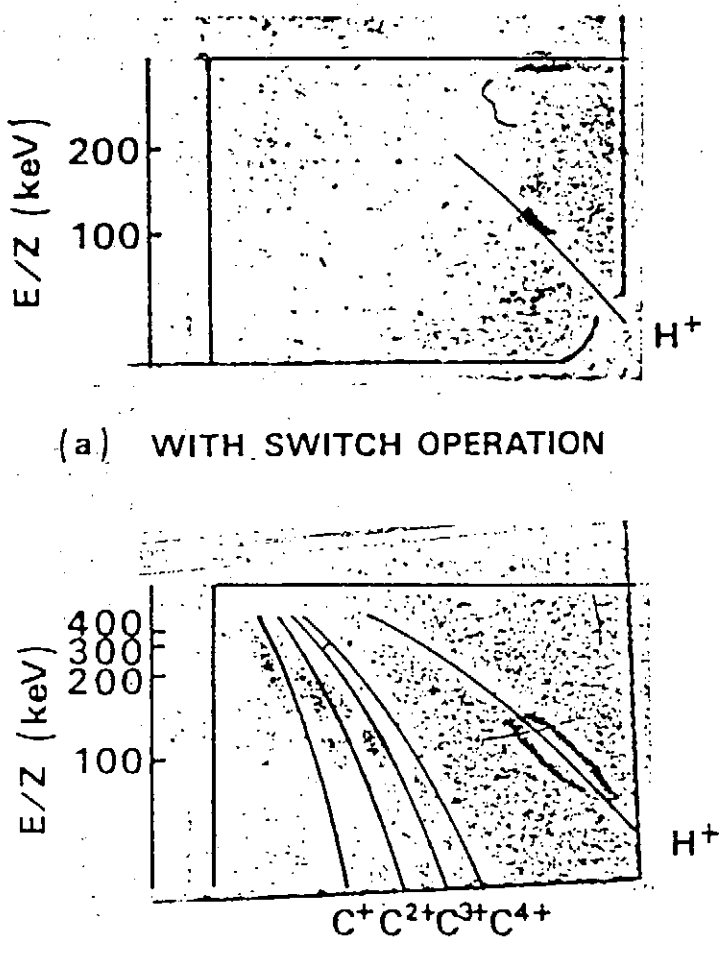

Fig. 4. Traces on the film CR-39 located in the Thomson-parabola ion spectrometer with the magnetic field of 0.1 T and the electric field of 3 kV/cm.

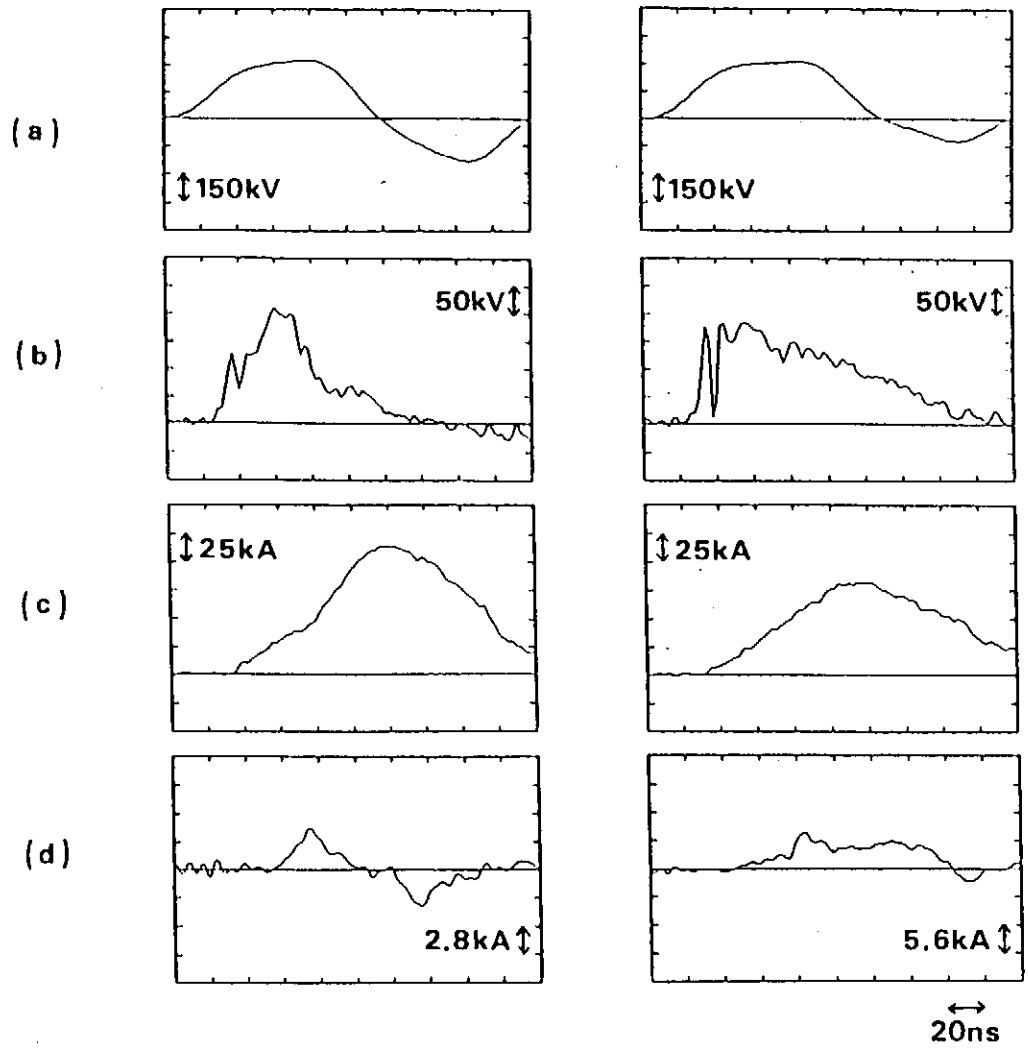

Fig.5. The wave-forms of (a) V_L, (b) V_D, (c) I_D and (d) I_i. The figures placed at the left hand were obtained with switch operation, and the other figures were obtained without switch operation.

GENERATION AND FOCUSING OF CARBON ION BEAM BY THE "INVERSE PINCH ION DIODE"

Y.Hashimoto, M.Sato, M.Yatsuzuka and S.Nobuhara

Department of Electrical Engineering, Faculty of Engineering,
Himeji Institute of Technology, Shosha, Himeji, Hyogo 671-22, Japan

Abstract. Focusing of intense ion beams has been attained with the "Inverse Pinch Ion Diode" which has a flat anode. The energy of the ion beam was 180 keV. At the focal point, the ion current density of 0.5 kA/cm^2 has been obtained and the focusing radius of the ion beam (FWHM) is 10 mm. Focusing of the ion beam is due to the electrostatic field in the "Inverse Pinch Ion Diode".

1. Introduction

In recent years, intense ion beams generated with the pulse power generator have been studied an energy driver for inertial confinement fusion (ICF)[1]. The intense ion beams have been also utilized to development of new materials, e.g. surface modification, annealing and preparation of thin films[2-4].

For applications of the ion beams as a heat source, focusing of intense ion beams is one of desirable characteristics. In order to focus ion beams, the magnetic lens or the diode having a curved electrode are generally used. These methods need a power source of the magnetic coils or the anode of a concave surface. A simple method to focus ion beams using the "Inverse Pinch Ion Diode" (IPD)[5,6] with a flat anode is successfully studied in this paper. In this method, the electrostatic field in IPD leads to focusing of ion beams. An advantage of IPD is very simple for focusing of ion beams.

For application of surface modification, medium or heavy ion beams are required, because hydrogen ions are only damage to materials. Generation of the carbon ion beam have been tried with the anode painted in Aquadag by using of IPD.

In this paper, generation and focusing of intense ion beams with IPD having the flat anode is reported.

2. Experimental Setup

Figure 1 shows the schematic drawing of IPD. The diode consists of a ring cathode projected from a circular plate and a ring anode. The circular plate is connected to a ground plate with a metal rod which is located on the axis of the ring anode. When a pulse high voltage is applied to the diode, the electrons emitted from the cathode are accelerated to the anode. Electron bombardment produces an anode plasma from which ions are extracted. At the same time, the current flowing along the metal rod generates a strong azimuthal magnetic field. By this field, magnetic insulation of the electrons is achieved and effective ion beam generation is expected.

The experimental setup of IPD is shown in Fig. 2. This diode was set at the end of the pulse power generator "HARIMA-II"(400kV, 3 Ω, 50ns). The outer diameters of the cathode and the anode were 15, 50 mm, respectively. A 2 mm thick acrylic plate was attached to the anode surface as a plasma source.

A diode voltage (V_d) is measured at the anode plate by using a resistive voltage divider. A diode current (I_d) is measured with a Rogowski coil. Two types of biased ion collectors (BIC) are used to measure ion beam currents. A small BIC with a small aperture of 0.5 mm in diameter is used to estimate the current density of ion beams. A large BIC (210 mm in diameter) with the mesh of the transparency 0.2 % is used to estimate the total current of ion beams. Each collector of the BICs are biased at -450 V to remove accompanying electrons. A Thomson-parabola ion spectrometer is employed for analyzing the species and those energies of ion beams. The collimator has the two pinholes of which diameters are 0.2 and 0.5 mm. The maximum values of the magnetic and the electric field are 0.54 T and 6 kV/cm, respectively. The film CR-39 is used for detection of analyzed ions.

3. Experimental Results

3.1 Focusing of the intense ion beam with IPD

3.1.1 Diode characteristics

Figure 3 shows the typical waveforms of the diode voltage (V_d) and the diode current (I_d). In Fig.3, V_d reaches to the peak value (180kV) in about 10 ns, and the pulse width (FWHM) is 80 ns. The diode current rises

up in about 10 ns after V_d is initiated, and reaches its peak value of 95 kA by 75 ns. Here inductive correction for V_d was not carried out, because the voltage divider was located close to the anode plate.

Figure 4 shows the ion beam current density measured by the small BIC with the bias voltage to the collector (j_i) and with no bias voltage (j_o). In Fig.4, j_i has a peak value of 200 A/cm^2, and there is a little signal with no bias voltage because of neutralization for the ion beams due to accompanying electrons.

3.1.2 Measurement of ion beam with BICs

Figure 5 shows the waveforms of the total ion beam current (I_i) measured with the large BIC located at 120 mm from the anode. As seen in Fig.5, the peak value of I_i is 5 kA. The generation efficiency of the ion beams ($\eta = I_i / I_d$) is roughly calculated by using the peak values of I_i (~5kA) and I_d (~100kA, from Fig.3), resulting in 5%.

The radial profiles of the ion beams at various positions on the diode axis are shown in Fig.6. These profiles were obtained by combining the several data measured with the small BIC. As seen in Fig.6, the ion beams generated with the flat anode have the maximum value of the current density on the diode axis. This means that the ion beam is focused. From Fig.6, the maximum current density (j_i) is 0.5 kA/cm^2 at 120 mm distance from the anode surface on the diode axis. And the focusing radius (r') of the ion beam (FWHM of these profiles) is 10 mm at this point.

3.1.3 Calculation of electrostatic field in IPD

The electrostatic field in IPD was calculated by solving Laplace's equation ($\nabla^2 \phi = 0$) with the finite element method. The calculated equi-potential lines are shown in Fig.7, where the outer radius of the cathode and the anode were 7.5 mm and 25 mm, respectively.

As ions extracted from the anode are accelerated perpendicular to the equi-potential lines in Fig.7, it is expected that the ions are focused at a point on the diode axis. Ion beam trajectories would be considerably affected by electron cloud (virtual cathode) in front of the anode. When ion beams are extracted by the virtual cathode, ion beams might travel parallel to the diode axis and tend to diverge. However, the electron beam current in this experiments is not so large that the electrostatic field is dominant for ion beam focusing than the effects of

electron space-charge, resulting in the ion beam focusing due to the electrostatic field in the diode. Furthermore, in order to get exact trajectories of ions, it is necessary to calculate the electric field including the space-charge effects in the diode.

3.2 Generation of carbon ion beam with IPD

3.2.1 Typical waveforms

Carbon ion beams have been generated by IPD. This experiment was performed with the same set up shown in Fig.2. An acrylic plate painted in Aquadag was attached to the anode surface as a plasma source.

Figure 8 shows the typical waveforms of the diode voltage (V_d) and the diode current (I_d). The top value of V_d was smaller than that obtained in Fig.3, and was 100 kV. This is due to shortening the A-K gap by painted in Aquadag on the anode. And the peak value of I was 120 kA.

3.2.2 The total currents of the ion beams

The total currents of the ion beams were measured by the large BIC located at 120 mm from the anode surface. Figure 9 shows the peak values of the ion beam currents correspond to H^+ and C^+ against the numbers of shots. In the first shot, the values of both hydrogen and carbon ion beam current were small. The currents of carbon and hydrogen ion beam have the maximum values in the second and the third shot, respectively. And these values were 8 and 14 kA. After a few shots, the values of carbon and hydrogen ion current were decreased. This means that Aquadag painted on the anode surface was consumed.

3.2.2 Analysis of ion species with Thomson-parabola ion spectrometer

Figure 10 shows the typical traces on the film CR-39 located in the Thomson-parabola ion spectrometer. This trace was obtained at the second shot. From Fig.9, the main components of the ion beam are found to be hydrogen and carbon, and these ions have the energy ranged from 80 to 120 kV. The C^+ and C^{2+} have two to three times higher energies obtained by the diode voltage in Fig.8. These ions are produced charge exchange from C^{3+}.

4. Summary

Generation and focusing of the ion beam by the "Inverse Pinch Ion Diode" with the flat anode was experimentally studied. The major result

are follows :

1. The energy of the ion beam was about 160 keV, and the total current of the ion beam was 5 kA.

2. In spite of the flat anode, extracted ions were focused at a point on the diode axis and the intensity of the ion beam was 0.5 kA/cm^2.

3. Calculated electric fields in the diode without space-charge effects indicate that trajectories of ions are bent towards the diode axis.

Generation of the carbon ion beam have been tried. The total current of the carbon ion beam was 8 kA on the second shot.

REFERENCES

1) S. Humphries, Jr.: Nucl. Fusion, 20 (1980) 1549.

2) Y. Nakagawa, T. Ariyoshi, M. Itami and Y. Fujii: Jpn. J. Appl.Phys. 27 (1988) L719.

3) K. Yatsui: Laser and Particle Beams 7 (1989) 733.

4) R. T. Hodgson, J. E. E. Baglin, R. Pal, J. M. Neri and D. A. Hammer: Appl. Phys. Lett. 37 (1980) 187.

5) S. Miyamoto, K. Imasaki, A. Yoshinouchi, T. Ozaki, S. Higaki, H. Fujita, M. Saito, R. Ozaki, S. Nakai and C. Yamanaka: Proc. 4th IEEE Int. Conf. Pulsed Power Conf., Albuquerque, 482 (1983).

6) S. Miyamoto, A. Yoshinouchi, T. Ozaki, S. Higaki, H. Fujita, K. Imasaki, S. Nakai and C. Yamanaka: Jpn. J. Appl. Phys. 22 (1983) L703.

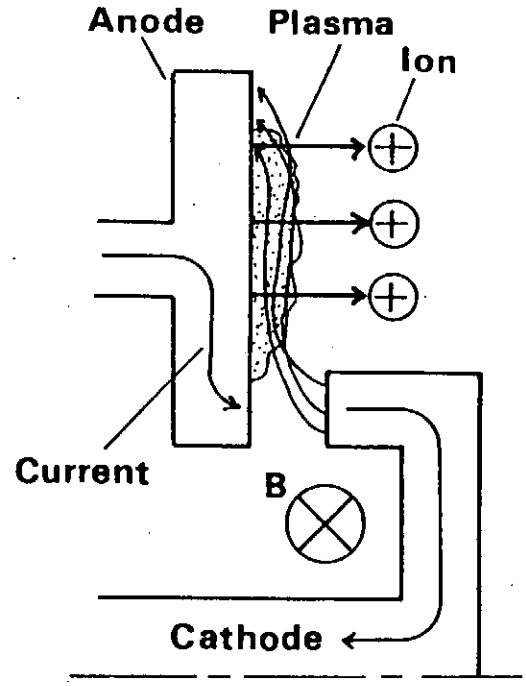

Fig.1 Schematic drawing of the "Inverse Pinch Ion Diode".

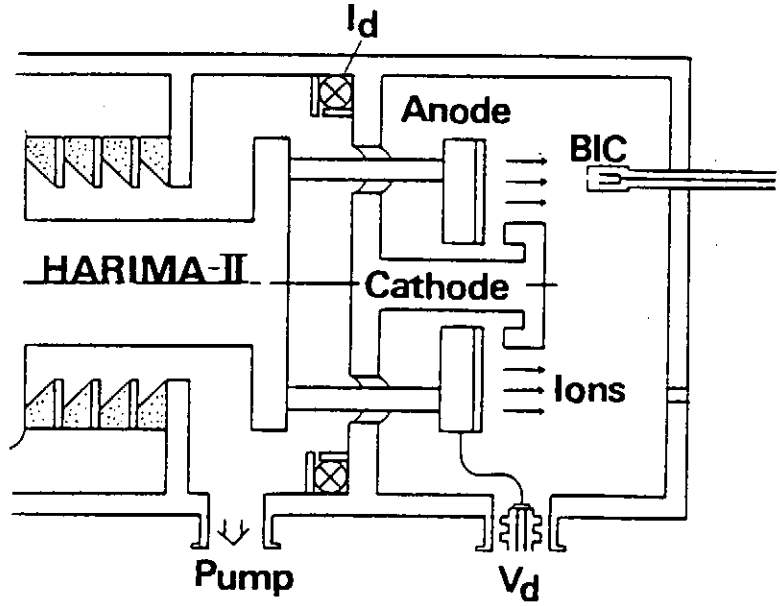

Fig.2 Schematic drawing of the experimental setup.

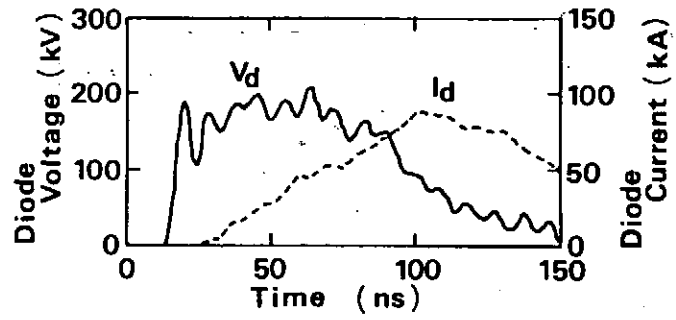

Fig.3 The waveforms of the diode voltage(V_d) and current(I_d).
A acrylic plate ia attached on the anode.
A-K gap length is 3 mm.

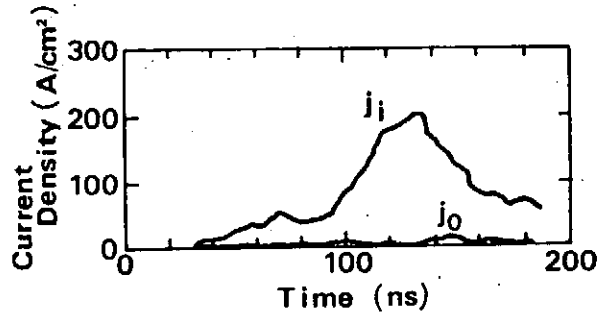

Fig.4 The current density of ionbeams at 100 mm from the anode, where j_i is with bias voltage and j_o is with no bias voltage.

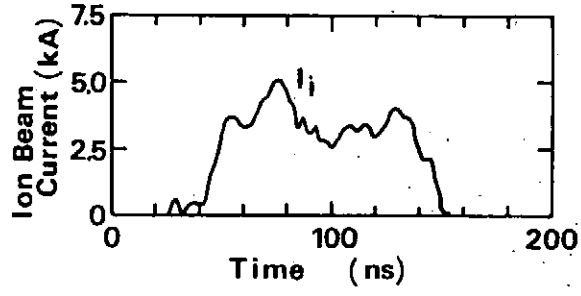

Fig.5 The waveforms of the total ion beam current.

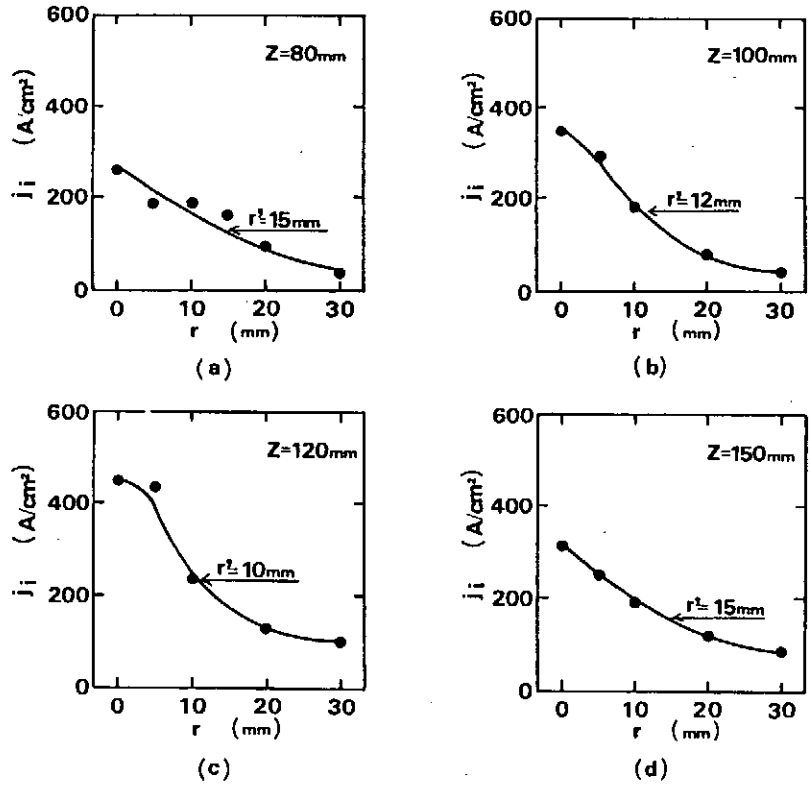

Fig.6 The radial profiles of the ion beam at various positions on the diode axis, where ji is the ion current density, z is the axis distance from the anode and r is the radial distance from the axis.

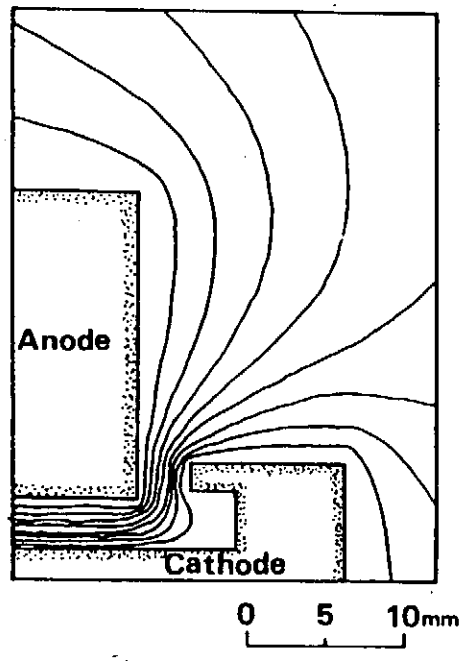

Fig.7 The equi-potential lines in IPD.

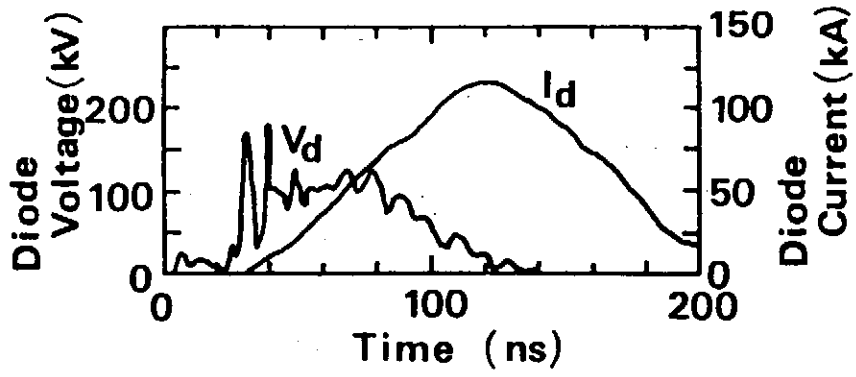

Fig.8 The waveforms of the diode voltage(V_d) and current(I_d). A acrylic plate painted in Aquadag is attached on the anode. A-K gap length is 3 mm.

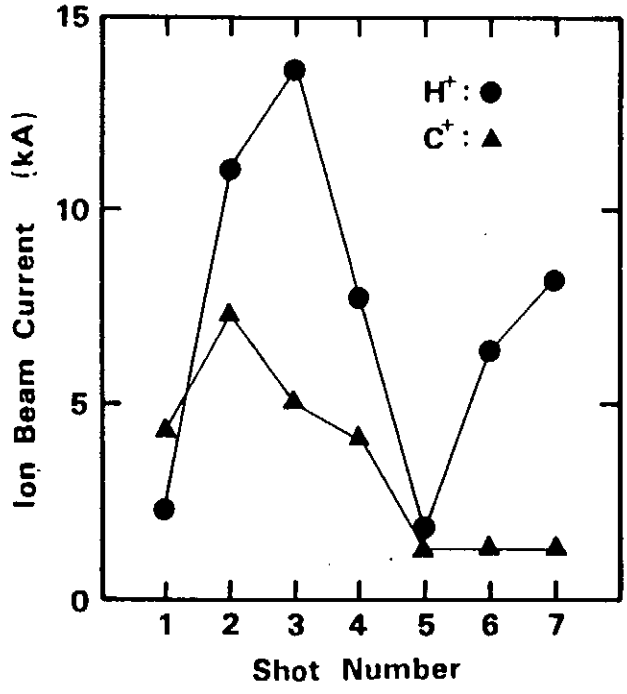

Fig.9 The total currents of the ion beams against the numbers of shots.

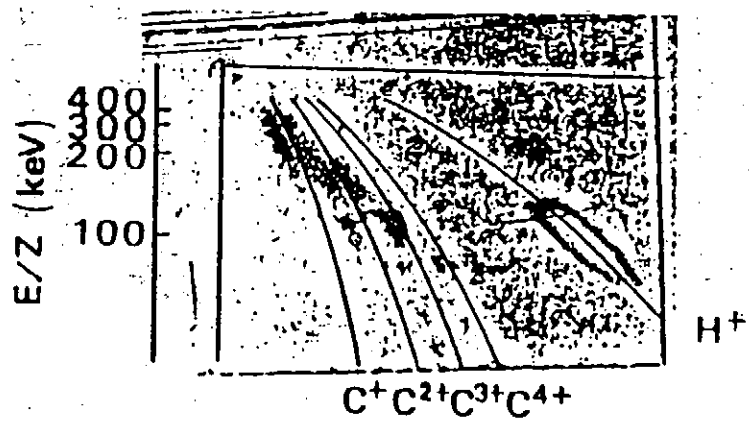

Fig.10 Typical traces on the film CR-39 located in the Thomson-parabola ion spectrometer with the magnetic field of 0.1 T and the electric field of 3 kV/cm.

Generation of Pulsed Ion Beams by an Inductive Storage Pulsed Power Generator

Sunao KATSUKI, Hidenori AKIYAMA, and Sadao MAEDA
Kumamoto University

Abstract

A pulsed power generator by an inductive energy storage system is extremely compact and light in comparison with a conventional pulsed power generator, which consists of a Marx bank and a water pulse forming line. A compact and light pulsed power generator is applied to the generation of pulsed ion beams. A thin copper fuse is used as an opening switch, which is necessary in the inductive storage pulsed power generator. A magnetically insulated diode is used for the generation of ion beams. The pulsed ion beams are successfully generated by the inductive storage pulsed power generator for the first time.

§ 1. Introduction

Developments of pulsed power technologies produced many interesting fields, for example, microwave sources, free electron lasers, soft X-ray sources, neutron sources and mass drivers. The pulsed intense ion beams[1-4] are one of those fields, and have many potential applications as inertial confinement fusion, heating of confined plasma and implantation of ion beams.

The conventional pulsed power generators, which consist of a

Marx bank and a water pulse forming line, have been used as power sources to generate the pulsed intense ion beams. Since the conventional pulsed power generators are too large, a development of compact pulsed power generator has been desired to study many applications of pulsed ion beams. The conventional pulsed power generators have been improved by adding an inductive energy storage pulse compression, using the plasma erosion opening switch(PEOS).[5,6] However, these pulsed power generators are still large machines. An inductive storage pulsed power generator, which does not use a Marx bank and a water pulse forming line, is extremely compact and light, and has been developed.[7-10] Before constructing many compact pulsed power generators to study applications, we have to know if an inductive storage pulsed power generator is able to be used as a power source to produce the pulsed ion beams.

In this paper, we present the first experiment of the pulsed ion beam production by the inductive storage pulsed power generator, which has not a Marx bank and a water pulse forming line. A magnetically insulated diode is selected as a typical ion beam source. A thin copper fuse is used as an opening switch, which is necessary in the pulsed power generator of the inductive energy storage system. The dependence of the ion beam current density on the magnetic field and the radial position is investigated.

§ 2. Experimental Setup

Figure 1 shows the schematic configuration of the experimental

apparatus. After the capacitor(C=10 μ F)is charged 10kV, the trigatron switch is fired. The capacitor is discharged through the solenoid inductor (L=84 μ H) and a copper fuse. When the energy stored in the capacitor is transferred to the inductor, the fuse vaporizes. Then the induced voltage, Ldi/dt, is produced across the fuse. The water is selected as the ambient material of the fuse.[8, 10] The voltage multiplication factor, which is the ratio of the output voltage across the fuse on the charging voltage of the capacitor, is about ten for the fuse of 0.15mm in diameter and 36cm in length. These fuse parameters are selected.

The pulsed power is supplied to the magnetically insulated ion diode through the spark gap, which is operated in air. The spark gap is used to achieve the prepulse suppression and rise time sharpening. The breakdown voltage of the spark gap is adjusted by the gap separation. Therefore, the voltage waveform of the pulsed power supplied to the ion diode is changed by the gap separation. The maximum diode current increases with the decrease of the inductance of the energy storage inductor, since the maximum current, I_D, transferred from the inductor to the diode is expressed by $I_D=V_D\sqrt{C/L}$ at the optimum fuse selection. The voltage, V_D, is the charging voltage of the capacitor.

The plastic anode of 2mm in thickness and 3.5cm in diameter and the stainless mesh cathode of 40 % transparency are used as electrodes of the ion diode. The thirty nine copper pins of 1mm in diameter are buried into the plastic anode. The length of pins near the anode center is a little longer than that at the circumference to get the homogeneous radial distribution of the

ion beam current density. The magnetic field, which is produced by discharging the capacitor of 400 μ F through one turn coil surrounding the anode, is used to avoid for electrons to move across the gap. A part of one turn coil is the mesh cathode. The gap separation of the diode is 2mm. The ions are extracted from the plasma produced on the plastic surface, and accelerated by the pulsed power.

The diode current and voltage are measured by the Rogowski coil and the resistive potential divider respectivelly. The ion beams are measured by the biased ion collector (BIC),[11] which is radially movable at the axial position, 2cm, from the cathode.

§ 3. Results and Discussion

Figure 2 shows the typical waveforms of the diode voltage, V_d, the diode current, I_d, and the ion beam current density, J_i. The ratio of the magnetic field at the diode on the critical magnetic field for the insulation of electrons is 1.8. The waveform of V_d is able to be changed by the gap separation of the spark gap placed between the fuse and the magnetically insulated diode. The voltage waveform with the prepulse is obtained at a small gap separation. The maximum voltage of 60kV, which is about two-fifth of the output voltage obtained for the open-circuit load, is supplied to the diode. The maximum voltage increases with the increase of the gap separation of the diode. The maximum diode current increases with the decrease of the inductance L in Fig.1. The diode and ion beam currents start to

increase at the same time, and then the diode voltage decreases. When the diode voltage becomes almost zero, the diode and ion beam currents become almost maximum and zero respectively. The Child-Langmuir ion current density[12], J_{i0}, which is calculated from the diode voltage, 20kV, at the maximum ion current density, is about $4A/cm^2$. The measured ion current density is larger than J_{i0}, since the electron sheath extends to the anode by the effect of the magnetic insulation.[13]

Figure 3 shows the dependence of the ion beam current density on B/B_0, where B and B_0 are the applied magnetic field to the diode and the critical magnetic field for the insulation of electrons. A typical error bar is shown in Fig.3. The ion beam current density is maximum at B/B_0 1, and becomes near J_{i0} with the increase of B/B_0. This experimental curve qualitatively coincides with the theoretical curve.[13] The maximum ion beam current density is about 5.5 times the Child-Langmuir ion current density.

Figure 4 shows the radial distribution of J_i, where $B/B_0=1.8$. A typical error bar is shown in Fig.4. The length of copper pins, which are buried into the plastic anode, is carefully selected as shown in Fig.4, to get the homogeneous distribution of J_i. If the length of copper pins is equal to the thickness of the plastic anode, the extremely inhomogeneous ion beams with the high density at the circumference are generated. It is important for getting the homogeneous radial distribution of the ion beam current density that the length of pins near the anode center is a little longer than that at the circumference, as is shown in Fig.4.

§ 4. Summary

It is demonstrated that the pulsed ion beams are able to be produced by the inductive storage pulsed power generator, which is extremely compact and light. The inductive storage pulsed power generator has not a Marx bank and a water pulse forming line but a fuse as the opening switch. The magnetically insulated ion diode is selected as the typical ion beam source. The maximum ion current density, $24A/cm^2$, is about 5.5 times the Child-Langmuir ion beam current density. The homogeneous radial distribution of the ion beam current density is obtained by the proper selection of the length of copper pins buried into the plastic anode.

The further intense ion beams will be obtained by the pulsed power generator ASO-1, which is able to generate the higher output power. The detail comparison between the inductive storage pulsed power generator and the conventional pulsed power generator in the ion beam production will be done by ASO-1, which generates the same output power as a conventional pulsed power generator.

References

1) K.Yatsui,K.Masugata and M.Matsui: Phys.Rev.A26(1982)3044.

2) S.Miyamoto,T.Ozaki,K.Imasaki,S.Higaki,S.Nakai and C.Yamanaka:Jpn.J.Appl.Phys.20(1981)L717.

3) S.Miyamoto,S.Sawada,K.Emura,N.Yugami,T.Akiba,T.Ozaki, Y.Mizuguchi,K.Imasaki,S.Nakai and C.Yamanaka:J.Phys.Soc.Japan 57(1988)3277.

4) K.Horioka,T.Takahashi,K.Kasuya,J.Mizui and T.Tazima:Jpn.J. Appl.Phys.23(1984)L374.

5) E.N.Abdullin,G.P.Bazhenov,V.M.Bystritskii,A.A.Kim, B.M.Kovalchuk,V.A.Kokshenev,Ya.E.Krasik,V.M.Matvienko, A.A.SinebryukhovandV.G.Tolmacheva:Sov.J.PlasmaPhys. 13(1987)589.

6) B.V.Weber,R.J.Commisso,G.Cooperstein,J.M.Grossmann, D.D.Hinshelwood,D.Mosher,J.M.Neri,P.F.Ottinger and S.J.Stephanakis:IEEE Trans. Plasma Sci. PS-15(1987)635.

7) D.D.Hinshelwood,J.R.Boller,R.J.Commisso,G.Cooperstein, R.A.Meger,J.M.Neri,P.F.Ottinger and B.V.Weber:Appl.Phys.Lett. 49(1986)1635.

8) H.Akiyama,K.Fujita and S.Maeda:Laser Part.Beams 5(1987)487.

9) H.Akiyama,T.Majima,K.Fujita and S.Maeda:Jpn.J.Appl.Phys.26 (1987)L1743.

10) N.Shimomura,H.Akiyama and S.Maeda:Trans.Insti.Electri.Engi. Japan A109(1989)323.

11) C.Eichenberger,S.Humphries,Jr.,J.Maenchen and R.N.Sudan: J. Appl.Phys.48(1977)1449.

12) I.Langmuir:Phy.Rev.3(1931)238.

13) K.D.Bergeron:Appl.Phys.Lett.28(1976)306.

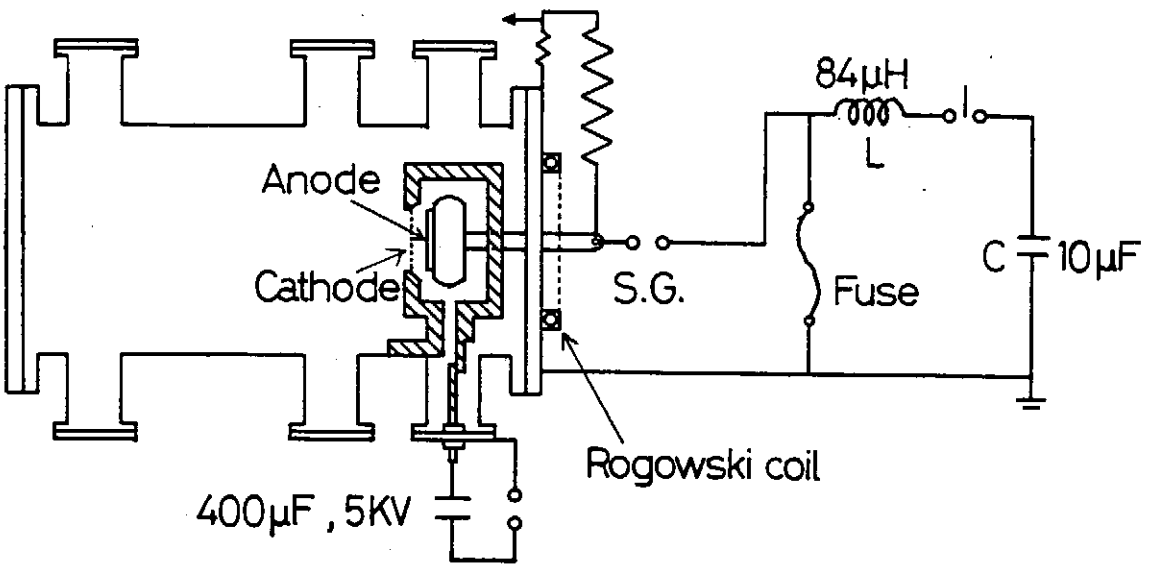

Fig.1. Schematic configuration of the experimental apparatus.

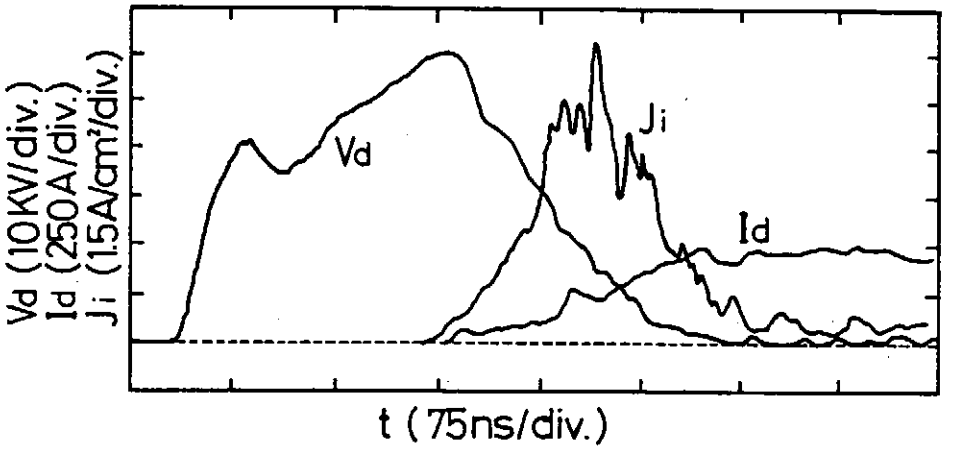

Fig.2. Typical waveforms of the diode voltage, V_d, the diode current, I_d, and the ion beam current density, J_i. The ratio of the magnetic field on the critical magnetic field for insulation is 1.8.

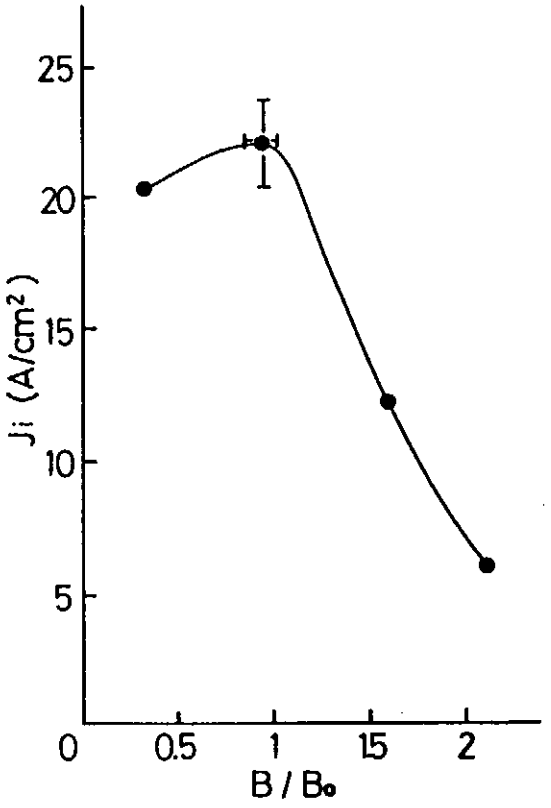

Fig.3. Dependence of the ion beam current density on $B/B_{\square}$.

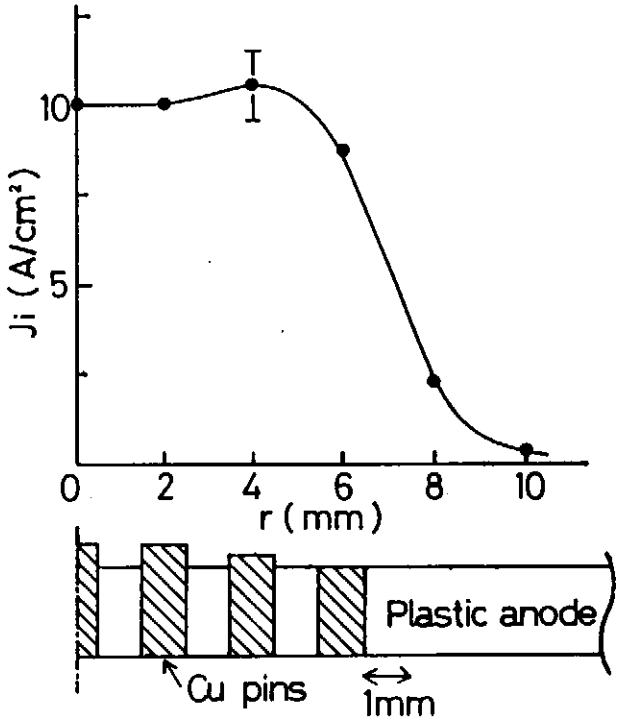

Fig.4. Dependence of the ion beam current density on the radial position, r, at $B/B_{\square}=1.8$.

POWER PLANT BY LIB FUSION

Keishiro Niu, Takayuki Aoki and Hiroya Naramoto
Department of Energy Sciences, the Gratuate School at Nagatsuta
Tokyo Institute of Technology, Midori-ku, Yokohama 227, Japan

Abstract

A fusion power plant of 1GW electric output is proposed here by using proton beam of 12MJ for energy driver. The flibe for the coolant in the reactor cavity with a thickness of 50cm thermalizes the neutrons which produced by fusion reactions and protects the solid wall from being damaged. Tritium-breeding-radio can exceed unity. An indirect-driven-target will implode in a spherically simmetric way even in the nonuniform beam irradiation.

§1. Introduction

Although a proposal of power plant by light ion beam (LIB) fusion has been given,[1] another proposal of power plant of LIB by inertial confinement fusion (ICF) is given here as a reasonable one from technical and economical points of view. The paper includes the analysis for the thermalization of neutrons which are generated by fusion reactions and tritium breeding in the coolant--flibe. The indirect-driven-target is proposed to be used for spherically symmetric implosion of the fuel.[2]

§2. Pulsed Power Supply System

The power supply system is similar to those proposed before.[3] Here proton beam is extarcted from the diode with a particle energy of 8MeV. In order to extract the proton beam from a diode with a particle energy of 8Mev (4Mev for propagation, 3Mev for rotation and 1MeV for thermal oscillation), the output voltage of Marx generator is 16MV. This value seems to be the upper limit for the ordinary Marx generator. For LIB impinging on a spherical target, a spherically symmetric irradiation of LIB on a target may be difficult to be realised. Therefore, the indirect driven target is proposed to be used.[2] In this case, the beam energy, required to release the fusion energy of 3GJ from a target, is 12MJ. Here, 12 power supply systems are prepared. Each two of them are combined together to extract one proton beam of energy of 2MJ. The power supply system is as follows:

Table 1. Power supply system to extract proton beam.

Marx Generator		12 modules	
charging voltage	200kV	capacitance of a banck	2.5μF
number of capacitor banks	80	stored energy	4MJ
		output voltage	16MV
Cylindrical Intermediate Strage Capacitor		12 modules	
insulator	water	inner (anode) radius	3m
outer (cathode) radius	5m	length	3.5m
		charging time	155ns
Pulse Forming Line		12 modules	
input voltage	16MV	output voltage	8MV
length	0.67m	pulth width	τ_b=30ns

Once the power in a Marx genereter is shifted to an intermediate storage capacitor, which is a coxial cylinder filled with water for the directric material. The inner (anode) radius is 3m, the outer (cathode) radius is 5m, and the length is 3.5m. The charging time is estimated to be 155ns. The pulse forming line has the length of 0.67m for the pulse width of 30ns. The input voltage is 16MV and the output voltage is 8MV.

To construct the total power supply systems of 12 modules, the cost is estimated to be US$120M, which is less than 10% of the construction cost of light water reactor of 1GW. Economically and technically, LIB fusion system seems to be reasonable.

As explained in section 4, the electron beam is launched from a triode to the target at the same time with the launching of proton beam in order to neutralise the charge of the proton beam during propagation in the reactor cavity. To let the electron beam have the same velocity with that of proton beam which has the propagation energy of 4Mev, the cathode voltage of triode to accelerate the electron is -6.20kV. This voltage is supplied by a kind of Marx generator, whose stored energy is 3.93×10^2J. The total energy stored in the Marx generators of 6 modules to extract the six-electron beam is only 2.38kJ. To the grid of triode, the voltage of 168kV is supplied through a capacitor bank of 3.54μF, where 50kJ is initially stored. Thus the total stored energy for six capacitor banks of grid circuits is only 300kJ. Required energy to extract six electron beams is negligible in comparison with that for proton beams.

§3. Neutron Thermalisation and Tritium Breeding in Flibe

The reactor to be used is just the same with that proposed by Niu and Kawata.[4] The flibe is proposed to be used as the coolant in the rotating reactor. The flibe is chemically stable and the neutron with the energy of 14.6MeV is thermalised in the flibe layer with the thickness of 50cm. No damage is expected to be accepted on the structural-reactor-wall by the spattering, blistering and swelling. Figure 1 shows the accumlated neutron numbers which are counted at the outer surface of flibe layer with the thickness of 50cm or 75cm in the spherical reactor cavity of radius of 5m. On the inner surface of the flibe layer, 10^{21} neutrons with the particle energy of 14.6MeV impinges in a moment. The group number corresponds to the energy range of neutron: 1, 14-12MeV; 2, 12-10MeV; 3, 10-8MeV; 4, 8-6MeV; 5, 6-5MeV; 6, 5-4MeV; 7, 4-3MeV; 8, 3-1.4 Mev; 9, 1.4MeV-900keV; 10, 900-400keV; 11, 400-100keV;, 12, 100-17keV; 13, 17-3keV; 14, 3keV-550eV; 15, 550-100ev; 16, 100-30eV; 17, 30-10eV; 18, 10-3eV; 19, 3-0.1eV; 20. 0.1-0.04eV: 21, 0.04-0.01eV; 22, 0.01-0.025eV.

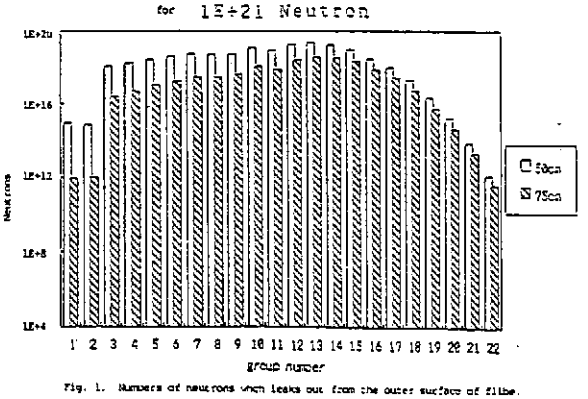

Fig. 1. Numbers of neutrons which leaks out from the outer surface of flibe.

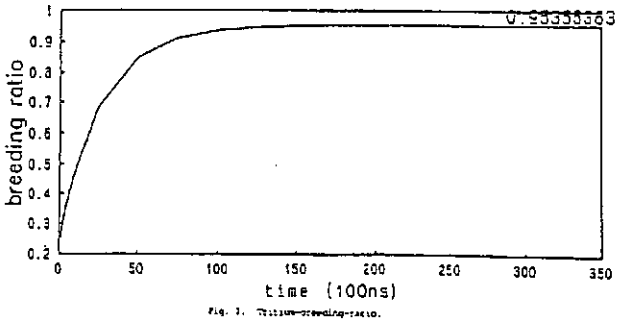

Fig. 2. Tritium-breeding-ratio.

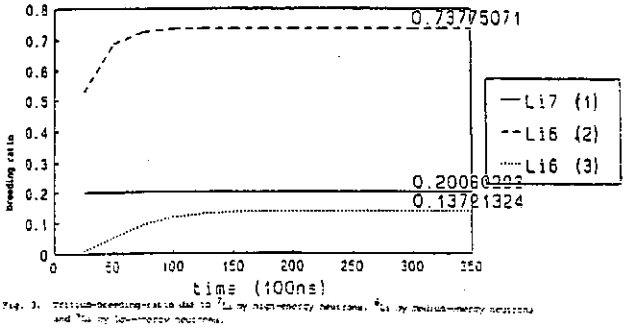

Fig. 3.

From Fig. 1, number of neutrons, which leak out from outer surface of flibe with the particle energies more than 10keV, is counted to be 10^{18}. Among the damages in the solid wall, swelling is the most severe. If one neutron is assumed to knock on lattice atoms on the average in the

solid wall outside the flibe, it takes 420 years (the life time of wall) until the solid wall with the thickness of 1/4 inch accepts the damages of 20% by impinging neutrons.

The volume of flibe per fusion reactor is required to be $300m^3$, when the thickness of flibe layer is 50cm. The corresponding mass of flibe is 600t, in which the lithium mass is 200t. The total lithium mass on the earth is estimated to be $1.8x10^{10}$t. Enough number of fusion power plants with the flibe-wall can be constructed. The difficulty to operate the fusion power plant is diminished and the cost to construct the plant decreases by using the liquid wall of flibe.

Figure 2 shows the accumlated tritium-breeding-ratio versus the time for the flibe with the thickness of 50cm. At t=150ns, the breeding-ratio is saturated. But the ratio is less than unity. Figure 3 indicates the breeding ratios in the flibe with the thickness of 1m for ^{7}Li with high-energy-neutron, ^{6}Li with intermediate-energy-neutron and ^{6}Li with thermalized neutron. The natural lithium in flibe includes 97.5% of ^{7}Li and 2.5% of ^{6}Li. Figure 3 shows that ^{6}Li plays an important role on tritium-breeding. If the mixing ratio of ^{6}Li increases to 5% in the lithium in flibe, the tritium-breeding-ratio will exceed unity in the flibe with the thickness of 50cm.

§4. Diode for Proton Beam and Triode for Electron Beam

The diode for proton beam and triode for electron beam are schematically shown in Fig.4. Two powers from the two pulse-forming-lines are supplied to a diode to extract a proton beam of 2MJ. The parameters of diode is tabulated as follows:

Table 2. Diode for proton beam

anode inner radius r_i=50cm	anode outer radius r_0=23.6cm
anode area S_A=1.67x10^{3}cm^2	electro gap distance d=9.51mm
magnetic field for insulation of	in the azimuthal direction
electron current in the radial	(average) B_θ=3.90T
direction (average) B_r=0.921T	total intensity B_{tot}=4.55T
proton current intensity on the	total proton current $I_b=j_bS_A$=8.33MA
anode surface j_b=5kA/cm^2	$I_{b\parallel}$=4.17MA

By the action of the Lorentz force due to B_r, the proton particle is

accelerated in the azimuthal direction. Thus the proton beam has the particle energy as follows, the total particle energy; e_p=8MeV, the average propagation energy; $e_z=mv_z^2/2$=4MeV, the average rotation energy; $e_\theta=mv_\theta^2/2$=3MeV, the average thermal energy; $e_r=mv_r^2/2$=1MeV.

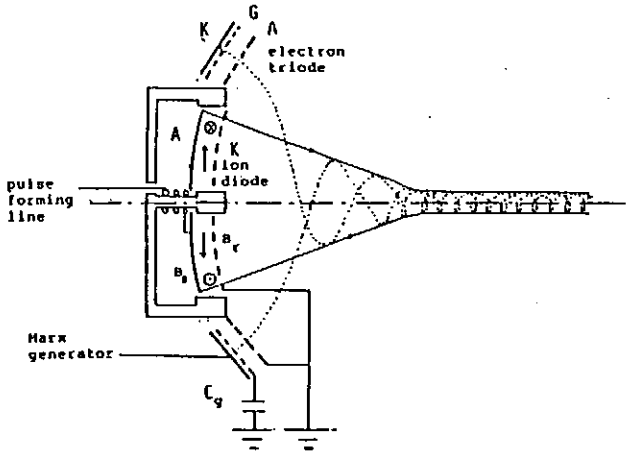

Fig. 4. Diode for proton beam and triode for electron beam.

The proton beam is confined in a small radius of 5mm by the azimuthal magnetic field B_θ which is induced by the beam current $I_{b||}$=4.17MA. This beam propagation is stabilised by the large thermal motion e_r and by the axial magnetic field B_z which is induced by the beam rotation. Since all the proton particles rotate around the axis extracted from a diode shown in Fig. 4, the proton beam forms a hollow cylinder with the inner radius of 2mm and the outer radius of 5mm.

At the leading and trailing edges of a strong proton beam, there remains the particle charges unneutralised and they induce a strong electrostatic field[5] and causes to diverge the beam propagation. To delete these unneutralised ion charge, the proposal is given for launching the electron beam with the proton beam as follows;[6]

Table 3. Triode for electron beam

cathode inner radius r_{in}=25cm	cathode outer radius r_{out}=32cm
cathode area S_K=1.06x10^{3}cm^2	cathode voltage Φ_K=-6.20kV
distance between cathode and anode d_{KA}=1cm	grid capacitor bank C_G=3.54μF
grid current I_G=800kA	grid voltage Φ_G=168kV-150kV
electron current density on the cathod surface j_e=8kA/cm^2	distance between cathode and anode d_{KG}=2.0mm
	total electron current $I_{be}=j_eS_K$=4.17MA

The velocity of electron accelerated by the voltage of Φ_K=-6.20kV is v_e=2.12x10^{7}m/s which is equal to the proton velocity v_z with the propagation energy of e_z=4MeV. Since the partial electron current of

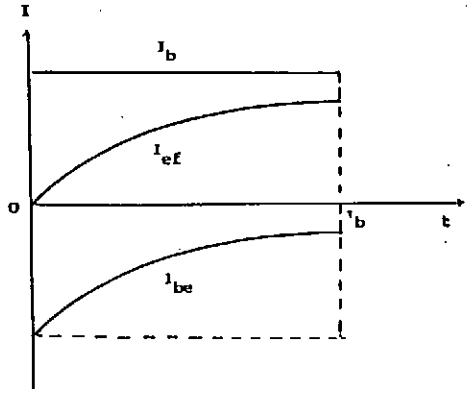

Fig.5. Proton current density I_b, electron current density I_{be}, and effective current density I_{ef} versus time t.

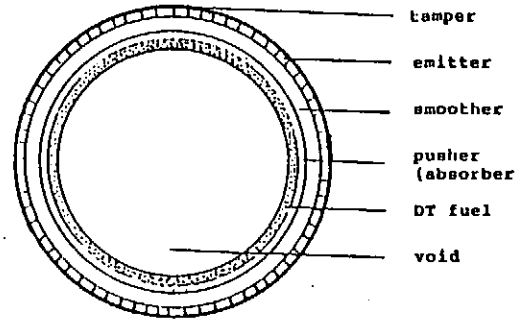

Fig.6. Schematic view of indirect driven target.

800kA flows in the grid circuit, the grid voltage decrease from the initial value of 168kV to the final value of 150kV during 30ns because the grid capacitor bank is 3.54μF in which the initial stored energy is 500kJ. Thus the electron current I_{be} decerases from the initial value of 4.17MA to 3.97MA with time, although the electron velocity remains constant due to the constant cathode-voltage. Figure 2 shows that the proton current $I_{b||}$, the electron current I_{be} and the effective current $I_{ef}=I_{b||}-I_{be}$ versus the time t. Thus the electron beam neutralises the proton charge at the leading edge of the proton beam and the effective current I_{ef}(=200kA at $t=\tau_b$=30ns) is expected to confine the beam in a small radius, if the beam temperature is of order of 100keV.

§5. Indirect-Driven-Target

The indirect-driven-target which is proposed to be used is schematically shown in Fig.6. The target is irradiated by 6 proton beams whose particle energy is 4MeV and total energy is 12MJ with the pulse width of 30ns. The parameters of the target are summarised in Table 4.

Table 4. Indirect-driven-target for beam energy E_b=12MJ and pulse width τ_b=30ns.

	target radius r_t=8.716mm		
	tamper	(lead)	
density	ρ_{Pb}=11.3g/cm^3	thickness	δ_{Pb}=23.4μm
mass	M_{Pb}=120mg	rate of beam energy deposition	
temperature	T_{pb}=8K-500keV		C_{Pb}=20%

leaking out radiation energy loss	E_{rl}=1.5MJ		
	radiator	(lead)	
density	ρ_{ra}=2.13g/cm^3	thickness	δ_{ra}=690μm
mass	M_{ra}=1.49g	rate of beam energy deposition	C_{ra}=80%
temperature	T_{ra}=1.76keV	inward radiation intensity	I_{ra}=4.06x10^{13}W/cm^2
expansion velocity	V_{ra}=1.61x10^{5}m/s		
	radiation gap	(smoother, vacuum)	
thickness	δ_{sm}=2mm		
	pusher	(absorber, aluminium)	
density	ρ_{Al}=2.7g/cm^3	thickness	δ_{Al}=217μm
mass	M_{Al}=264mg	temperature	T_{Al}=8K-200eV
propagation velocity of hot surface	V_h=5.42x10^{3}m/s	transparent time	δ_{Al}/V_h=40ns
	DT fuel		
density	ρ_{DT}=0.19g/cm^3	thickness	δ_{DT}=286μm
mass	M_{DT}=23mg		
	inner void		
radius	r_v=5.5mm	saturated vapour pressure	P_v=7x10^{7}Pa

When the target is irradiated by proton beams of 12MJ, 80% of the beam energy is deposited in the radiator layer, and the temperature of radiator layer increases to T_{ra}=1.76keV, 2.4ns after the start of the beam irradiation. At this temperature, 60% of the deposited beam energy is converted to the radiation energy. About 12% of the radiation energy leaks out from the target through the tamper layer. Thus the average inward radiation (soft x-ray) intensity is I_{ra}=4.06x10^{5}W/cm^2. The radiation gap of thickness of 2mm smoothes out the nonuniformity of the radiation intensity on the outer surface of absorber. The temperature at the outer surface of pusher layer becomes uniform (200eV) after 3ns of x-ray irradiation, even in the case that proton beam irradiates the target from one direction[7]. This radiation gap closes 20ns after the beam-irradiation starts, by the expansion of radiator and absorber layers. The temperature T_{AL}=200eV of the outer surface of aluminium absorber corresponds to the pusher pressure of P_{Al}=7.15x10^{12}Pa. Since the

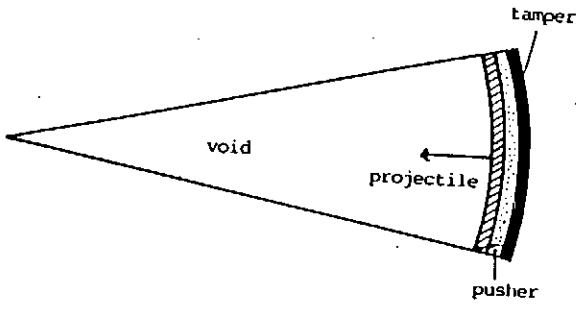

Fig. 7. Projectile, accelerated by pusher, flies with supersonic velocity in a converging nozzle.

temperature of inner absorber layer is so small as 8K that the radiative mean free path is very short. The outer layer of absorber absorbs x-ray and beacomes hot to be transparent for the x-ray. Thus the hot region advances in the absorber layer from the outer layer to the inner layer with the velocity V_h $=5.42\times10^3$m/s. This velocity is slower than the sound velocity ($s_{Al}=5\times10^4$m/s) in the solid aluminium. Thus the pressure p_{Al} at the boundary between the alminium absorber and DT fuel increases gradually to $p_{Al}=7.15\times10^{12}$Pa during 7.5ns and it saturates at that value because of the expansion of absorber layer. In the case that this increase in pressure is not too steep, the fuel acceleration is done in an adiabatic way.[8,9] The acceleration of the fuel reaches $\alpha=p_{Al}S_{DT}/M_{DT}=1.15\times10^{14}$m/s^2, where S_{DT} means the outer surface of DT layer. Thus the fuel-implosion-velocity u arrives at $u=\alpha\tau=3\times10^5$m/s for $\tau=2.6$ns. As Fig. 7 shows, a spherical hollow target forms a supersonic converging nozzle for the DT fuel.[10] To compress the fuel to 2000 times the solid density, the adaiabatic compression is very important. In a supersonic converging nozzle, the fuel is compressed adiabatically, and by the action of small pusher pressure $p_{Al}=7.15\times10^{12}$Pa, the fuel obtains the final high pressure of p_{DT} $=10^{17}$Pa. According to another method for adiabatic compression proposed by Morreeuw and Saillard[8] or by Kidder[11], always pusher pressure should be larger than the fuel pressure, and the DT fuel cannot be compressed 2000 times the solid density. In the supersonic converging nozzle, the fuel density ρ_s at the sonic surface r_s is given by

$$\rho_s/\rho_o=[2/(\gamma+1).\{1+(\gamma-1)M_o^2/2\}]^{1/(\gamma-1)}, \qquad (1)$$

where ρ_o is the initial (solid) density, and M_0 is the initial Mach number. The sonic surface r_s is given by

$$r_s/r_o=M_o^{1/2}[2/(\gamma+1)\{1+(\gamma-1)M_o^2/2\}]^{-(\gamma+1)/4(\gamma-1)}. \qquad (2)$$

The initial position of fuel is $r_0=5\times10^{-3}$m, and the sound velocity of the fuel is $s_0=2.34\times10^5$m/s. Therefore, the initial Mach number of fuel is M_0 $=12.8$. Equations (1) and (2) lead to $\rho_s=2.69\times10^2\rho_0=5.12\times10^4$kg/m^3 and r_s

$=2.63\times10^{-6}$m. In the nozzle inner than r_s, the flow is subsonic and flow-choking occurs. The strong shock wave propagates outward in the fuel. Thus again the fuel is compressed to 2000 times the solid density and especially heated to 4keV. The most important process for ICF is the adiabatic compression of fuel in the supersonic converging nozzle.

References

1) K. Niu, T. Aoki and H. Naramoto: Laser Interaction and Related Plasma Phys. **8** (1988) 605.
2) K. Niu: Laser and Particle beams **7** (1989) 505.
3) K. Niu and T. Aoki: Laser Interaction and Related Plasma Phys. **9** (1989) (in printing).
4) K. Niu and S. Kawata: Fusion Tech, **11** (1987) 365.
5) T. Kaneda and K. Niu: Laser and Particle Beams **7** (1989) 207.
6) K. Niu T. Aoki, P. Mulser and L. Drska: Laser and Particle Beams (submitted).
7) K. Niu, T. Aoki, T. Sasagawa and Y. Tanaka: Laser and Particle Beams (submitted).
8) J. P. Morreeuw and Y. Saillard: Nucl. Fusion **18** (1978) 1263.
9) S. Kawata, K. Abe and K. Niu: J. phys. Soc. Jpn. **50** (1981) 3497.
10) K. Niu and T. Aoki: Fluid Dyn. Res. **4** (1988) 195.
11) R. E. Kidder: Nucl. Fusion **14** (1974) 53.

Control of Gap Closure in Applied-B diode

Takayuki AOKI and Keishiro NIU
Department of Energy Sciences, the Graduate School at Nagatsuta,
Tokyo Institute of Technology, 4259 Nagatsuta, Nidori-ku, Yokohama 227

Abstract

The rapid gap closure due to the build-up of the electron sheath is analyzed by a new one dimensional particle-in-cell code. It is found that the diamagnetic effect of the electrons enhances the ion emission from the anode and increases the amount of the ion charge in the diode gap. The ion charge cancels out the electron charge in the sheath, so that the electron density of the sheath increases and the diamagnetism has more effect on the build-up of the sheath toward the anode. Two methods are proposed to control the gap closure. One is to increase the applied magnetic field and another is to limit the flux emitted at the anode surface. In the simulation results, it is shown that these methods improve the impedance characteristics of the diode.

§1. Introduction

An intense light ion beam (LIB) is one of the promising candidates for the energy driver of inertial confinement fusion. The applied-B ion diodes[1] have many advantages to extract the high current LIB. The enormous experiments have been carried out, and two large problems have been noticed. These are the impedance characteristics and the focusability of the extracted ion beam. A lot of studies are concentrated on these problems[2,3,4], however, these have not been improved so much. In this paper, we pick up the rapid impedance collapse of the diode. The diode impedance is determined by the applied voltage in the gap and the width of the gap, if there is no electron sheath and the ion density of the anode surface is infinity. In reality, the sheath electrons confined by the applied magnetic field decrease the effective gap width. Concerning to the ion source, the emitting surface is not sure to be the anode surface. When the flashover ion source is used, the ion density is enough to extract the ion beam, however, there are neutral particles of several ten times the ion density. The accelerated ions collide with the neutral particles and creat the fast neutral particles by the charge exchange process. These fast neutral particles are ionized in the gap, so that the anode plasma expands rapidly in the gap.[5,6,7] In this paper, because the effect of the fast neutral particles is not clear, it is assumed that the anode ion source is the pure plasma. In the sheath, the electrons do the Larmor motion and $\mathbf{E} \times \mathbf{B}$ drift, and the

diamagnetic effect of the electrons appears. Desjarlais has shown the steady solution that the location of the virtual cathod moves toward the anode[8,9]. In the case of the real cathod construction, it is shown that the electron sheath moves toward the anode and decreases the effective gap of the diode in the following sections.

§2. Particle Simulation Code

In order to study the characteristics of the diode, we have developed a new 1D particle-in-cell (PIC) code MIRKY, coupling with the external circuit for the system of the pulse power supply. Electrons and ions are solved by using PIC model between the anode and the cathode (A-K) gap, in which the electromagnetic fields are applied to accelerate the ions and to insulate the electrons. The motions of the charged particles are employed by the relativisic Newton equation. The numerical differencing forms are described as followed,

$$\frac{\mathbf{p}^{n+1}-\mathbf{p}^{n}}{\Delta t} = q(\mathbf{E}^{n}+\mathbf{v}^{n+1}\times\mathbf{B}^{n}) , \tag{1}$$

$$\frac{m^{n+1}c^2-m^{n}c^2}{\Delta t} = q(\mathbf{E}^{n}\cdot\mathbf{v}^{n+1}) , \tag{2}$$

$$\frac{\mathbf{r}^{n+1}-\mathbf{r}^{n}}{\Delta t} = \mathbf{v}^{n+\frac{1}{2}} , \tag{3}$$

where $\mathbf{v}$ and $\mathbf{r}$ denote the velocity and the position of the particle and the momentum is written in the form $\mathbf{p} = m\mathbf{v}$ and $m = m_0\sqrt{1-\frac{v^2}{c^2}}$. The symbol m_0 is the rest mass, q is the charge of the particle and c is the light velocity. The time interval of the numerical calculation is represented as Δt and the superscript n means the step of the time difference. The symbol $\mathbf{E}$ and $\mathbf{B}$ are the electric and the magnetic fields at the particle position. We use the Cartesian coordinate, whose z-direction is fixed to the A-K direction.

The electric field is applied in the z-direction, and the magnetic field is applied in the x-direction. The electrons have $\mathbf{E}\times\mathbf{B}$ drift in the y-direction and induce the diamagnetic current in this direction. In eq.(1), the y and z components are solved to describe the Larmor motion, however, the charge density and the current density of the electrons and the ions are summed up only in the z-direction of the space. Using the scalar potential ϕ and the vector potential $\mathbf{A}$, we are able to solve the electromagnetic fields, $E_z = -\frac{\partial\phi}{\partial z} - \frac{\partial A_z}{\partial t}$, $E_y = -\frac{\partial A_y}{\partial t}$, $B_x = -\frac{\partial A_y}{\partial z}$, by using the following Maxwell equations,

$$\frac{\partial^2\phi}{\partial z^2} = -\frac{\rho_e}{\varepsilon_0} , \tag{4}$$

$$\frac{1}{c^2}\frac{\partial^2\mathbf{A}}{\partial t^2} + \frac{\partial^2\mathbf{A}}{\partial z^2} = -\mu_0\mathbf{j}_e , \tag{5}$$

where ρ_e is the charge density and j_e is the y component of the current density, respectively. The electrons and the ions are emitted from the anode and the cathod surface and their fluxes are determined by the local Child-Langmuir limiting current density. The surface charge densities are obeied by the Gauss law. To confirm the reliability of the code, two types of well-known solutions have been checked. One of these is the monopolar Child-Langmuir limiting flow[10], and another is the steady solution of the applied-B diode without diamagnetic effect of the electrons.[11] Both of the simulation results have good agreements with the analytic solutions.

The diode is connected with the external circuit as shown in fig. 1. The pulse power system is described in the following equation.

$$L\frac{dI_d}{dt} + (R + Z_d)I_d = V_{ext} \ , \tag{6}$$

where the inductance of the power supply system is denoted as L and the resistance is R. The output voltage of the pulse forming line is V_{ext} and Z_d is the diode impedance and the diode voltage is given as $V_d = Z_d I_d$. Equation (6) is nonlinear with respect to I_d, because the diode impedance depends strongly on the diode voltage and the amount of the charged particles in the diode gap. Therefore, we have to solve this equation iteratively in the implicit differencing form.

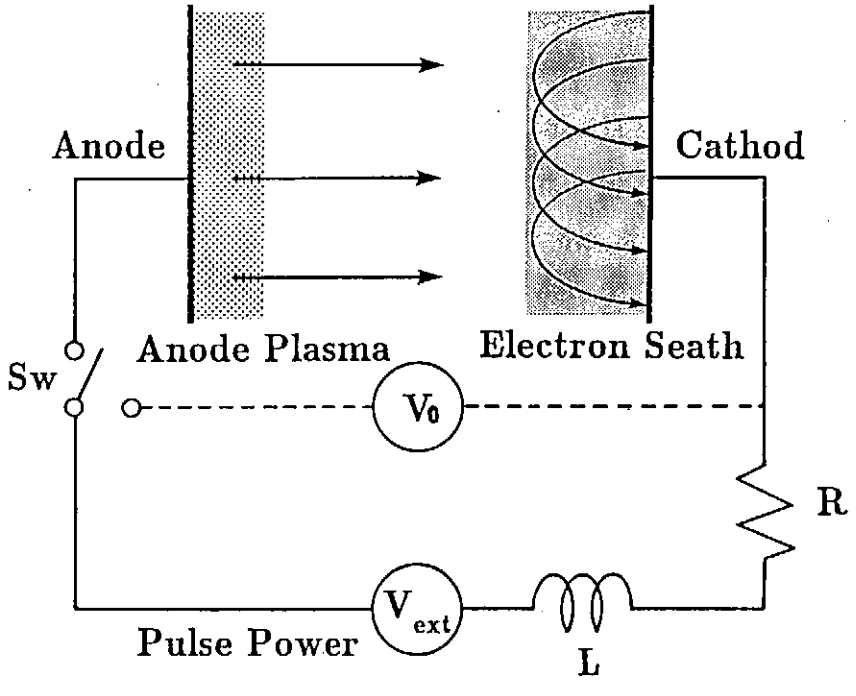

Fig. 1. The equivalent circuit model of the pulse power supply system for the diode simulation.

§3. Diamagnetic Effect

The build-up of the cathod sheath electron reduces the effective gap width in which the external voltage is applied. It causes the rapid impedance collapse of the diode in the operation. Desjarlais pointed out the shift of the virtual cathod location due to the diamagnetic effect.[7,8] In this section, a new explanation of the electron sheath is presented in the case of the real cathod. When only the sheath electron is considered, the diamagnetism has less effect[12] on the width d^* of the electron sheath[13],

$$d^* = \frac{(2eV_0/r_e)^{1/2}(1+eV_0/2m_ec^2)^{1/2}}{<B>}, \tag{7}$$

where $<B>$ is the magnetic field averaged over the sheath width, V_0 is the applied voltage and r_e is the classical electron radius. In the case that there is the ion flow in the sheath, their ion charges cancel the electron ones, and the electron density increases to maintain the constant net charge. The magnetic field becomes small inside the sheath and is enlarged outside, because the diamagnetic effect is proportional to the density. According to eq.(7), the sheath front moves toward the anode. When the gap width d^* decreases, the ion current density J_{CL} is enhanced, obeying the Child-Langmuir Law,

$$J_{CL}{}^* = \frac{4\varepsilon_0}{9}\left(\frac{2Ze}{m}\right)^{1/2}\frac{V_0{}^{3/2}}{d^{*2}} \tag{8}$$

where Z is the charge of the ion. Equation (8) holds good when the anode ion source has enough ion density and there is no limitation for the ion emission. The flashover ion source is approximately satisfied with such conditions. The ion charges in the gap are also increased in association with the enhancement of the ion current. The electron charges in the sheath increase again owing to the enhanced ion charges. Consequently, the diamagnetic effect in the electron sheath becomes stronger. On the other hand, the magnetic field outside the sheath becomes stronger and the insulation effect balances with the diamagnetism. The effective gap is much smaller than the case without account of diamagnetism, and it depends on the initial magnetic field. The ion current does not affect this phenomena for itself, however, the charge is quite important.

In order to confirm the above mechanism, we use MIRKY code with the fixed applied voltage. The enhancement factor, that is, the ion current density normalized by Child-Langmuir current and the location of the electron are shown as a function of time in fig.2. The dark lines mean the results with account of the diamagnetic effect and the shaded lines show the results without account of the diamagnetic effect. The symbol J_i and L mean the ion current density and the real gap width, respectively. In the case that the diamagnetic effect is taken into consideration, it results that the enhancement factor J_i/J_{CL} is about 2.5 times greater than that in the case of no consideration of the diamagnetic effect. The

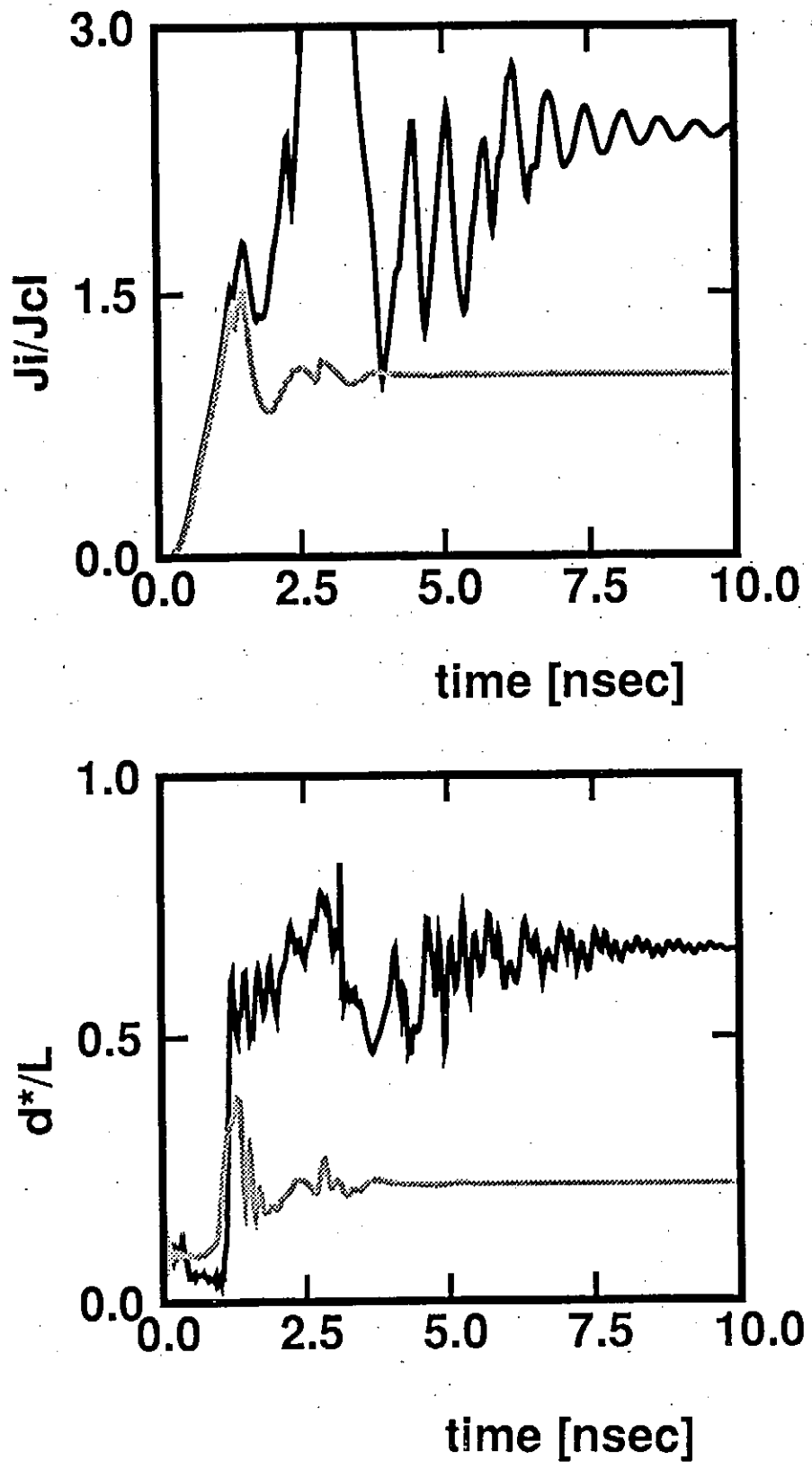

Fig. 2. The enhancement factor and the location of the sheath surface as a function of time. The dark lines mean the results with account of the diamagnetic effect and the shaded lines show the results without account of this.

position of the sheath surface also moves toward the anode by half of the initial gap width. It is sure that the diamagnetic effect induces the rapid collapse of the diode impedance.

§4. Impedance Control of Applied-B diode

It is not so difficult to give the method to control the enhancement of the ion current, because the mechanism becomes clear in the previous section. The chain of the ion current enhancement depends on two reasons. One is the ion emission which is determined by the local Child-Langmuir limitation, that is, the ion current increases to infinity as the gap is closing. Another reason is that the diamagnetic effect depends on the amount of the accumulated electron charges which is supplied from the cathod surface. Therefore, it is possible for us to propose two methods to break the chain of the ion current enhancement, corresponding to the above reasons.

The first method is to increase the applied magnetic field for insulation of the electron current. The electron charge accumulated in the sheath is decreased, so that the diamagnetic effect becomes weak. The electron sheath keeps the constant width, even if there is the ion current. The enhancement of the ion current no more occurs. To prove the efficiency of these methods, we use the simulation code MIRKY connected with the external circuit. The pulse power system is assumed to support the voltage for 10 nsec pulse duration. The voltage keeps a constant of 5 MV for 5 nsec. The pulse has the rising and the tailing of 2.5 nsec. We choose the 10 nsec pulse width to prevent the time consuming of the calculation, because it is enough to simulate the diode characteristics. The inductance and the resistance of the external circuit are 10 nH and 2 Ω, respectively.

When the applied magnetic field $B_{\rm applied}$ is 1.0 Tesla, the enhancement factor and the location of the electron are shown as a function of time with the dark lines in fig.3. The maximum voltage in the diode gap reaches 2.0 MV and the ratio of the applied field to the critical field, $B_{\rm applied}/B_{\rm c}$, is reduced to 1.2. In this case, the diode gap is closed by the build-up of the electron sheath, and the ion current is enhanced extremely at 6 nsec. At this moment, the gap is filled with the electrons and the potential gradient becomes initial state. Then the magnetic field is enough to insulate the electron current, and the width of the sheath is decreased. After 3 nsec, the electron sheath grows and the ion current is greatly enhanced again. In fig.5, it is shown that the diode impedance falls dawn rapidly. For $B_{\rm applied} = 1.5$ Tesla, the applied field is more than 1.8 times the critical field strength. The results are written with the shaded lines in fig.3. The enhancement factor arrives at 3 at most, and the width of the electron sheath keeps half of the real gap. It is understood that the diamagnetic effect is suppressed effectively by the applied magnetic field and depends on its strength sensitively.

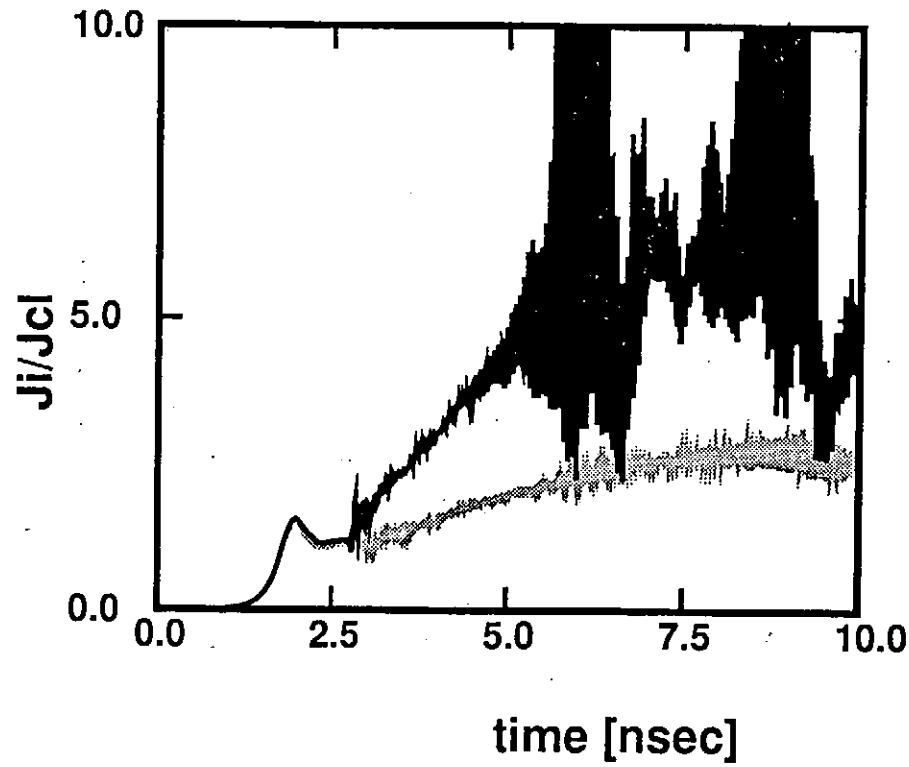

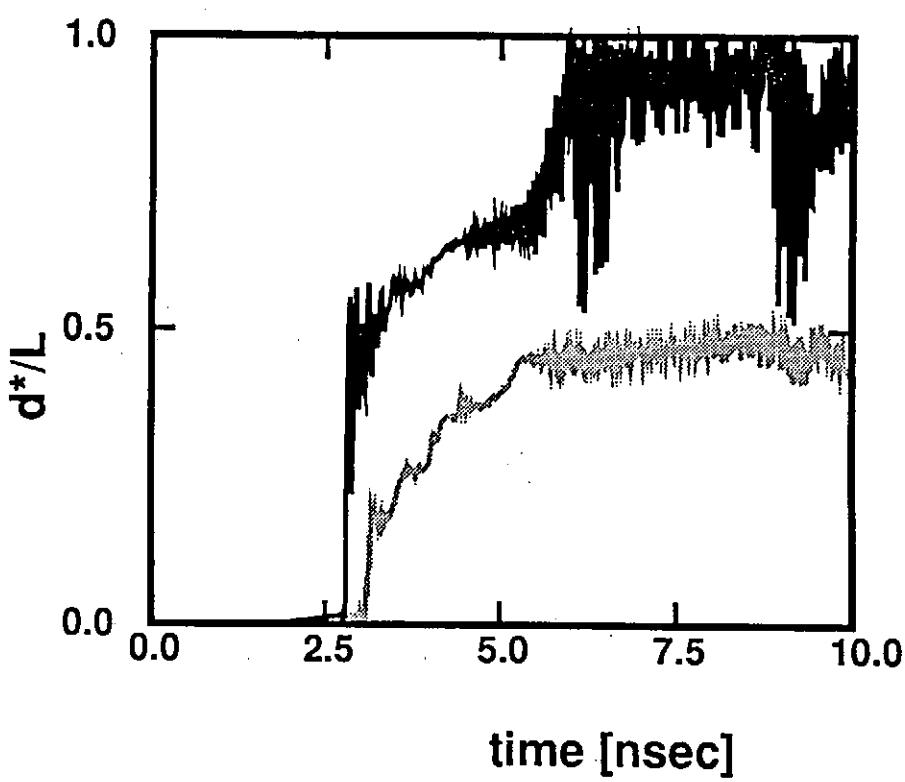

Fig. 3. The enhancement factor and the location of the sheath surface as a function of time. The dark lines mean the results with the applied magnetic field of 1.0 Testa. In the case of 1.5 Tesla, the results are shown with the shaded lines.

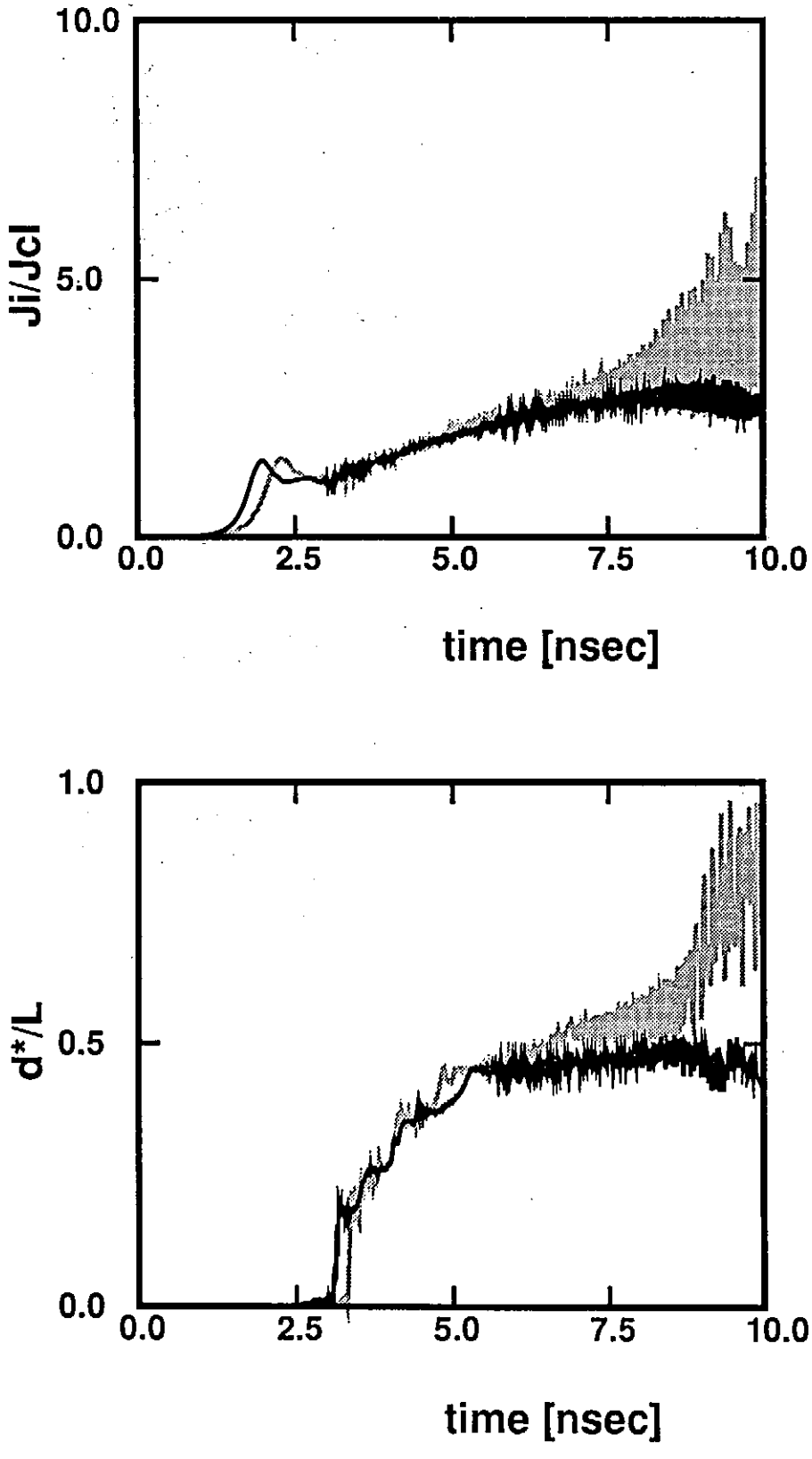

Fig. 4. The enhancement factor and the location of the sheath surface as a function of time. The dark lines mean the results in the case that the limited ion source is used, while the shaded lines are the same ones of fig.3 with the applied magnetic field of 1.5 Tesla.

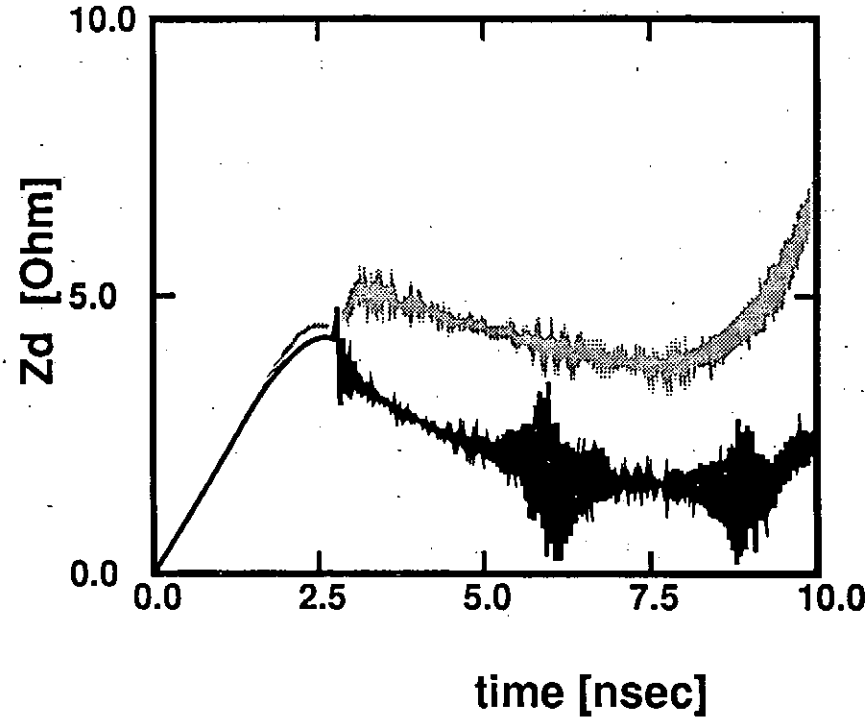

Fig. 5. The impedance characteristics of the diode. The dark lines mean the results with the applied magnetic field of 1.0 Testa. In the case of 1.5 Tesla, the results are shown with the shaded lines.

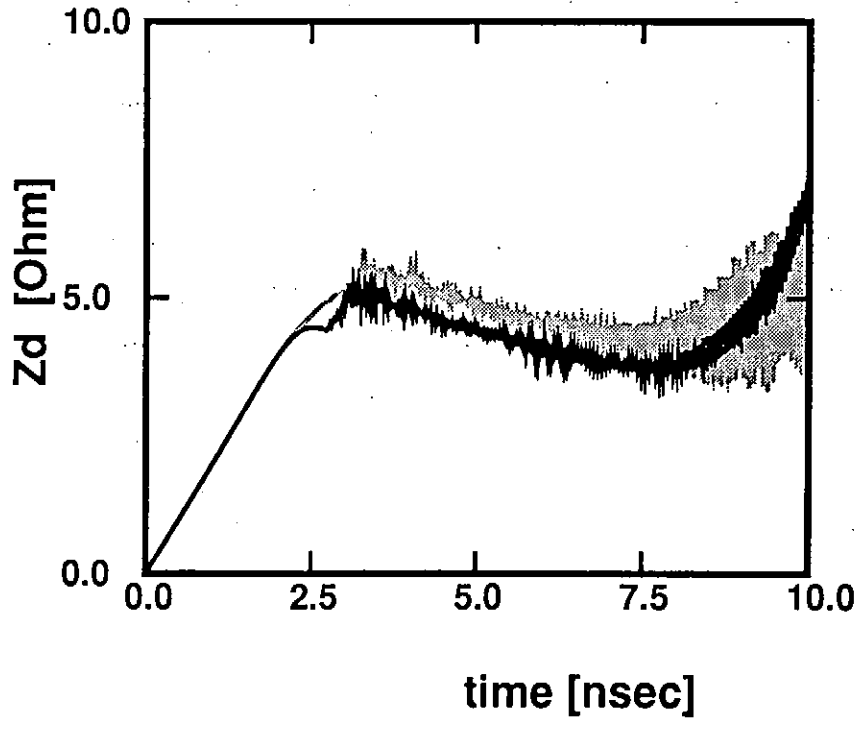

Fig. 6. The impedance characteristics of the diode. The dark lines mean the results in the case that the limited ion source is used, while the shaded lines are the same ones of fig.3 with the applied magnetic field of 1.5 Tesla.

Second method is to limit the ion flux at the anode surface. If a flashover ion source is used, it seems to be impossible to control the ion flux there. When other types of ion source such as the plasma injection is used, the ion flux at the anode is determined by the injected ion, even if the applied electric field increases. Therefore, the ion charge in the sheath does not increases and the electron density keeps constant. The diamagnetic effect does not become strong, and the sheath has the constant width. In the case that the ion flux is limited to the monopolar Child-Langmuir current, the simulation results are shown with the shaded lines in fig.4, while the dark lines represent the same results with that of fig.3 for $B_{\rm applied} = 1.5$ Tesla. It is found that the build-up of the electron sheath is suppressed. The impedance characteristics are shown in fig.6, and both cases have similar nature. The impedance is almost kept constant during the pulse. These simulation results show the validity of the explanation in the section 3.

§5. Summary and Acknowledgements

It was understood that the rapid gap closure due to the build-up of the electron sheath was induced by the diamagnetic effect of the electron. The build-up of the sheath enhanced the ion emission from the anode and increased the amount of the ion charge in the diode gap. The ion charge canceled out the electron charge in the sheath, so that the electron density of the sheath was increased and the diamagnetism had more effect on the build-up of the sheath toward the anode. Two methods was proposed to control the gap closure and examined by using a new particle-in-cell code MIRKY . When the applied magnetic field was more than 1.8 times the critical field, the sheath width kept half of the real gap length. When the emitted flux at the anode surface was limited, the electron sheath did not move toward the anode, even if the applied magnetic field was 1.2 times the critical value. The diode impedance characteristics was improved greatly by these methods.

We would like to thank Dr. Horioka for his useful discussion and advice from the experimental point of view. This work was carried out under the Collaboration Research Program at the Institute of Plasma Physics, Nagoya University (National Institute for Fusion Science), and partly supported by the Scientific Research Fund of the Education, Science and Culture.

References

1) R. N. Sudan and R. V. Lavelace : Phys. Rev. Lett. **31**, 1174 (1973).
2) S. A. Slutz, D. B. Seidel and R. S. Coats : J. Appl. Phys. **59**, 11 (1986).
3) P. A. Miller and C. W. Mendel,Jr : J. Appl. Phys. **61**, 529 (1987).

4) P. A. Miller : J. Appl. Phys. **57**, 1473 (1985).
5) Y. Maron, M. D. Coleman, D. A. Hammer and H. S. Peng : Phys. Rev. Lett. **57**, 699 (1986) ; Y. Maron, M. D. Coleman, D. A. Hammer and H. S. Peng : Phys. Rev. A **36**, 2818 (1987).
6) T. D. Pointon : J. Appl. Phys. **66**, 2879 (1989).
7) M. P. Desjarlais : J. Appl. Phys. **66**, 2888 (1989).
8) M. P. Desjarlais : Phys. Rev. Lett. **59**, 2295 (1987).
9) M. P. Desjarlais : Phys. Fluids B **1**, 1709 (1989).
10) C. D. Child Phys. Rev. **32**, 492 (1911) ; I. Langmuir, *ibid.* **2**, 450 (1913).
11) T. M. Antonsen,Jr and E. Ott : Phys. Fluids **19**, 52 (1976).
12) R. V. Lavelace and E. Ott : Phys. Fluids **6**, 1263 (1974).
13) S. Humphries,Jr : Nucl. Fusion **20**, 1549 (1980).